Technische Universität München

Fakultät für Mathematik
Lehrstuhl M2 - Fachgebiet Numerische Mathematik (Prof. Wohlmuth)

High performance simulation of fluid flow in porous media using lattice Boltzmann method

Ehsan Fattahi Evati

Vollständiger Abdruck der von der Fakultät für Mathematik der Technischen Universität München zur Erlangung des akademischen Grades eines

Doktors der Naturwissenschaften (Dr. rer. nat.)

genehmigten Dissertation.

Vorsitzende:	Univ.-Prof. Dr. Kathrin Glau
Prüfer der Dissertation:	
	1. Univ.-Prof. Dr. Barbara Wohlmuth
	2. Univ.-Prof. Dr. Ulrich Rüde

Die Dissertation wurde am 15.12.2016 bei der Technischen Universität München eingereicht und durch die Fakultät für Mathematik am 27.03.2017 angenommen.

Acknowledgements

I would like to express my sincere thanks to Prof. Dr. Barbara Wohlmuth for giving me a marvelous opportunity to work on this thesis and supported me by her expert guidance. I am indebted to Prof. Dr. Ulrich Rüde, for his advice, guidance, constant encouragement throughout the doctoral research, and hosting me at the chair of system simulation (LSS).

I deeply appreciate Dr. Christian Waluga, Prof. Dr. Michael Manhart and Prof. Dr. Rainer Helmig for their insightful suggestions and several discussions that shaped this work. I am ever grateful to Prof. Mousa Farhadi and Prof. Kourosh Sedighi who introduced me the LBM and gave me the opportunity to work on this topic.

My sincere gratitude goes to Dr. Daniel Weingaertner who helped me in the terrible time at the beginning of this work, for his guidance for adaption to the new environment as well as being supportive and answering my questions regarding the programming. Certainly, I sincerely express my gratitude toward the waLBerla team, Florian Schornbaum, Christian Godenschwager, and Martin Bauer for being always helpful and patient with my programming questions. I am thankful to Simon Bogner, Ali Ghasemi, Christoph Rettinger, for their effective comments and discussions. Thanks to all the colleagues and friends, whom I don't mention here due to space requirements. There are many of them who are actively involved in my life and stay behind it.

Financial support from the German Research Foundation (DFG, Project WO 671/11-1) and also the International Graduate School of Science and Engineering (IGSSE) of the Technische Universität München for research training group 6.03 are gratefully acknowledged.

My special thanks go to my parent, my brothers, and my sister, for supporting me in a terribly long time being far away from home, standing up for me, respecting my decisions. I deeply appreciate you.

Last but the most important, I would like to express my sincere love and gratitude to my wife for her continuing support and encouragement - I don't tell you often enough how important you are. I also thank my little lovely son, Shayan, for the joy and energy he brought to our family to make us stronger and more happy.

Contents

List of Figures

List of Tables

Abstract

The lattice Boltzmann method can be used to simulate flow through porous media with full geometrical resolution. With such a direct numerical simulation, it becomes possible to study fundamental effects that are difficult to assess either by developing macroscopic mathematical models or experiments.

In order to achieve accurate and relevant results, it is important not only to implement very efficient code but also to choose the most appropriate simulation setup. Moreover, it is essential to accurately evaluate the boundary conditions and collision models that are effective from the Stokes regime to the inertial and turbulent flow regimes. In this study, we compare various no-slip boundary schemes and collision operators to assess their efficiency and accuracy. Instead of assuming a constant volume force driving the flow, a periodic pressure drop boundary condition is employed to mimic the pressure-driven flow.

We first consider the convergence rates of various boundary conditions with different collision operators in the Stokes regime. Additionally, we choose different boundary conditions that are representatives of first-order to third-order schemes at curved boundaries in order to evaluate their convergence rates numerically for both inertial and turbulent flow. We find that the multi-reflection boundary condition is second order convergence for inertial flow while it converges with third order in the Stokes regime. Taking into account both computational cost and accuracy requirements, we choose the central linear interpolation bounce-back scheme in combination with the two-relaxation-time collision model. This combination is characterized by providing viscosity independent results and second-order spatial convergence. This method is applied to perform simulations of touching spheres arranged in a simple cubic array. Full- and reduced-stencil lattice models, i.e., the D_3Q_{27} and D_3Q_{19}, respectively, are compared and the drag force and friction factor results are presented for Reynolds numbers in the range of 0.001 to $2,477$. The drag forces computed using these two different lattice models have a relative difference below 3% for the highest Reynolds number considered in this study.

Taking into account computational cost and accuracy, we choose the most efficient combination of the solid boundary condition and collision operator. We apply this method to perform simulations for a wide range of Reynolds numbers from Stokes

flow over seven orders of magnitude to turbulent flow. We investigate the flow behavior for a simple sphere pack and quantify the flow structure at different flow regimes. Moreover, unknown parameters of the Forchheimer, the Barree–Conway and friction factor models are evaluated numerically for the considered flow regimes.

By simulating particle interactions, we construct packed beds of particles with several shapes. We study flow through dense and dilute spherical packings and compare our results to the existing correlations. Furthermore, based on the developed framework, fluid flow through the packing of non-spherical particles are studied. Particle shape and arrangement are shown to influence the pressure drop. Obtained results are compared to the recent correlations of non-spherical particles.

In the last part of this work, we investigate the interaction of free and porous media flow by large scale lattice Boltzmann simulations. We study the transport phenomena at the porous interface on multiple scales, i.e., we consider both computationally generated pore-scale geometries and homogenized models at a macroscopic scale. The pore-scale results are compared to those obtained by using different transmission models. Two-domain approaches with sharp interface conditions, e.g., of Beavers–Joseph–Saffman type, as well as a single-domain approach with a porosity depending viscosity, are taken into account. We show that the two-domain approaches depend sensitively on the choice of the exact position of the interface, whereas our well-designed single-domain approach can lead to a significantly better recovery of the averaged pore-scale results.

Zusammenfassung

Die Lattice Boltzmann Methode kann zur Simulation von porösen Medien mit voller geometrischer Auflösung verwendet werden. Mit solch einer direkten numerischen Simulation ist es möglich, grundlegende Effekte zu simulieren, die nur schwer durch makroskopische, mathematische Modelle oder Experimente zugänglich sind. Um korrekte und relevante Ergebnisse erzielen zu können, ist es zum einen wichtig, hocheffizienten Code zu implementieren, zum anderen aber auch das am besten passende Simulations-Setup zu wählen. Darüberhinaus, ist es essentiell Randbedingungen und Kollisionsmodelle zu wählen, die vom Stokes Bereich bis hin zum turbulenten Bereich geeignet sind. In dieser Arbeit werden verschiedene No-Slip Randbedingungen und Kollisionsoperatoren hinsichtlich Effizienz und Genauigkeit verglichen. Anstatt einer konstanten Volumenkraft zum Anregen der Kanalströmung, kommt eine periodische Druckdifferenz Randbedingung zur Anwendung um den Fluss in dem periodischen Szenario zu simulieren.

Zuerst werden die Konvergenzraten von verschiedenen Randbedingungen mit verschiedenen Kollisionsoperatoren im Stokes Bereich untersucht. Die untersuchten Randbedingung enthielten Randbedingung erster bis dritter Ordnung an gekrümmten Rändern. Somit konnte die Konvergenzrate numerisch sowohl für den Trägheits- als auch für den turbulente Bereich untersucht werden.

Unsere Ergebnisse zeigen, dass die Multi-Reflection Randbedingung mit Ordnung 2 im Trägheitsbereich und mit Ordnung 3 im turbulenten Bereich konvergiert. Unter Berücksichtigung von Rechenaufwand und Genauigkeitsanforderungen, wurde die "central linear interpolation bounce-back"Randbedingung sowie ein Kollisionsmodell mit zwei Relaxationszeiten gewählt. Diese Kombination liefert viskositätsunabhängige Ergebnisse und hat eine räumliche Konvergenz zweiter Ordnung. Diese Methode wurde für die Simulation von sich berührenden Kugeln verwendet, welche in einem einfachen kubischen Gitter angeordnet sind. Volle (D_3Q_{27}) und reduzierte (D_3Q_{19}) Stencils werde verglichen. Es werden Ergebnisse für den Strömungswiderstand und den Reibungsindex gezeigt, für Reynoldszahlen zwischen 0.001 und 2477. Der Strömungswiderstand dieser zwei Modelle zeigt eine relative Abweichung unter 3% für die höchste hier untersuchte Reynoldszahl.

Unter Berücksichtigung des Berechnungsaufwands und der Genauigkeit, wählen wir die effizienteste Kombination von Randbedingung und Kollisionsoperator. Wir wenden die Methode über einen großen Bereich von Reynoldszahlen an, angefangen vom Stokes Bereich bis hin zu turbulenten Bereichen. Wir untersuchen das Flußverhalten in einfachen Kugelpackungen und quantifizieren die Struktur der Strömung in den verschiedenen Regimes. Weiterhin werden jeweils die unbekannten Parameter der Forchheimer-, Barree–Convay- und Reibungsmodelle ausgewertet.

Wir erzeugen Partikelschüttungen mit verschiedenförmigen Teilchen. Wir betrachten die Strömung in Kugelpackungen geringer und hoher Dichte und vergleichen mit existierenden Korrelationen. Weiterhin setzen wir das entwickelte Framework ein, um Strömung durch nicht-kugelförmige Teilchen zu studieren. Man kann zeigen, dass die Teilchenform und die Anordnung der Teilchen den Druckabfall beeinflussen. Die Ergebnisse werden mit neueren Relationen für nicht-sphärische Partikel verglichen.

Im letzten Teil der Arbeit, untersuchen wir die Interaktion von freier Strömung und porösen Medien in Lattice Boltzmann Simulationen auf Großrechnern. Wir studieren die Transportphänomene an der porösen Grenzfläche auf mehreren Skalen, d.h., wir betrachten sowohl Geometrien in der Porenskala als auch homogenisierte Modelle auf der makroskopischen Skala. Die Simulationsergebnisse für die poröse Geometrie werden mit verschiedenen Transitionsmodellen verglichen.

Teilbereichsmodelle mit scharfen Grenzflächen, wie z.B. Beavers-Joseph-Saffman Modelle, genauso wie Einbereichsmodelle mit einer porösitätsabhängigen Viskosität werden ebenso berücksichtigt. Wir zeigen dass die Auftrennung in Teilbereiche stark von der genauen Position der Grenzfläche abhängt, wohingegen unser Ansatz maßgeschneiderter Einbereichsmodelle zu einer signifikanten Verbesserung der gemittelten Porenskalaergebnisse führt.

1 Introduction

Transport phenomena in porous materials are important in many scientific and engineering applications such as catalysis, hydrology, tissue engineering, and enhanced oil recovery. In the past several decades, flow in porous media has been studied extensively both experimentally and theoretically. We refer the interested reader to the textbook (*Helmig*, 2011) and the references therein.

Characterizing flow regimes in porous media is essential for practical applications. The complex geometry of porous media highly influences fluid flow, and the porous structure destroys the boundary layer and forces fluid to pass through narrow and random open passages resulting in a higher pressure drop when compared with that of free flow. In order to quantify the pressure drop, it is necessary to understand the flow regime, transition from one regime to another, and energy dissipation processes.

While the rigorous, analytic up-scaling of the pore-scale problem at lower Reynolds numbers has received much attention in the literature (*Whitaker*, 1986, 1996), similar approaches for higher Reynolds numbers have not been demonstrated yet. This is primarily because of the immense mathematical difficulties that arise in flow models if a moderate Reynolds number cannot be assumed. Analytic solutions are only available for relatively simple applications but usually provide an exact solution.

Experimental data analysis enables in understanding of fluid flow phenomena to develop models and governing equations, that can be analytically or numerically solved. For steady state flow at low Reynolds numbers, a generally accepted and experimentally confirmed macroscopic relation between the pressure gradient and the flow rate is given by Darcy's law (cf. Sec. 2.3.1). Additionally, efforts were made to theoretically derive Darcy's law via different approaches (*Whitaker*, 1986).

Fluid flow in porous media is not restricted to the creeping flow regime in which Darcy's law is applicable. High fluid velocities are required to increase heat and mass transfer rates in many of the fore-mentioned practical applications. Therefore, Reynolds numbers ranging from $\mathcal{O}(10^{-4})$ up to $\mathcal{O}(10^{4})$ are encountered in practice

(*Perry and Green*, 1984). Inertia effects become relevant when the Reynolds number increases (for example, gas flow through a catalytic converter, groundwater flow, filtration processes, and airflow in lungs). At larger pore Reynolds numbers, *Forchheimer* (1901) observed a non-linear deviation from Darcy's relation, and proposed the addition of a quadratic term to the Darcy equation. Although the Forchheimer equation is commonly used in porous media simulations, recent studies suggest that the Forchheimer correction also has a limited range of applicability (*Barree and Conway*, 2004; *Bagci et al.*, 2014).

Pioneering studies involved relating pressure drop to porous media structure, and researchers relied on experiments since it is not possible to derive the exact analytic solution except in simple cases. One of the most widely used relations of the pressure drop and porous media characteristics is the empirical relation proposed by *Ergun* (1952) which defines the pressure drop based on the superficial velocity, the porosity, and the particle diameter.

Real particles, both artificial and natural, have different shapes from a roughly spherical glass to highly irregular shapes of fibrous or biomass materials. In many important applications, such as absorption, processes such as gasification, pyrolysis, and carbonization (*Allen et al.*, 2013), and several syntheses reactors (*Kunii and Levenspiel*, 1991), the particles are not spherical. The pressure drop through the porous media, e.g., packed beds, must be known for the successful and effective design, operation, and optimization of the system. The shape, solid volume fraction, and the orientation of the particles strongly affect the flow behavior (*Nikku et al.*, 2014; *Hölzer and Sommerfeld*, 2008; *Zastawny et al.*, 2012).

When a porous medium and a free flow domain co-exist, e.g., in a river bed, there is no uniquely accepted model for the transition between the Darcy model and the free flow. Different approaches based on single-domain models (*Alazmi and Vafai*, 2001; *Nield and Kuznetsov*, 2009; *Le Bars and Worster*, 2006) or on two-domain (*Beavers and Joseph*, 1967; *Ochoa-Tapia and Whitaker*, 1995; *Nield and Kuznetsov*, 2009; *Duman and Shavit*, 2009) are available. Both, single-domain and two-domain, homogenized models rely on assumptions whose validity is not automatically guaranteed and depend on additional parameters (*Le Bars and Worster*, 2006; *Goyeau et al.*, 2003; *Chandesris and Jamet*, 2009).

Because experimental setups for many practical questions may be too expensive or even impossible to realize, numerical simulation of porous media flow can be a useful complementary method to conventional experiments. Over the past decades, computational fluid dynamics (CFD) is considered as an attractive field due to the

increase in the power of computers. Specifically, CFD provides detailed results by simulating complex multi-physics phenomena that cannot be easily captured by experiments.

However, the application of pore-scale simulations is challenging in most practical situations since the system under study is often several orders of magnitude larger than the characteristic size of the pores. Thus, for practical purposes, many computational techniques are based on macroscopic models that average over many pores and consider average flow rates. Additionally, natural characteristics of a porous medium with irregular geometry make it difficult to solve a system of partial differential equations such as Navier–Stokes equations. Previous studies typically involved several simplifying assumptions to relate the pores in porous media to known shapes or geometry.

In the past two decades, the lattice Boltzmann method (LBM) has attracted the interest of researchers in CFD-related fields. In contrast to traditional CFD approaches based on the conservation of macroscopic quantities such as mass, momentum, and energy, the LBM models a fluid using the kinetics of discrete particles that propagate (streaming step) and collide (relaxation step) on a discrete lattice mesh. Owing to this kinetic nature, microscopic interactions in fluid flow can be handled even in complex geometries such as those in microfluidic devices or porous media (*Singh and Mohanty*, 2000; *Bernsdorf et al.*, 2000; *Kim et al.*, 2001). Moreover, the inherently local dynamics used in LBM afford efficient implementation and parallelization of both of the fundamental algorithmic stages. This allows to harness the computational power of currently available and emerging supercomputing architectures (*Peters et al.*, 2010; *Schönherr et al.*, 2011; *Feichtinger et al.*, 2011; *Fattahi et al.*, 2016a,b).

In this study, we use the waLBerla framework (widely applicable Lattice-Boltzmann from Erlangen) (*Feichtinger et al.*, 2011), which is specifically designed to be used for massively parallel fluid flow simulations; this enables us to compute problems with resolutions of more than one trillion (10^{12}) cells and up to 1.93 trillion cell updates per second using 1.8 million threads (*Godenschwager et al.*, 2013). waLBerla has already been used to study the flow through moderately dense fluid-particle systems *Bogner et al.* (2015) and to simulate large-scale particulate flows *Götz et al.* (2010).

However, having immense computational power at hand is not enough to solve relevant problems. For a three-dimensional LBM simulation, stencils that differ with respect to the velocity directions can be used. Lattice models generally require an exact evaluation of their velocity moments up to second-order to consistently recover Navier-Stokes dynamics in the continuum limit. However, they may behave

differently at a discrete level, which in turn can lead to a violation of some important physical requirements. It was found that lattice models with a plane having less than six velocity vectors are not fully isotropic and can produce qualitatively different results (*Mayer and Házi*, 2006; *White and Chong*, 2011; *Geller et al.*, 2013; *Kang and Hassan*, 2013).

Moreover, the explicitness of classical LBM means that the spatial and temporal discretization characteristics are strongly coupled. Hence, special care must be taken when performing pore-scale simulations to properly incorporate the physics at the boundaries and inside the domain without over-resolving the problem. Several methods have been proposed for the implementation of the LBM on non-uniform grids to improve the geometrical flexibility (*Lee and Lin*, 2003; *Eitel-Amor et al.*, 2013; *Fakhari and Lee*, 2015), as well as the interpolating boundary conditions that can be used by the classical LBM (*Bouzidi et al.*, 2001b; *Mei et al.*, 2000; *Ginzburg and d'Humières*, 2003). As was already pointed out in the evaluation of *Pan et al.* (2006), this requires a suitable combination of collision and boundary operators. The evaluation of different boundaries is mostly done for Stokes flow regimes (*Ginzburg et al.*, 2008b; *Khirevich et al.*, 2015); however, combinations of boundary conditions and collision models must also be evaluated for high Reynolds number flow.

A common way to simulate pressure-driven flow in the LBM is to replace the pressure gradient with an equivalent body force and apply stream-wise periodic boundary conditions. However, previous studies (*Chen and Doolen*, 1998; *Zhang and Kwok*, 2006; *Kim and Pitsch*, 2007; *Gräser and Grimm*, 2010) have shown that using this approach does not lead to correct flow fields for flow through complex geometries, such as e.g., porous media. In this study, we drive flow by imposing a pressure gradient while applying a periodic boundary condition in the stream-wise direction in order to allow the flow to develop based on the geometry.

The objective of this thesis is to evaluate the lattice Boltzmann method for multi-scale simulation of flow through porous media. The focus is on the finding of best strategy for pore-scale simulation by considering various collision operators and boundary conditions that are available in the literature. The best combination of lattice model, collision operator, and boundary condition is chosen regarding the efficiency and accuracy. Different scenarios of porous media flow are selected, such as flow through porous media, packed beds, and free flow over porous media to examine the methods. A homogenized model as a macro-scale model is proposed to represent the correct velocity profile in the case of free flow in presence of porous media.

This thesis is organized as follows: Chapter 2 provides necessary background for fluid flow and porous media (see Sec. 2.3). The existing models of the interface in the coupled system of free flow and porous media are summarized in Sec. 2.4.

The lattice Boltzmann method is explained in chapter 3. First, the basics of the kinetic gas theory are presented in Sec. 3.2. In Sec. 3.4 the lattice Boltzmann method, boundary conditions and collision schemes are described in detail. Brief introduction to the WALBERLA framework is given in Sec. 3.10.

The evaluation of the LBM for porous media that is partly published in (*Fattahi et al.*, 2016b) is presented in chapter 4. We simulate flow through simple sphere packs using different LBM approaches, which is briefly outlined in Sec. 3.4. Their accuracy and convergence rates for flow in the Stokes regime, are investigated in Sec. 4.2. In addition, the computational costs of different boundary schemes are assessed in Sec. 4.4 in order to choose the best combination for highly resolved simulations in high Reynolds numbers flow. After finding a suitable configuration, we then examine the spatial convergence of the boundary schemes in the laminar steady and fluctuating flow regime (see Sec. 4.3).

Using the results of this evaluation, in chapter 5 we simulate the flow through a simple sphere pack for two different solid volume fractions. By sampling over the regime $Re_p \in (10^{-4}, 10^4)$ for a regular packing of touching spheres, we numerically investigate the permeability based on the Reynolds number and evaluate the existing models.

In chapter 6 we extend our LBM simulation for the unstructured packing of different particles. We explain how the packing is constructed in Sec. 6.1. Then we investigate fluid flow through packed beds containing spherical particles (see Sec. 6.2), and the permeability and compare it with available literature data for packed beds. We also simulate flow through packed beds of non-spherical particles in Sec. 6.3.

In chapter 7, we investigate the interaction of free and porous media flow. We study the transport phenomena at the porous interface on multiple scales, i.e., we consider both, computationally generated pore-scale geometries and homogenized models at a macroscopic scale. In Sec. 7.3 we use the results of the direct numerical simulation of flow over and through the porous media as reference solution and evaluate several sharp-interface conditions. As a further example, we also use a homogenized lattice Boltzmann model as a REV scale simulation and show the capability of this model to reproduce the pore-scale results with high accuracy (see Sec. 7.5).

Chapter 8 concludes with a summary and outlook.

2 Theoretical background

2.1 Overview

Fluid flow is a part of daily life, and various phenomena of fluid flow have attracted individuals from an early age. Relatively young individuals can perceive surface wave propagation, force driven flow, bubbly flow, and water channeling. This is followed by understanding and utilizing wind energy and flying objects. This is further realized via scientific analysis.

In real life, the complex phenomena of fluid flow are surprising, because they are difficult to explain without a deep scientific understanding. For example, a Van Gogh painting, titled "La Nuit Etoilee", shows a rare phenomenon of instability in the clouds that in the scientific community is called *Kelvin-Helmholtz instability*. Further examples of fluid flow that may be observed daily include water absorption via a sponge (capillarity), and various sounds of airflow when in contact with solid objects (vortex shedding and the onset of turbulent flow).

Theoretical developments in fluid dynamics help in designing the technical devices at different scales. Examples include microfluidic devices at a micro-scale and buildings at a large-scale. Additionally, practical applications in geology (e.g., groundwater infiltration), medicine (e.g., vocal fold) and meteorology (e.g., weather forecasting) require a deep understanding of fluid behavior and necessitate research that typically involves interaction of fluid flow with other physical or chemical phenomena known as multi-physics problems.

2.2 Governing equations in fluid mechanics

Incompressible fluid flow can be described by a system of partial differential equations (*Kundu et al.*, 2012). A general equation developed by the Swiss mathematician

Leonhard Euler in the 17th century governs incompressible and inviscid fluid flow. Euler's equation is expressed as:

$$\frac{\partial(u_i)}{\partial t} + \frac{\partial[u_i u_j]}{\partial x_j} = -\frac{\partial p}{\rho \partial x_i}, \tag{2.1}$$

where u_i denotes the fluid velocity vector, p is the fluid pressure, and ρ is the fluid density. Claude-Louis Navier then developed an equation based on discrete molecular interactions to include the effects of attraction and repulsion of neighboring molecules. Indeed, the effects of molecular interactions might be viewed as equivalent to viscosity which was not specified by Navier. British physicist and mathematician, Sir George Gabriel Stokes, proposed an assumption for a continuum limit. Specifically, he proposed to use the viscosity term directly and this continues to be the common approach to-date. With respect to incompressible flow, this can be simplified as follows:

$$\frac{\partial(u_i)}{\partial t} + \frac{\partial[u_i u_j]}{\partial x_j} = -\frac{\partial p}{\rho \partial x_i} + \frac{\partial \tau_{ij}}{\partial x_j} + S_i, \tag{2.2}$$

where S_i denotes the source term, and τ_{ij} is the viscous stress which for Newtonian fluid is given as

$$\tau_{ij} = 2\nu S^*_{ij}, \tag{2.3}$$

where ν is the kinematic viscosity (assumed to be constant), and S^*_{ij} is the trace-less viscous strain-rate, and it is defined by:

$$S^*_{ij} \equiv \frac{1}{2}(\partial_{x_j} u_i + \partial_{x_i} u_j) - \frac{1}{3}\partial_{x_k} u_k \delta_{ij}. \tag{2.4}$$

The above equations are always solved in conjuction with the continuity equation:

$$\frac{\partial \rho}{\partial t} + \frac{\partial(\rho u_i)}{\partial x_i} = 0. \tag{2.5}$$

It should be noted that Eq. (2.2) is simply Newton's second law of motion applied to a fluid parcel. The left-hand side corresponds to mass (per unit volume) times acceleration, while the right-hand side corresponds to the sum of forces acting on

the fluid element. Basically, the Navier-Stokes equations represent the conservation of momentum, while the continuity equation represents the conservation of mass.

2.3 Fluid flow in porous media

A porous medium is a solid body that contains random pores or voids. Tiny voids are termed as molecular interstices, and large voids are termed as caverns. Fluid can flow only in the inter-connected pores of a porous medium, and this is known as the effective pore space.

2.3.1 Darcy equations

As a civil engineer, Henry Darcy was interested in the flow characteristics of sand filters. He performed experimental observations of one-dimensional water flow through packed sands for steady state weak inertial flow, which is also known as creeping flow. The findings indicated that the flow rate of water through the filter bed was directly proportional to the area of the sand (*Darcy*, 1857). Additionally, it was proportional to the difference in height between fluid heads at the inlet and outlet of the bed, and inversely proportional to the thickness of the bed. This is now known as Darcy's law. The constant proportionality is defined as the ratio of the permeability and the viscosity of the fluid. Permeability is a geometrical property of porous media, and is entirely independent of the nature of the fluid. It includes geometrical properties of porous media such as porosity, grain shape, and grain size. According to the Darcy's law, the relation between the pressure gradient and flow rate is defined as

$$\nabla P = -\mu K_D^{-1} \mathbf{U}, \tag{2.6}$$

where μ denotes the dynamic viscosity of the fluid, K_D denotes a permeability tensor associated with the geometry of the porous medium under consideration, and $\mathbf{U}$ and P denote the volume averaged velocity and pressure, respectively. This model is valid in the following regime: $Re_p \ll 1$ where $Re_p := \rho d_p U/\mu$ denotes the Reynolds number based on a characteristic pore-diameter d_p, ρ denotes the density of the fluid, and $U := |\boldsymbol{U} \cdot \boldsymbol{i}|$ denotes the scalar velocity in the stream-wise direction $\boldsymbol{i}$. Additionally, *Whitaker* (1986) showed that Darcy's law can be derived from continuous momentum and mass balance assuming that the solid-fluid hydrodynamic interaction is proportional to the relative solid-fluid velocity.

2.3.2 Forchheimer equation

At moderate pore Reynolds numbers, *Forchheimer* (1901) observed a non-linear deviation from the Darcy equation, and proposed the addition of a quadratic term, as detailed below:

$$\nabla P = -\mu K_D^{-1}\mathbf{U} - \beta\rho|\mathbf{U}|\mathbf{U}, \tag{2.7}$$

where β denotes a constant inertial factor proposed by Forchheimer that mainly depends on the flow path and is usually determined experimentally. Replacing the β factor with the dimensionless Forchheimer constant, $\beta = C_F K_D^{-1/2}$, Eq. (2.7) is known as Hazen–Dupuit–Darcy equation (*Lage*, 1998).

2.4 Flow over permeable beds [1]

The phenomenon of flow over porous media can be found vastly in our environment, such as flow over sediment beds, forest, and cities. The flow behavior, physical and chemical properties of the fluid within the permeable bed and above the interface differs significantly from the bulk flow field. Therefore, it is critical to understand the exchange rate of the momentum, mass, and heat between the two regions. Although this has been investigated during the last few decades (*Helmig*, 2011), a clear and satisfying solution has, to the best of our knowledge, not yet been achieved.

2.4.1 Coupling concepts

To describe the flow in the bulk of porous medium, Darcy's law Eq. (2.6) is commonly used. However, when a porous medium and a free flow domain co-exist, e.g., in a river bed, there is no uniquely accepted model for the transition between the Darcy model and the free flow. Different approaches based on a single- or a two-domain model are available. Using a single-domain in combination with the Brinkman equation that modifies Darcy's law by a viscous term

$$-\mu_{eff}\nabla^2\boldsymbol{u} + \mu\boldsymbol{K}^{-1}\boldsymbol{u} = -\nabla p, \tag{Br}$$

[1] Parts of this section are published in "E. Fattahi, C. Waluga, B. Wohlmuth, and U. Rüde (2016), Large scale lattice Boltzmann simulation for the coupling of free and porous media flow, High Performance Computing in Science and Engineering, HPCSE 2015, Czech Republic, May 25-28, 2015, Revised Selected Papers, pages 1–18. Springer International Publishing."

allows to model a smooth transition (see e.g. *Alazmi and Vafai* (2001); *Nield and Kuznetsov* (2009); *Le Bars and Worster* (2006)). Here μ_{eff} is an effective dynamic viscosity in the porous region. However, determining appropriate viscosity parameters for the Brinkman model in the transient region is challenging (*Le Bars and Worster*, 2006; *Goyeau et al.*, 2003; *Chandesris and Jamet*, 2009). Furthermore, the penetration of the flow into the porous medium is found to depend on the roughness coefficient of the surface; see e.g. *Goharzadeh et al.* (2005); *Ghisalberti* (2010); *Morad and Khalili* (2009); *Pokrajac and Manes* (2009).

Alternatively, one can use a two-domain approach in combination with a sharp interface transmission condition. Considering the (Navier-)Stokes equation in the free flow region and the Brinkman (or Darcy) equation in the porous region, the interface plays an important role. Proceeding from the experimental investigation of Poiseuille flow over a porous medium, *Beavers and Joseph* (1967) introduced an empirical approach that agrees well with their experiment; see also *Nield and Kuznetsov* (2009). They suggested to use a slip-flow condition at the interface, i.e., the velocity gradient on the fluid side of the interface is proportional to the slip velocity. For simplicity, we consider a domain in which the interface is aligned with the flow direction. The Beavers¬Joseph relation is formulated as

$$\left.\frac{dU}{dz}\right|_{z=0^+} = \frac{\alpha}{\sqrt{k}}\left(U_s - U_m\right), \tag{BJ}$$

where z denotes the coordinate perpendicular to the interface, $U = U(z)$ is the mean velocity in flow direction, U_s is the slip velocity at the interface $z = 0^+$, U_m is the seepage velocity that is evaluated far from the plane $z = 0$ in the porous region, and k is the permeability. The α is a phenomenological dimensionless parameter that characterizes the structure of the permeable material within the boundary region which typically varies between 0.01 and 5 (*Nield and Bejan*, 2006; *Duman and Shavit*, 2009). We refer the interested reader to *Baber et al.* (2012) and the references therein for the interface coupling of two-phase compositional porous-media flow and one-phase compositional free flow.

In 1971, *Saffman* (1971) found that the tangential interface velocity is proportional to the shear stress. He proposed a modification of the BJ condition as

$$\frac{\sqrt{k}}{\alpha}\left.\frac{dU}{dz}\right|_{z=0^+} = U_s + O(k). \tag{BJS}$$

More than two decades later, *Ochoa-Tapia and Whitaker* (1995) proposed an alternative modification of the BJ condition which includes the velocity gradient on both

sides of the interface as

$$\mu_{eff}\frac{dU}{dz}\bigg|_{z=0^-} - \mu\frac{dU}{dz}\bigg|_{z=0^+} = \frac{\mu}{\sqrt{k}}\beta U_s. \tag{OTW}$$

Here the jump-coefficient β is a free fitting parameter that needs to be determined experimentally (*Martys et al.*, 1994). Different expressions for the effective viscosity μ_{eff} can be found in the literature. For instance, *Lundgren* (1972) suggested a relation of the form $\mu_{eff} = \mu/\epsilon$, where ϵ is the porosity.

All of the interface conditions mentioned above require a priori knowledge of the exact position of the interface (*Zhang and Prospretti*, 2009; *Nabovati et al.*, 2009; *Liu and Prospretti*, 2011), which is for realistic porous geometries often not the case. Additionally, both single-domain and two-domain homogenized models rely on assumptions whose validity is not automatically guaranteed and depend on additional parameters. Traditional experiments to validate and calibrate such models are often costly, time-consuming and difficult to set up. On the other hand, modern high-performance computers enable the development of increasingly sophisticated and accurate computational models resolving pore-scale features.

2.5 Summary

This chapter provided the necessary theoretical background of fluid flow through porous media and summarized the existing models for coupled systems. In the following chapter, the numerical method of the lattice Boltzmann method will be presented.

3 Lattice Boltzmann models

3.1 Overview

The lattice Boltzmann method (LBM) is an approach for computational fluid dynamics (CFD) that solves a discretized Boltzmann equation in the mesoscopic scale. The LBM is based on kinetic gas theory that describes the properties of an idealized gas using point-like particles interacting in collisions. Historically, the LBM emerged from Lattice Gas Automata (LGA), which are known as a leading approach for discrete simulation of fluid dynamics.

Hardy et al. (1976) introduced the first LGA (abbreviated HPP model) to model gas behavior. The basic concept of the LGA is based on the fact that different microscopic interactions lead to the same macroscopic equations. Hence, an artificial micro-world representing the whole system is introduced instead of simulating the interaction of all fluid molecules. Mass and momentum are the two conserved macroscopic quantities in the HPP model. Although this attempt was not sufficient to simulate the Navier-Stokes equations, it attracted considerable attention from researchers in the parallel computing community since the local update rule allows for efficient parallelization.

Frisch et al. (1986) introduced a version of the LGA for Navier-Stokes equations. They introduced an additional condition for the model to recover the Navier-Stokes equations in which it was necessary for the lattice model to possess sufficient symmetry to ensure isotropy of a certain tensor of the fourth rank formed from the lattice velocities. The increasing number of LGA studies revealed the deficiencies of this approach. *McNamara and Zanetti* (1988) proposed replacing Boolean variables with a real number to overcome statistical noise, lack of Galilean invariance, and the velocity dependent equation of state from the LGA. Their approach was considered as the introduction of the LBM, and this numerical method attracted the scientific community.

This chapter focuses on these developments of the LBM and introduces various collision operators, boundary conditions, and lattice models. In the following sections, we first present the basics of kinetic gas theory, and this is followed by the derivation of the lattice-Boltzmann equation.

3.2 Kinetic Gas Theory

Kinetic theory considers a dilute gas that consists of a certain number of molecules in a fixed volume. In a simple model, an ideal gas can be assumed as a group of molecules that behave in a manner similar to rigid spheres. The collision between these particles is assumed to satisfy mass, momentum, and energy conservation. Additionally, it is necessary for the sizes of the particles to be small when compared to the average distance separating the gas particles. This quantity can be classified by the Knudsen number Kn (named after Danish physicist Martin Knudsen (1871–1949)), which defines the ratio of the molecular mean free path and a macroscopic length scale L_0, as

$$Kn \equiv \lambda_f / L_0. \tag{3.1}$$

The continuum assumption of fluid dynamics applies only to the small value of the Knudsen number, that is $Kn \ll 1$. Only statistical methods are valid if the Knudsen number is greater than one.

The equation of state for an ideal gas is defined as

$$PV = NK_BT, \tag{3.2}$$

where P is the absolute pressure, N is the number of molecules in a given volume of the gas V, K_B is the Boltzmann constant, and T is the absolute temperature. Even when the gas is at rest, the molecules of the gas move due to Brownian motion. The mean kinetic energy of the molecules $\bar{E}_K$, in the equilibrium state, is equal to the thermal energy E_T,

$$\bar{E}_K = \frac{1}{2}mc_0^2 = \frac{3}{2}K_BT = E_T, \tag{3.3}$$

where $c_0 = \sqrt{3\frac{K_B T}{m}}$ is the mean absolute velocity of the molecules. This velocity is also commonly defined as $c_0 = \sqrt{3RT}$, where $R = \frac{K_B}{m}$ is the molar gas constant.

The state of the dilute gas describes the combination of its parameters that can be specified by a function of generalized coordinates and moments. The same macroscopic condition can correspond to several different microstates of the gas. If a point specifies these microstates in the phase space, then a continuous distribution can be used to represent the group of the system. The continuous distribution is termed as the density function $f(\boldsymbol{x}, \boldsymbol{\xi}, t)$, and it describes the probability of finding a particle in time t at the particular position $\boldsymbol{x}$ with a certain velocity $\boldsymbol{\xi}$ (*Chapman and Cowling*, 1991). This function is the core construct of kinetic theory.

The macroscopic quantities are defined by integrating the density distribution function over velocity space. The number of particles in a given volume expressed as follows:

$$N = \iint_V f(\boldsymbol{x}, \boldsymbol{\xi}, t)\, d\boldsymbol{x}\, d\boldsymbol{\xi}. \tag{3.4}$$

For infinitesimally small volumes, the variation of $f(\boldsymbol{x}, \boldsymbol{\xi}, t)$ across the volume can be neglected, therefore the density and momentum of particles with mass m are defined as

$$\rho(x, t) = m \int f(\boldsymbol{x}, \boldsymbol{\xi}, t)\, d\boldsymbol{\xi}, \tag{3.5}$$

$$\rho(x, t)\boldsymbol{u}(x, t) = m \int \boldsymbol{\xi} f(\boldsymbol{x}, \boldsymbol{\xi}, t)\, d\boldsymbol{\xi}. \tag{3.6}$$

The molecular collisions between the gas particles and the boundary are assumed as elastic and are assumed to satisfy momentum and energy conservation. Hence, by considering the momentum balance the normal stresses can be obtained as

$$P_{\alpha\alpha} = m \int \xi_\alpha^2 f(\boldsymbol{x}, \boldsymbol{\xi}, t)\, d\boldsymbol{\xi}, \tag{3.7}$$

where $\alpha = x, y, z$. The total isotropic pressure corresponds to the mean of these normal stresses and is expressed as follow:

$$P = \frac{1}{3}(P_{xx} + P_{yy} + P_{zz}) = \frac{m}{3} \int \boldsymbol{\xi}^2 f(\boldsymbol{x}, \boldsymbol{\xi}, t)\, d\boldsymbol{\xi}. \tag{3.8}$$

The right-hand side of the above equation is a ratio of the local energy density of the gas

$$\rho(x, t)\boldsymbol{E}(x, t) = \frac{m^2}{2} \int \boldsymbol{\xi}^2 f(\boldsymbol{x}, \boldsymbol{\xi}, t)\, d\boldsymbol{\xi}, \tag{3.9}$$

when the gas is at rest. Given Eqs. (3.3), (3.8) and (3.9), it can be readily derived that $P = \frac{2}{3}\frac{\rho E}{m} = \rho RT$, which again denoted the equation of state of an ideal gas. Knowing the equation of state, the speed of sound can be defined as

$$c_s^2 = \left.\frac{dp}{d\rho}\right|_{T=const} = RT. \tag{3.10}$$

The full stress tensor can be given by the following expression:

$$P_{\alpha\beta} = m \int \xi_\alpha \xi_\beta f(\boldsymbol{x}, \boldsymbol{\xi}, t)\, d\boldsymbol{\xi} = P\delta_{\alpha\beta} - \sigma_{\alpha\beta}, \tag{3.11}$$

where $\sigma_{\alpha\beta}$ is the deviatoric stress tensor. For Newtonian fluid it can be modeled as

$$\sigma_{\alpha\beta} = \mu\left(\frac{\partial v_\alpha}{\partial x_\beta} + \frac{\partial v_\beta}{\partial x_\alpha} - \frac{2}{3}\frac{\partial v_\gamma}{\partial x_\gamma}\delta_{\alpha\beta}\right) + \eta'\frac{\partial v_\gamma}{\partial x_\gamma}\delta_{\alpha\beta}, \tag{3.12}$$

which μ is the shear viscosity and η' is the bulk viscosity. The bulk viscosity (also called second viscosity) is relevant only when the effect of the fluid compressibility is essential.

The full evolution of the density distribution function was not required since the study focused on macroscopic variables such as density and momentum. Therefore, the few body distribution function was considered as the representative of the systems by using the Boltzmann equation.

3.3 Boltzmann equation

The Boltzmann equation describes the evolution of the particle distribution function (PDF) $f(\boldsymbol{x}, \boldsymbol{\xi}, t)$:

$$\frac{\partial f}{\partial t}(\boldsymbol{x}, \boldsymbol{\xi}, t) + \boldsymbol{\xi} \cdot \nabla_{\boldsymbol{x}} f(\boldsymbol{x}, \boldsymbol{\xi}, t) = \Omega\left(f(\boldsymbol{x}, \boldsymbol{\xi}, t)\right), \tag{3.13}$$

where Ω describes the effect of the collision of two particles. The other part equals the total time derivative $\frac{\mathrm{d}f}{\mathrm{d}t}$ when the chain rule is applied. The collision operator Ω for a two-particle collision is:

$$\Omega\left(f(\boldsymbol{x}, \boldsymbol{\xi}, t)\right) = \frac{1}{m}\int \left(\tilde{\boldsymbol{\xi}}_1 - \tilde{\boldsymbol{\xi}}\right)\left[f(\boldsymbol{x}, \tilde{\boldsymbol{\xi}}_1, t) f(\boldsymbol{x}, \tilde{\boldsymbol{\xi}}, t) - f(\boldsymbol{x}, \boldsymbol{\xi}, t) f(\boldsymbol{x}, \boldsymbol{\xi}_1, t)\right] d\phi d\boldsymbol{\xi}_1. \tag{3.14}$$

The right hand side of Eq. (3.14) transforms the pre-collision velocities of the particles $\boldsymbol{\xi}_1$ and $\boldsymbol{\xi}$ to the post-collision velocities $\tilde{\boldsymbol{\xi}}_1$ and $\tilde{\boldsymbol{\xi}}$, respectively. The transformation

depends on the collision angle ϕ and have to be integrated over all possible collision scenarios.

In the equilibrium state, it is necessary for the PDF f^{eq} to fulfill $\frac{\mathrm{d}f^{eq}}{\mathrm{d}t} = 0$ and hence the following is applicable:

$$\Omega(f^{eq}(\boldsymbol{x}, \boldsymbol{\xi}, t)) = 0, \tag{3.15}$$

i.e., the collision of the particles at the equilibrium state has no effect on their distribution function. Those distributions are called equilibrium distributions and are unique for a given velocity. Equation (3.15) is satisfied if

$$f(\boldsymbol{x}, \tilde{\boldsymbol{\xi}}_{\mathbf{1}}, t) f(\boldsymbol{x}, \tilde{\boldsymbol{\xi}}, t) = f(\boldsymbol{x}, \boldsymbol{\xi}, t) f(\boldsymbol{x}, \boldsymbol{\xi}_{\mathbf{1}}, t), \tag{3.16}$$

or equivalently

$$\ln f + \ln f_1 = \ln \tilde{f} + \ln \tilde{f}_1. \tag{3.17}$$

$\ln f$ is collision invariant, therefore, it can be expressed as a linear combination of the elementary collision invariants

$$\ln f = a + \boldsymbol{b} \cdot \boldsymbol{\xi} + c\boldsymbol{\xi}^2, \tag{3.18}$$

which $a, \boldsymbol{b}$ and c are physically related to the conserved quantities, i.e., the mass, momentum, and kinetic energy (*Gombosi*, 1994). Determining the constant from the moments for density, momentum, and kinetic energy leads to the Maxwell distribution function,

$$f^{eq}(\boldsymbol{x}, \boldsymbol{\xi}, t) = \frac{\rho}{(2\pi RT)^{d/2}} \exp\left[-\frac{(\boldsymbol{\xi} - \boldsymbol{u})^2}{2RT}\right] \tag{3.19}$$

where $\boldsymbol{u}$ is the macroscopic velocity and d is the domain dimension. The Maxwell distribution function provides a correct solution to the Boltzmann equation at thermodynamic equilibrium.

3.4 Conventional lattice Boltzmann schemes [1]

The lattice Boltzmann equation (LBE) is a simplification of the Boltzmann equation in which it is assumed that particle velocities are restricted to a discrete set of values

[1] Parts of this section are published in "E. Fattahi, C. Waluga, B. Wohlmuth, U. Rüde, M. Manhart, and R. Helmig, Lattice Boltzmann methods in porous media simulations: From laminar to turbulent flow, Computers and Fluids, 140 (2016), 247 – 259."

$\boldsymbol{e}_k$, $k = 0, 1, \ldots, q$. The particles can only move along a finite number of directions, that connect the nodes of a regular lattice (*Benzi et al.*, 1992; *Succi*, 2001).

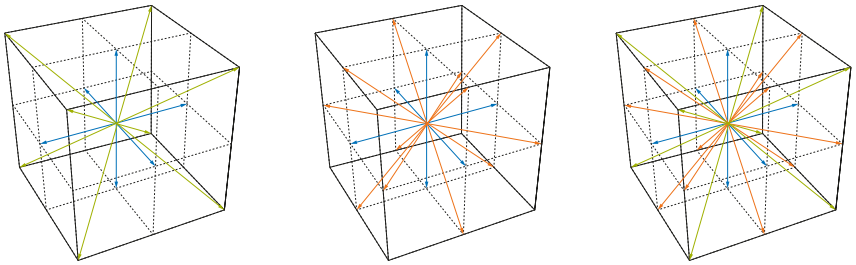

(a) (b) (c)

Figure 3.1: The velocity set in the three dimensional model, a) D_3Q_{15}, b) D_3Q_{19}, c) D_3Q_{27}.

Generally, the stencils for a lattice are denoted as D_dQ_q where d denotes the dimension and q denotes the number of velocity directions. For three dimensions, common stencils are shown in Fig. 3.1. In this study, we evaluate the D_3Q_{19} and D_3Q_{27} lattice models for porous media simulations which will be presented in chapter 4.

Discretizing in time using a time-step size of $\Delta t = t_{n+1} - t_n$, the semi-discrete LBE then reads as

$$f_k(\boldsymbol{x} + \boldsymbol{e}_k \Delta t, t_{n+1}) - f_k(\boldsymbol{x}, t_n) = \Delta t g_k(\boldsymbol{x}, t_n), \qquad k = 0, \ldots, q, \tag{3.20}$$

where $f_k(\boldsymbol{x}, t_n)$ represents the probability of finding a particle at some position $\boldsymbol{x}$ and time t_n with velocity $\boldsymbol{e}_k$. The left hand side of Eq. (3.20) corresponds to a discrete representation of the Boltzmann streaming operator, while the right hand side $\boldsymbol{g} := [g_k]_{k=0}^{q}$ is responsible for controlling the relaxation to a local equilibrium. This is generally split as $\boldsymbol{g} := \boldsymbol{\Omega}(\boldsymbol{x}, t_n)/\Delta t + \boldsymbol{F}(\boldsymbol{x}, t_n)$, where $\boldsymbol{\Omega}(\boldsymbol{x}, t_n)$ is a collision term function of $\boldsymbol{f} := [f_i]_{i=0}^{q}$, representing the change in the distributions due to the interaction between particles, and $\boldsymbol{F}$ is a force term that drives the flow.

3.4.1 Collision operators

The original form of the collision operator in the Boltzmann equation, Eq. (3.14), incorporates complex two-body particle collisions. Bhatnagar, Gross and Krook (BGK, (*Bhatnagar et al.*, 1954)) proposed a more simple expression that satisfies the conservation of the collision invariants and the relaxation towards the Maxwell distribution. The BGK model describes the relaxation of an arbitrary non-equilibrium distribution f with respect to the Maxwell equilibrium.

The collision operator takes the general form

$$\boldsymbol{\Omega}(\boldsymbol{x}, t_n) = -\boldsymbol{R}(\boldsymbol{f}(\boldsymbol{x}, t_n) - \boldsymbol{f}^{eq}(\boldsymbol{x}, t_n)), \tag{3.21}$$

where $\boldsymbol{R}$ is a relaxation operator and $\boldsymbol{f}^{eq}(\boldsymbol{x}, t_n)$ is an equilibrium distribution function of $\boldsymbol{f}(\boldsymbol{x}, t_n)$. The macroscopic values of density ρ and velocity $\boldsymbol{u}$ can be calculated from $\boldsymbol{f}$ as zeroth and first order moments with respect to the particle velocity, i.e.,

$$\rho = \sum_{k=0}^{q} f_k, \qquad \boldsymbol{u} = \frac{1}{\rho_0} \sum_{k=0}^{q} \boldsymbol{e}_k f_k. \tag{3.22}$$

In the LBM, the computation is typically split into a collision and streaming step, which are given as

$$\tilde{f}_k(\boldsymbol{x}, t_n) - f_k(\boldsymbol{x}, t_n) = \Delta t \, g_k(\boldsymbol{x}, t_n), \qquad \text{(collision)}$$
$$f_k(\boldsymbol{x} + \boldsymbol{e}_k \Delta t, t_{n+1}) = \tilde{f}_k(\boldsymbol{x}, t_n), \qquad \text{(streaming)}$$

respectively, for $k = 0, \ldots, q$. The execution order of these two steps is arbitrary and may vary from code to code for implementation reasons.

Single relaxation time (SRT) model

The BGK collision operator, explicitly relaxes the distribution functions to the equilibrium distribution function at a single relaxation rate. The relaxation rate ω is controlled by the mean free flight time, i.e., $\boldsymbol{R}_{SRT} := \omega \boldsymbol{I}$. In this model, the collision frequency is assumed to be constant. It should be noted that SRT does not appear as linear because of the equilibrium distribution function, Eq. (3.19); the Maxwellian is a complicated function of the hydrodynamic variables. However, for small Mach numbers, i.e., incompressible flows $Ma \equiv u/c_s \ll 1$, the equilibrium distribution function can be expanded with respect to the macroscopic velocity u. The extension to the second order in $\boldsymbol{u}$ is

$$f_k^{eq} = \rho w_k \left(1 + \frac{e_k \cdot \boldsymbol{u}}{c_s^2} + \frac{(e_k \cdot \boldsymbol{u})^2}{2c_s^4} - \frac{\boldsymbol{u}^2}{2c_s^2}\right) + \mathcal{O}(\boldsymbol{u}^3), \tag{3.23}$$

where w_k is the weighting function.

The equilibrium distribution function can be further simplified as it is given by (*He*

and Luo, 1997)

$$f_k^{eq}(\boldsymbol{x}, t_n) = w_k \left\{ \rho + \rho_0 \left[c_s^{-2} \boldsymbol{e}_k \cdot \boldsymbol{u} + \tfrac{1}{2} c_s^{-4} (\boldsymbol{e}_k \cdot \boldsymbol{u})^2 - \tfrac{1}{2} c_s^{-2} \boldsymbol{u} \cdot \boldsymbol{u} \right] \right\}, \tag{3.24}$$

where $\rho = \rho_0 + \delta\rho$ while $\delta\rho$ is the density fluctuation, and ρ_0 is the mean density which we set to $\rho_0 = 1$.

Multiple relaxation time (MRT) model

The Multiple Relaxation Time (MRT) can be used instead of relaxing all different modes with a single parameter. In the MRT, the collision is performed in moment space (*d'Humières*, 1992). The MRT is a linear form of the general collision operator (Ω). When compared to the SRT collision operator, the MRT model deals directly with the moments of the distribution functions, such as momentum and viscous stress. By using the MRT model, various collisions that typically occur with different frequencies can be relaxed differently.

Transformation from the velocity space to the moment space is performed one-to-one by a linear transformation $\boldsymbol{M}$, i.e.,

$$\begin{aligned} \hat{f}_i &= M_{ij} f_j \\ f_i &= M_{ij}^{-1} \hat{f}_j \end{aligned} \tag{3.25}$$

where the collision matrix $\boldsymbol{A}$ can be constructed as

$$A_{ij} = \sum_k M_i^{(k)} s_k M_j^{(k)} \tag{3.26}$$

where s_k denotes the relaxation rates (eigenvalues), and $M^{(k)}$ is the kth eigenvector. The eigenvector decomposition is performed by two common approaches, namely Hermit polynomials approach or Gram-Schmidt procedure (*Bouzidi et al.*, 2001a).

The Gram-Schmidt approach is more commonly used (*d'Humières et al.*, 2002; *Lallemand and Luo*, 2000) than the Hermit polynomials approach. In the Gram-Schmidt approach, the rows of the matrix $\boldsymbol{M}$ are obtained by applying an orthogonalization procedure to polynomials of the Cartesian components of the particle velocities. Orthogonal basis vectors, $\boldsymbol{e}_k$, are constructed from the outer product of the particle velocity vectors, $\boldsymbol{c}_i$, e.g.,

$$e_{0i} = 1, e_{1i} = \boldsymbol{c}_{ix}, e_{2i} = \boldsymbol{c}_{iy}. \tag{3.27}$$

The Gram-Schmidt approach ensures that the basis vectors are orthogonal as

$$\sum_i a_{ci} e_{ki} e_{li} = n_k \delta_{kl}, \tag{3.28}$$

where $a_{ci} > 0$ are positive weights. Although a_{ci} is also restricted by the same symmetry condition as the weights for the equilibrium, they are not necessarily the same. The normalization factors, n_i, are related to the choice of the basis vectors

$$n_i = \sum_i a_{ci} e_{ki}^2. \tag{3.29}$$

In the three-dimensional model with 19 velocity directions, i.e., D_3Q_{19}, six quadratic polynomials are created by Eq. (3.28). The polynomials up to the second-order are complete, while there are some dependent vectors in the third-order moments, such as c_{ix}^3 which is equivalent to c_{ix}. With respect to this lattice model, there are six independent third-order polynomials and only three independent polynomials in the fourth-order. Polynomials of order fifth and higher are equivalent to the lower polynomials.

The basis vectors are not unique; they can be created by various models of Gram-Schmidt orthogonalization, with differences stemming from the value of a_{ci}. Standard orthogonalization takes factor as $a_{ci} = 1$, which results in a set of polynomials that is categorized as unweighted in Tab. 3.1. It is worth to note that, the kinetic modes based on this set of basis vectors, i.e., $e_{10} - e_{18}$, are not orthogonal to the equilibrium distribution function. Hence, the moments created by these modes involved both equilibrium as well as non-equilibrium contribution.

Another common choice of the weighting factor included setting $a_{ci} = w_i$ and given this choice, the equilibrium distribution function is not projected to the kinetic moments. This set of polynomials is presented in Tab. 3.1 as weighted polynomials.

The moments can be constructed using the basis vectors, Eq. (3.25), in which the

Table 3.1: Orthogonal vectors of the MRT and TRT collision operator in D_3Q_{19} lattice model (*Chun and Ladd* (2007); *d'Humières et al.* (2002); *Khirevich et al.* (2015); *Ginzburg and d'Humières* (2003)).

k	$Moments$	$e_{ki_{(Weighted)}}$	$e_{ki_{(Unweighted)}}$	MRT	TRT
0	Mass	1	1	-	-
1	Momentum	c_x	c_x	-	-
2		c_y	c_y	-	-
3		c_z	c_z	-	-
4	Kinetic energy	c^2-1	$19c^2-30$	s_e	ω^+
5	Viscous stress	$3c_x^2-c^2$	$3c_x^2-c^2$	s_ν	ω^+
6		$c_y^2-c_z^2$	$c_y^2-c_z^2$	s_ν	ω^+
7		c_yc_z	c_yc_z	s_ν	ω^+
8		c_zc_x	c_zc_x	s_ν	ω^+
9		c_xc_y	c_xc_y	s_ν	ω^+
10	Energy-flux vectors	$(3c^2-5)c_x$	$(5c^2-9)c_x$	s_q	ω^-
11		$(3c^2-5)c_y$	$(5c^2-9)c_y$	s_q	ω^-
12		$(3c^2-5)c_z$	$(5c^2-9)c_z$	s_q	ω^-
13	Cubic polynomial vectors	$(c_y^2-c_z^2)c_x$	$(c_y^2-c_z^2)c_x$	s_h	ω^-
14		$(c_z^2-c_x^2)c_y$	$(c_z^2-c_x^2)c_y$	s_h	ω^-
15		$(c_x^2-c_y^2)c_z$	$(c_x^2-c_y^2)c_z$	s_h	ω^-
16	Kinetic energy square	$3c^4-6c^2+1$	$(21c^4-53c^2+24)/2$	s_ϵ	ω^+
17	Quartic polynomial vectors	$(2c^2-3)(3c_x^2-c^2)$	$(3c^2-5)(3c_x^2-c^2)$	s_π	ω^+
18		$(2c^2-3)(c_y^2-c_z^2)$	$(3c^2-5)(c_y^2-c_z^2)$	s_π	ω^+

hydrodynamic variables are related to the moments up to the quadratic order in c_i:

$$\begin{aligned}
\rho &= \hat{f}_0,\\
j_x &= \hat{f}_1 c,\\
j_y &= \hat{f}_2 c,\\
j_z &= \hat{f}_3 c,\\
\pi_{xx} &= (\hat{f}_0+\hat{f}_4+\hat{f}_5)c^2/3,\\
\pi_{yy} &= (2\hat{f}_0+2\hat{f}_4-\hat{f}_5+\hat{f}_6)c^2/3,\\
\pi_{zz} &= (2\hat{f}_0+2\hat{f}_4-\hat{f}_5+\hat{f}_6)c^2/3,\\
\pi_{xy} &= \hat{f}_7 c^2,\\
\pi_{yz} &= \hat{f}_8 c^2,\\
\pi_{zx} &= \hat{f}_9 c^2.
\end{aligned} \tag{3.30}$$

Two relaxation time (TRT) model

Based on a symmetry argument, *Ginzburg* (2008) proposed a model based on Two Relaxation Times (TRT), which is viewed as the minimal configuration that provides just sufficient free relaxation parameters to avoid non-linear dependencies of the truncation errors on viscosity in the context of porous media simulations (*Ginzburg*, 2007; *Ginzburg et al.*, 2008b,a). The scheme is derived from the MRT approach by splitting the probability density functions f_k into symmetric and anti-symmetric components $f_k^+ := \frac{1}{2}(f_k + f_{\bar{k}})$ and $f_k^- := \frac{1}{2}(f_k - f_{\bar{k}})$, where $\bar{k}$ is the diametrically opposite direction to k (*Ginzburg*, 2007; *Ginzburg et al.*, 2008b,a). Performing a separate relaxation by the two corresponding relaxation rates ω^+ and ω^- yields the operator

$$\boldsymbol{R}_{TRT} := \omega^+ \boldsymbol{R}^+ + \omega^- \boldsymbol{R}^-, \tag{TRT}$$

where $\boldsymbol{R}^+$ and $\boldsymbol{R}^-$ are the tensorial representations of the operators extracting the symmetric and antisymmetric components, respectively.

Cumulant collision model

Cumulants are certain nonlinear combinations of moments that successively encode the deviation of the distribution from a Gaussian equilibrium distribution. Cumulants have a property such that the cumulant of $\mathcal{O}(n)$ provides additional information that does not exist for cumulants of orders lower than n. Therefore, they provide independent observable quantities that can be controlled independently. The cumulants can be calculated by the moments, i.e., the cumulant is the natural logarithm of the moment generating function. By utilizing central moments, the Galilean invariance can be ensured by removing the effect of the frame of reference on the distribution functions (*Geier et al.*, 2015). The two-dimensional cumulant collision is described for purposes of simplicity. An extant study in the form of co-supervised master thesis can be referred to for detailed derivations (*Rohm*, 2016).

To find the moment generating function of the PDFs, first, the PDF f_{ij} is reformulated in a continuous way as

$$f(\boldsymbol{\xi}) := \sum_{i,j} f_{ij} \delta(c_{ix} - \xi_1) \delta(c_{iy} - \xi_2), \tag{3.31}$$

using the Dirac delta distribution δ, characterized by

$$\int f(x)\delta(x)dx = f(0). \tag{3.32}$$

The moment generating function is an integral transformation $\mathcal{L}$ similar to the two sided Laplace transformation, defined as

$$\mathcal{L}[g](\boldsymbol{\Xi}) \coloneqq \int_{\mathbb{R}^n} g(\boldsymbol{\xi}) e^{\boldsymbol{\Xi}\cdot\boldsymbol{\xi}} d\boldsymbol{\xi}.$$

With the help of this transformation, the moment generating function F of the PDF is introduced as

$$\begin{aligned} F(\Xi_1, \Xi_2) \coloneqq \mathcal{L}[f](\boldsymbol{\Xi}) &= \int_{\mathbb{R}^2} f(\boldsymbol{\xi}) e^{\boldsymbol{\Xi}\cdot\boldsymbol{\xi}} d\boldsymbol{\xi} \\ &= \sum_{i,j} f_{ij} \int_{\mathbb{R}^2} \delta(c_{ix} - \xi_1)\delta(c_{iy} - \xi_2) e^{\boldsymbol{\Xi}\cdot\boldsymbol{\xi}} d\boldsymbol{\xi} \\ &= \sum_{i,j} f_{ij} e^{\Xi_1 c_{ix}} e^{\Xi_2 c_{iy}}. \end{aligned} \tag{3.33}$$

Using the Taylor expansion of F one defines

$$\begin{aligned} F(\Xi_1, \Xi_2) &= \sum_{\alpha,\beta} \frac{1}{\alpha!\beta!} \frac{\partial^\alpha \partial^\beta}{(\partial\Xi_1)^\alpha (\partial\Xi_2)^\beta} F(\Xi_1, \Xi_2)\Big|_{\Xi_1=\Xi_2=0} \Xi_1^\alpha \Xi_2^\beta \\ &= \sum_{\alpha,\beta} \frac{1}{\alpha!\beta!} \underbrace{\sum_{i,j} (c_{ix})^\alpha (c_{iy})^\beta f_{ij}}_{m_{\alpha\beta}} \Xi_1^\alpha \Xi_2^\beta \\ &= \sum_{\alpha,\beta} \frac{1}{\alpha!\beta!} m_{\alpha\beta} \Xi_1^\alpha \Xi_2^\beta \end{aligned}$$

and hence

$$m_{\alpha\beta} = \frac{\partial^\alpha \partial^\beta}{(\partial\Xi_1)^\alpha (\partial\Xi_2)^\beta} F(\Xi_1, \Xi_2)\Big|_{\Xi_1=\Xi_2=0}. \tag{3.34}$$

The cumulants are defined as the coefficients of the Taylor expansion of the logarithm of the moment generating function. This yields for the cumulant $\kappa_{\alpha\beta}$:

$$\kappa_{\alpha\beta} = \frac{\partial^\alpha \partial^\beta}{(\partial\Xi_1)^\alpha (\partial\Xi_2)^\beta} \ln(F(\Xi_1, \Xi_2))\Big|_{\Xi_1=\Xi_2=0}. \tag{3.35}$$

The link from cumulant to moments can be established with the chain rule for differentiation. From Eq. (3.34) and Eq. (3.35) follows for $\alpha = \beta = 0$:

$$\kappa_{00} = \ln(F(0,0)) = \ln(m_{00}) = \ln(\rho).$$

All other cumulants are

$$\kappa_{00} = \ln(m_{00}) \tag{3.36}$$
$$\kappa_{10} = \frac{m_{10}}{m_{00}} \tag{3.37}$$
$$\kappa_{01} = \frac{m_{01}}{m_{00}} \tag{3.38}$$
$$\kappa_{11} = \frac{m_{11}}{m_{00}} - \frac{m_{10}m_{01}}{m_{00}^2} \tag{3.39}$$
$$\kappa_{20} = \frac{m_{20}}{m_{00}} - \frac{m_{10}^2}{m_{00}^2} \tag{3.40}$$
$$\kappa_{02} = \frac{m_{02}}{m_{00}} - \frac{m_{01}^2}{m_{00}^2} \tag{3.41}$$
$$\kappa_{21} = \frac{m_{21}}{m_{00}} - \frac{m_{20}m_{01}}{m_{00}^2} - 2\frac{m_{10}m_{11}}{m_{00}^2} + 2\frac{m_{10}^2m_{01}}{m_{00}^3} \tag{3.42}$$
$$\kappa_{12} = \frac{m_{12}}{m_{00}} - \frac{m_{10}m_{02}}{m_{00}^2} - 2\frac{m_{11}m_{01}}{m_{00}^2} + 2\frac{m_{10}m_{01}^2}{m_{00}^3} \tag{3.43}$$
$$\begin{aligned}\kappa_{22} = {} & \frac{1}{m_{00}}m_{22} \\ & - \frac{1}{m_{00}^2}\left(2m_{10}m_{12} + 2m_{21}m_{01} + 2m_{11}^2 + m_{20}m_{02}\right) \\ & + \frac{2}{m_{00}^3}\left(m_{10}^2m_{02} + 4m_{10}m_{11}m_{01} + m_{20}m_{01}^2\right) \\ & - \frac{6}{m_{00}^4}m_{10}^2m_{01}^2.\end{aligned} \tag{3.44}$$

As it readily can be seen, the zeroth cumulant κ_{00} is divisor in the calculation of cumulant which computationally is costly. However, normalizing the cumulants by the density m_{00}, the normalized cumulants are defined as

$$K_{\alpha\beta} \coloneqq m_{00}\kappa_{\alpha\beta}, \tag{3.45}$$

which computationally are more pleasant. A closer look into the calculated cumulant shows that the cumulants are equal to their corresponding order moments plus some additional terms that can be viewed as correction terms.

As we mentioned before, using the central moments instead of raw moments leads to Galilean invariance. Doing so, we will see that the way from central moments to cumulants is much more smooth, and not only results in more accuracy but also shows more efficiency in computation.

The central moments are equal to our normal moments when the frame of reference

is moved with the flow velocity. The particle distributions relative to the macroscopic flow velocity $\boldsymbol{u} = \begin{pmatrix} u_1 \\ u_2 \end{pmatrix}$ can be modified as

$$f^{central}(\boldsymbol{\xi}) \coloneqq \sum_{i,j} f_{ij}\delta((c_{ix} - u_1) - \xi_1)\delta((c_{iy} - u_2) - \xi_2).$$

Like in Eq. (3.33), the moment generating function $F^{central}$ of this distribution can be defined as

$$\begin{aligned} F^{central}(\Xi_1, \Xi_2) &\coloneqq \mathcal{L}[f^{central}](\boldsymbol{\Xi}) = \\ &= \int_{\mathbb{R}^2} \sum_{i,j} f_{ij}\delta((c_{ix} - u_1) - \xi_1)\delta((c_{iy} - u_2) - \xi_2)e^{\boldsymbol{\Xi}\cdot\boldsymbol{\xi}}d\boldsymbol{\xi} \\ &= \sum_{i,j} f_{ij}e^{\Xi_1(c_{ix}-u_1)}e^{\Xi_2(c_{iy}-u_2)}. \end{aligned} \tag{3.46}$$

Also, the Taylor expansion of $F^{central}$ yields to

$$F^{central}(\Xi_1, \Xi_2) = \sum_{\alpha,\beta} \frac{1}{\alpha!\beta!}\mathcal{C}_{\alpha\beta}\Xi_1^\alpha\Xi_2^\beta$$

so the definition of central moments can be found as

$$\mathcal{C}_{\alpha\beta} = \frac{\partial^\alpha\partial^\beta}{(\partial\Xi_1)^\alpha(\partial\Xi_2)^\beta}F^{central}(\Xi_1, \Xi_2)\Big|_{\Xi_1=\Xi_2=0}.$$

The central moments can be defined as

$$\begin{aligned} \mathcal{C}_{00} &= m_{00} \\ \mathcal{C}_{10} &= 0 \\ \mathcal{C}_{01} &= 0 \\ \mathcal{C}_{20} &= m_{00}\kappa_{20} \\ \mathcal{C}_{02} &= m_{00}\kappa_{02} \\ \mathcal{C}_{11} &= m_{00}\kappa_{11} \\ \mathcal{C}_{21} &= m_{00}\kappa_{21} \\ \mathcal{C}_{12} &= m_{00}\kappa_{12} \\ \mathcal{C}_{22} &= m_{00}(\kappa_{22} + 2\kappa_{11}^2 + \kappa_{20}\kappa_{02}). \end{aligned} \tag{3.47}$$

As we can see here, neglecting the scaling, the cumulants of non-conserved moments differ from central moments at order higher than 3.

The moment generating function of the Maxwell distribution Eq. (3.19) is defined as

$$\begin{aligned} F^{eq}(\Xi) = \mathcal{L}[f^{\text{maxwell}}](\Xi) &= \int_{\mathbb{R}^2} \rho \frac{m}{2\pi k_B T} \exp\left(-\frac{m \parallel \xi - u\parallel^2}{2k_B T}\right) \cdot e^{\Xi\cdot\xi} d\xi \\ &= \rho \exp\left(\Xi_1 u_1 + \Xi_2 u_2 + \frac{1}{4C}\left(\Xi_1^2 + \Xi_2^2\right)\right). \end{aligned} \tag{3.48}$$

The equilibrium cumulants, which is the Taylor series of the logarithm of the transformed equilibrium distribution, Eq. (3.48). With c_s defined as

$$c_s \coloneqq \sqrt{\frac{k_B T}{m}},$$

which is the definition of the speed of sound, the logarithm of Eq. (3.48) leads to

$$\begin{aligned} \ln(F^{eq}(\boldsymbol{\Xi})) &= \ln(\rho) + \Xi_1 u_1 + \Xi_2 u_2 + \frac{1}{4C}\left(\Xi_1^2 + \Xi_2^2\right) \\ &= \ln(\rho) + \Xi_1 u_1 + \Xi_2 u_2 + \frac{k_B T}{2m}\left(\Xi_1^2 + \Xi_2^2\right) \\ &= \ln(\rho) + \Xi_1 u_1 + \Xi_2 u_2 + \frac{c_s^2}{2}\left(\Xi_1^2 + \Xi_2^2\right). \end{aligned} \tag{3.49}$$

As Eq. (3.49) is a finite polynomial, its Taylor series is finite and equal to the function itself. Hence, the equilibrium cumulants are

$$\begin{aligned} \kappa_{00}^{eq} &= \ln(\rho) = \ln(m_{00}) \\ \kappa_{10}^{eq} &= u_1 = \frac{m_{10}}{m_{00}} \\ \kappa_{01}^{eq} &= u_2 = \frac{m_{01}}{m_{00}} \\ \kappa_{11}^{eq} &= 0 \\ \kappa_{20}^{eq} &= c_s^2 \\ \kappa_{02}^{eq} &= c_s^2 \\ \kappa_{21}^{eq} &= 0 \\ \kappa_{12}^{eq} &= 0 \\ \kappa_{22}^{eq} &= 0, \end{aligned} \tag{3.50}$$

where we used the moment representation of the macroscopic variables Eq. (3.5). Notice that in equation, Eq. (3.50), the Maxwell distribution is fully incorporated; hence, no truncation error introduced here.

The cumulant collision scheme is a linear interpolation between PDFs and their

equilibrium, similar to SRT scheme, as

$$\kappa^*_{\alpha\beta} \coloneqq \kappa^\circ_{\alpha\beta} + \omega_i \left(\kappa^{eq}_{\alpha\beta} - \kappa^\circ_{\alpha\beta}\right).$$

However, unlike the SRT, the relaxation rates are not restricted to just one parameter, but can be chosen for each cumulant.

3.5 Relaxation time

The utilization of the MRT was proposed to maximize the number of free relaxation time of the model to achieve the stability and accuracy. The relaxation times for the conserved moments and stresses, as shown in Eq. (3.30), are selected based on the physics of the problem. However, it is possible to enhance stability by controlling additional moments. These moments included kinetic or ghost moments that do not enter the bulk hydrodynamic equations. However, they play a major role at the boundaries and therefore affect accuracy.

The relaxation parameters corresponding to collision invariants ρ, and $\mathbf{j} := \rho\mathbf{u}$, denote conserved quantities during the collision, and hence, are set to zero in the absence of a force term. *Pan et al.* (2006) proposed that the remaining modes should be chosen as follows: (i) viscous stress vectors s_ν, which are related to the kinematic viscosity $\nu = \mu/\rho$ as $s_\nu = (3\nu + 0.5)^{-1}$, and (ii), set the kinetic modes s_q, s_π, s_h, s_e and s_ϵ to $s_\zeta = 8(2 - s_\nu)(8 - s_\nu)^{-1}$, which are also related to the kinematic viscosity. However, this sets of relaxation rates lead to viscosity-dependent position of the wall that is not physically possible.

As indicated in a recent study (*Khirevich et al.*, 2015), this problem can be solved if the aforementioned model is modified such that the symmetric energy modes, i.e., s_e, s_π and s_ϵ, keep the ratio $(1/s_\nu - 0.5)/(1/s_{\pi,\epsilon,e} - 0.5)$ constant given variation in s_ν.

In the TRT collision operation, the eigenvalue of the symmetric components is again related to the kinematic viscosity as $\omega^+ = s_\nu = (3\nu + 0.5)^{-1}$, and the second eigenvalue $\omega^- \in (0, 2)$ corresponds to a free parameter. For steady non-linear flow situations, it has been demonstrated (*Ginzburg et al.*, 2008b) that most of the macroscopic errors depend on the so-called "magic" parameter

$$\Lambda = \left(\frac{1}{\omega^+} - \frac{1}{2}\right)\left(\frac{1}{\omega^-} - \frac{1}{2}\right)$$

that is determined for the specific flow setup. The choice $\Lambda = \frac{1}{4}$ is given as an optimal value for the stability of the simulations. Another choice, namely $\Lambda = \frac{3}{16}$, which yields the exact location of bounce-back walls in case of a Poiseuille flow in a straight channel (*Ginzburg et al.*, 2008b; *Khirevich et al.*, 2015).

3.6 Grid refinement

Originally, LBM has been introduced with uniform grids. Therefore, grid refining is needed for the whole computational domain to resolve the fluid flow with sufficient resolution and this makes computation unnecessarily expensive. It is essential to decrease the computational cost, especially for multi-scale simulations in a large domain such as turbulent free flow over porous media. Several approaches of grid refinement were proposed to overcome this limitation (*Filippova and Hänel*, 1998; *Dupuis and Chopard*, 2003; *Chen et al.*, 2006).

The choice of the two different lattice grids, namely cell-based grid and node-based grid, for the original LBM implementation is a matter of taste. However, the difference is a relevant issue when local grid refinement is applied (*Rohde et al.*, 2006). In the node-based approach, the fine node lies directly on the interface of the refinement, while in the cell-based approach fine cell centers that exactly coincide with a corresponding coarse cell center are absent. This difference leads to two different categories of grid refinement, namely the node-based grid refinement *Filippova and Hänel* (1998); *Dupuis and Chopard* (2003); *Freudiger et al.* (2008), and the cell-based grid refinement, e.g., *Chen* (1998); *Rohde et al.* (2006); *Chen et al.* (2006); *Yu and Fan* (2009).

In this study, static cell-based grid refinement is utilized for the simulation presented in chapter 7. The following briefly describes the volumetric grid-refinement that is a cell-based approach. For further details on the block-structure, adaptive refinement with load-balancing and the benchmarking, readers can refer to extant studies (*Staubach*, 2013; *Schornbaum and Rüde*, 2016).

In the cell-based approach, communication between coarse and fine grids is performed in a shared layer as an interface. The interface has a total overlapping area size of $2\Delta x_c$, which c denotes the coarse cells. In a D-dimensional space, a fine grid requires 2^D times the number of interface cells in a corresponding coarse grid.

The basic grid-refinement algorithm used in this study is summarized as follows:

- Step 1: communication step in both directions
- Step 2a: Propagation step on both grids
- Step 2b: Collision step on both grids
- Step 3: Communication step from the coarse direction to fine direction
- Step 4a: Propagation step on the fine grid only
- Step 4b: Collision step on the inner fine grid only

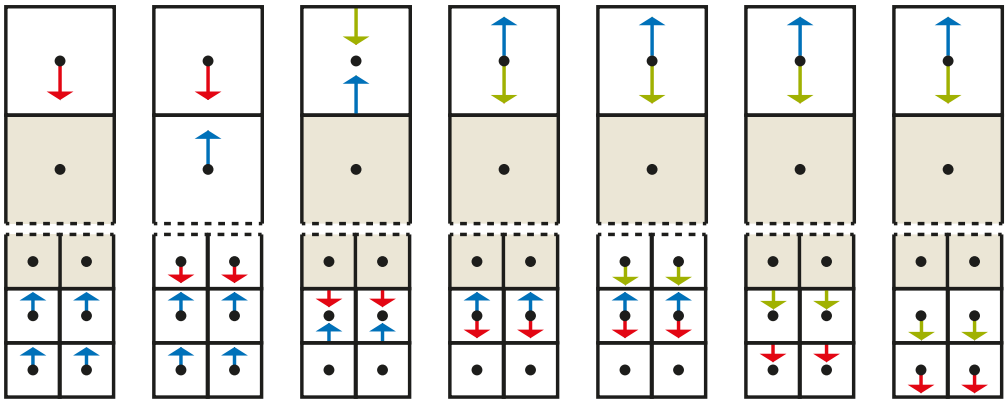

Figure 3.2: Grid refinement algorithm with uniform explosion operation. The distribution functions are exchanged using interface cells (gray color). Arrows pointing outwards with respect to the cell center denote post-collision data, arrows pointing towards the cell center denote post-propagation values.

The algorithmic scheme is shown in Fig. 3.2. The synchronous communication step involves the uniform explosion, i.e., the outgoing distribution functions of a coarse interface cell are uniformly distributed among the corresponding fine cells. The PDFs are then propagated from the interface in the direction to the inner domain as shown in Fig. 3.2. Following this, the collision step is conducted in both grids. In this step, the fine cells carry post-collision solutions at time $t + \Delta t_f$, while the data in the coarse inner cell is at time $t + \Delta t_c$. The streaming step is performed on the fine grid prior to the occurrence of the second collision. The second collision is only performed for the fine grid except for the cells located in the overlap region in which the distribution functions are only streamed. Prior to the re-occurrence of the collision on both grids, the missing incoming distributions of a coarse interface cell are reconstructed from the arithmetic mean of the incoming distributions of the corresponding child cells.

Acoustic scaling is applied in the algorithm such that the fine grid performs twice the number of time steps in comparison to that of the coarse grid (*Freudiger et al.*,

2008). This scheme is called nested time-stepping scheme and it is briefly shown in Fig. 3.3. With this scheme, the speed of sound remains constant. To keep the Reynolds number constant in each level, the viscosity should remain constant. Therefore, the relaxation rate at level L is defined as

$$\begin{aligned} \nu_L = \nu_0 \;\Rightarrow\; c_s^2\left(\frac{1}{\omega_L}-\frac{1}{2}\right)\Delta t_L &= c_s^2\left(\frac{1}{\omega_0}-\frac{1}{2}\right)\Delta t_0 \\ \xrightarrow{\Delta t_L=\Delta t_0/2^L} \omega_L &= \frac{2\omega_0}{2^{L+1}+(1-2^L)\omega_0}, \end{aligned} \tag{3.51}$$

where the subscript 0 denotes the coarsest level. For the TRT, Eq. (3.51) is used for the ω^+, and the ω^- is defined by keeping the magic number constant and calculating with ω^+ in the corresponding level.

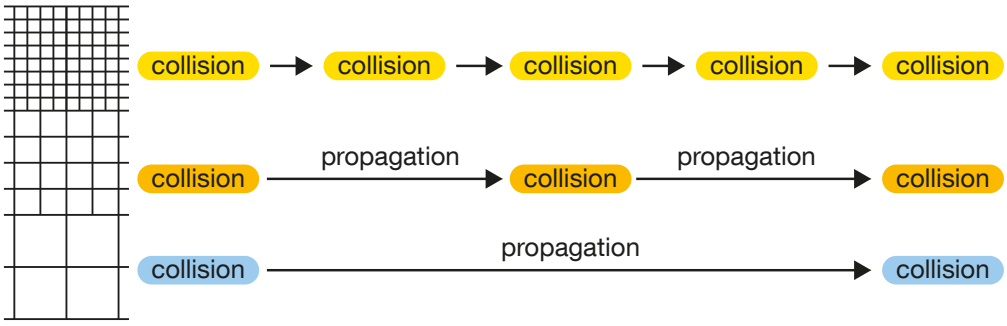

Figure 3.3: Nested time-stepping scheme in the grid-refinement. Three different levels of grid-refinement are shown.

3.7 Errors in the LBM

The LBE has been shown to recover the incompressible Navier–Stokes equation by the Chapman–Enskog asymptotic procedure (*Sterling and Chen*, 1996). The Chapman-Enskog expansion includes a Taylor series expansion of $f_i(x+e_i\Delta t, t+\Delta t)$ about $f_i(x,t)$, and f_i about f_i^{eq}, as well as an expansion of time. If the viscosity is defined as $\nu \propto (2\tau-1)\Delta x^2/\Delta t$, then the LB equation can satisfy the Navier-Stokes equation. However, employing this procedure lead to errors of the LBM in the same order as the viscous term, $O(\epsilon)$, as well as additional errors from the terms in the order of $O(\epsilon^2)$. The reason for this unclear analysis of the truncation error is that the Chapman–Enskog uses multiple time scales which makes it hard to analyze higher order terms.

The compressibility is measured by the Mach number, $Ma = u/c_s$, in which u is the bulk velocity and c_s is the speed of sound. It is worth to note that the speed of sound

in the LBM, is the transport of the information in the model. *Reider and Sterling* (1995) showed that the LB equation can recover the compressible Navier–Stokes with additional terms of order $O(Ma^2)$. The finite size effect is determined by the Knudsen number (Kn) that is the ratio of the mean-free-path to the characteristic length. The Knudsen number is related to the Reynolds number and Mach number by $Re = Ma/Kn$. Therefore, the compressibility error consists of the terms of Knudsen number squared, Mach number cubed and the Navier–Stokes compressibility terms. *Reider and Sterling* (1995) pointed out that convergence to the incompressible Navier–Stokes is only possible if the compressibility error is less than the discretization error. Although the common LBM, uses a first-order upwind on the left-hand side, since the viscosity covers all second-order terms in the truncation error, this scheme performs as second-order model. The results indicated that, if the discretization is performed with the fourth-order finite-difference methods, then it also performs fourth-order convergence for sufficiently small Mach number. However, a smaller Mach number increases the time required for accurate results because of the smaller time step involved. Therefore, the most efficient way is to choose the Mach number in a way that the compressibility error is in the same order as the discretization error. With this approach, the effective temporal convergence of the LBM is of first-order.

Holdych et al. (2004) performed a truncation error analysis and found that for the fixed lattice spacing, LBM converges second-order temporally. They also pointed out that if the refining is done with constant $\Delta x^2/\Delta t$, then LBM converges with second-order in space and temporally converges with first-order. Numerical simulations also confirm that the model converges spatially with second-order if the relaxation time is kept constant (*Skordos*, 1993).

In the LBM, in addition to the traditional grid-spacing errors, the errors also depend on the relaxation parameter. Therefore, for the SRT in which a relaxation time controls all moments, higher order truncation error will depend on the relaxation time, and thereby on the viscosity. This deficiency can be solved by using the TRT and MRT collision operator which will be analyzed in chapter 4.

An error exists due to the inability of the regular lattice to accurately represent the geometry of the solid. The LBM uses a Cartesian mesh for the computational domain. Hence, it creates roughness in the form of "staircases" on the solid boundaries. Therefore, it is not possible to represent the actual position of the wall by a simple bounce-back boundary condition. We shall discuss this issue in the Sec. 3.9.

3.8 Unit conversion

The LBM is supposed to model the physics of real phenomena. Therefore, this involves the usual question of selecting the parameters in a mesoscopic scale that represents the same physics on the macroscopic scale. First, it is necessary that the system be equivalent to the defined physical system. Second, the parameters should be defined such that they satisfy accuracy and stability limits of LBM.

To find appropriate parameters in the LBM simulation, the physical system should first be converted to the dimensionless system, which is an intermediate scale that is independent of both macroscopic and mesoscopic scales. This step is done by using the governing dimensionless numbers, e.g., Reynolds number for fluid flow. Dimensionless numbers allow for the comparison of different scales, and they also show the relation between different phenomena. It is crucial to find a right dimensionless number to create the dimensionless system. The dimensionless system can now be converted to the mesoscopic scale, i.e., lattice units. This step consist in choosing the required resolution, and the parameters, such as velocity and relaxation time, that can satisfy stability and accuracy limits.

On certain occasions, it is not straightforward to define the relevant dimensionless numbers for the simulation, and the conversion must be based on the reference length, time, and mass. The key question for this approach involves finding the right reference time. There is no straightforward way to choose the reference time. In the explicit numerical schemes, this is usually related to the stability limit, and is selected by the relation $\delta_t \sim \delta_x^2$. In the LBM method, there are other limitations over the stability problem. For example, the velocity, which in the LBM unit is $u \sim \delta_t/\delta_x$, should be small in comparison to the speed of sound that is usually chosen as $1/\sqrt{3}$, to satisfy the incompressibility assumption. As it is mentioned in Sec. 3.7, the compressibility error scales like $O(Ma^2)$, and recall that the Mach number is u/c_s. Therefore, the compressibility error is scaling with δ_t^2/δ_x^2. On the other hand, the discretization error scales with δ_x^2 as a second order method. The second-order spatial convergence is only guaranteed if these two errors are equal, i.e., $\delta_t^2/\delta_x^2 \sim \delta_x^2$. This leads to the relation $\delta_t \sim \delta_x^2$ which is the same as other explicit methods as well.

3.9 Boundary conditions [2]

Because of the kinetic nature of LBM, the boundary conditions are fundamentally different from the traditional CFD models, e.g., finite volume methods. In the LBM, when the PDFs leave the computational domain, they have to be replaced either with a given a priori value or a computed one from the condition. Since the perfect knowledge of the particle behavior in the kinetic is not available, they usually will be approximated such that the cell approximately exhibits the macroscopic condition. This mismatch leads to a slip boundary instead of a no-slip boundary. As in the case of all numerical methods, the mismatch to the exact macroscopic value at the boundary cells influences the solution in the whole simulation domain. Therefore, a careful consideration of the boundary condition in the LBM simulation is necessary.

Typically, two types of boundary conditions are encountered in pore-scale simulations. The first condition is a *solid-wall interaction* of fluid particles that come into contact with the porous geometry. This type of boundary is called bounce-back (BB) which represents the no-slip boundary condition on the macroscopic scale. The second boundary condition is a *periodic pressure forcing* that is applied to drive the flow by a pressure gradient. The successful simulation should have a correct implementation of the boundary condition, which in LBM is to find the unknown particle distribution function after the streaming step.

3.9.1 Simple bounce back

Simple bounce-back (SBB) is the most common boundary condition in which the particle is assumed to bounce-back to fluid nodes after colliding with a wall. Therefore, zero velocity is satisfied in the wall position. There are two types of SBB, namely the on-site model (*Behrend*, 1995) that is implemented on the solid cell and implies a no-slip velocity at the solid cell, and the mid-plane model (*Ladd*, 1994) that represents the wall position in the mid-grid-spacing of the solid cell and the fluid cell. The first SBB only provides first order accuracy, while the second SBB results in second-order accuracy in the mesh aligned walls (*Ginzbourg and d'Humières*, 1996; *Luo*, 1997). Various schemes considered in this study are outlined in the following.

[2] Most parts of this section are published in "E. Fattahi, C. Waluga, B. Wohlmuth, U. Rüde, M. Manhart, and R. Helmig, Lattice Boltzmann methods in porous media simulations: From laminar to turbulent flow, Computers and Fluids, 140 (2016), 247 – 259."

In the SBB scheme, the wall location is represented by a zeroth order interpolation (staircase approximation), and the collision of particles with the wall is incorporated by mimicking the bounce-back phenomenon of the particle reflecting its momentum upon collision with the wall, which is supposed to happen half-way between the solid and fluid nodes. Hence, the unknown distribution function is calculated as:

$$f_{\bar{k}}(x_{f_1}, t_{n+1}) = \tilde{f}_k(x_{f_1}, t_n). \tag{3.52}$$

where we recall that $\bar{k}$ is the diametrically opposite direction to k, and we take the values $\widetilde{f}_k$ after collision but before streaming on the right hand side.

As mentioned in Sec. 3.7, the bounce-back boundary represents the wall with the zig-zag approximation. However, in complex geometries, the wall position is not always located half-way on a regular lattice. Hence, especially at coarse resolutions, this boundary treatment introduces severe geometric errors, which in turn lead to boundary layer effects that can be particularly problematic in porous media of low porosity, where solid nodes occupy the large part of the domain. Thus, a discretization that adequately resolves the solid boundaries is often computationally prohibitive since the meshes tend to become exceedingly large.

Thus, several advanced schemes have been proposed to represent boundaries that are not mesh aligned more accurately. Three types of boundary conditions are offered to deal with curved boundaries. The first strategy is to use body-fitted meshes to fit the boundary, in which the entire domain will use this mesh structure. The second approach is to use spatial interpolations but using Cartesian mesh in the domain (*Bouzidi et al.*, 2001b; *Mei et al.*, 2000; *Ginzburg and d'Humières*, 2003; *Yu et al.*, 2003; *Lallemand and Luo*, 2003; *Chun and Ladd*, 2007). Using the latter, interpolation or extrapolation depends on the exact position of the wall between the solid cell and fluid cell. The immersed boundary (*Pinelli et al.*, 2010; *Peskin*, 1977) is another approach that is used to model the boundary cells in the LB simulation (*Feng and Michaelides*, 2004). Because of the simplicity of the applicability and the reliability of the interpolation types boundaries, it has been used most commonly.

3.9.2 Interpolating bounce back

Let x_{f_i} denote a lattice node which at a distance of at most $i > 0$ cells from the boundary and let $q = |x_{f_1} - x_w|/|x_{f_1} - x_b|$ define the normalized wall distance; as shown in Fig. 3.4. Bounce-back schemes based on higher order interpolations require more

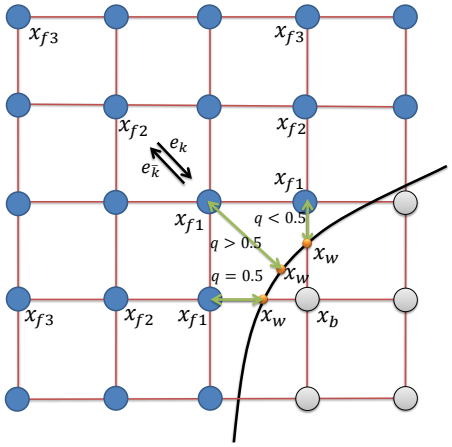

Figure 3.4: Example of the different distances of the wall to the first fluid node, simple bounce-back happens when the value of $q = 1/2$, lower or higher value of q emerges the need of interpolated bounce-back schemes. For simplicity, we only display a two-dimensional illustration.

than one fluid node between nearby solid surfaces. During the stream-collide step, the perfect mid-plane BB considers that the particle starts from the fluid cell (x_{f1}) travels mid-grid-spacing towards the wall, collide with the wall and at x_w, reverse its momentum and travels back to the fluid cell again. Therefore, the unknown particle distribution function at x_{f1} can be defined as Eq. (3.52). However, if the wall is not in the mid-grid-spacing of the wall cell and fluid cell, then the particle might end up somewhere that there is no cell there. The parameter q can help to distinguish various situation; as in Fig. 3.4. If $q = 0.5$, perfect mid-plane BB is applied. If $q < 0.5$, then the particle after the stream-collide step ends up at a position between x_{f1} and x_{f2}, and if $q > 0.5$, then it ends up at a position between x_w and x_{f1}. These situations can be handled by using the interpolation schemes, which correct the SBB with additional terms, by using the known PDFs.

Here we describe five common interpolating boundary condition schemes to deal with curved boundaries, namely, the linear interpolation bounce-back (*Bouzidi et al.*, 2001b), the quadratic extension (*Lallemand and Luo*, 2003), the interpolation/extrapolation bounce back (*Mei et al.*, 2000), the multi-reflection (*Ginzburg et al.*, 2008b) scheme and the central linear interpolation (*Ginzburg et al.*, 2008b) scheme.

Linear interpolation bounce-back (LIBB)

Bouzidi et al. (2001b) proposed a linear interpolation to correct the bounce-back for

the curved boundary, which the interpolation scheme is given by

$$f_{\bar{k}}(x_{f_1}, t_{n+1}) = \begin{cases} (1-2q)\tilde{f}_k(x_{f_2}, t_n) + 2q\tilde{f}_k(x_{f_1}, t_n), & q < 1/2, \\ \left(1 - \frac{1}{2q}\right)\tilde{f}_{\bar{k}}(x_{f_1}, t_n) + \frac{1}{2q}\tilde{f}_k(x_{f_1}, t_n), & q \geq 1/2. \end{cases} \tag{3.53}$$

In this scheme the interpolation of the particle distribution function $f_{\bar{k}}(x_{f_1}, t_{n+1})$ is formulated based on different lattice cell and time-step according to the situation of the particle after the stream-collide step, i.e., $q < 0.5$ or $q \geq 0.5$. *Lallemand and Luo* (2003) used similar scheme for moving boundaries.

Quadratic interpolation bounce-back (QIBB)

One can also use quadratic interpolation to obtain the QIBB scheme (*Lallemand and Luo*, 2003), where the unknown distribution function would be calculated as:

$$f_{\bar{k}}(x_{f_1}, t_{n+1}) = \begin{cases} q(1+2q)\tilde{f}_k(x_{f_1}, t_n) + (1-4q^2)\tilde{f}_k(x_{f_2}, t_n) - q(1-2q)\tilde{f}_k(x_{f_3}, t_n), & q < 1/2, \\ \left(\frac{2q-1}{q}\right)\tilde{f}_{\bar{k}}(x_{f_1}, t_n) + \frac{1}{q(2q+1)}\tilde{f}_k(x_{f_1}, t_n) + \frac{1-2q}{2q+1}\tilde{f}_{\bar{k}}(x_{f_2}, t_n), & q \geq 1/2. \end{cases} \tag{3.54}$$

The QIBB boundary scheme uses three neighbor cells to interpolate the unknown PDF, while the LIB uses two neighbor cells. If the neighboring cell does not exist, it is proposed to fall back to SBB. However, this decreases the accuracy of the scheme.

Interpolation/extrapolation bounce-back (IEBB)

Filippova and Hänel (1998) were the first who tried to introduce a curved boundary condition with second-order accuracy. They used the Chapman–Enskog analysis to motivate this boundary condition and assumed that the intrinsic time scale of the unsteady flow must be large compared with the advection time on the lattice scale. However, it has been found that it is somewhat unstable (*Mei et al.*, 2000). *Mei et al.* (2000) proposed an improvement (referred to from now on as IEBB scheme) over this boundary and demonstrated its applicability in 3D simulation.

The idea of the *Mei et al.* (2000) was to correct the SBB by using an auxiliary equilibrium distribution function and a weighting factor χ. Applying a process of linear interpolation, they proposed to find the unknown PDF as

$$f_{\bar{k}}(x_{f_1}, t_{n+1}) = (1-\chi)\tilde{f}_k(x_{f_1}, t_n) + \chi f_k^*(x_b, t_n). \tag{3.55}$$

The auxiliary equilibrium function is defined as

$$f_k^*(x_b,t_n) = w_k\left\{\rho+\rho_0\left[\tfrac{3}{c^2}\boldsymbol{e}_k\cdot\boldsymbol{u}_{bf}+\tfrac{9}{2c^4}(\boldsymbol{e}_k\cdot\boldsymbol{u}_{x_{f_1}})^2-\tfrac{3}{2c^2}\boldsymbol{u}_{x_{f_1}}\cdot\boldsymbol{u}_{x_{f_1}}\right]\right\}, \tag{3.56}$$

where the velocity at the wall is computed via

$$\boldsymbol{u}_{bf} = \begin{cases}\boldsymbol{u}_{x_{f_2}}, & q<1/2,\\ \left(1-\frac{3}{2q}\right)\boldsymbol{u}_{x_{f_1}}, & q\geq 1/2.\end{cases}$$

Once $\boldsymbol{u}_{bf}$ is defined, the weighting factor can be defined as $\chi=(2q-1)/(1/\omega-2)$ for $q<\frac{1}{2}$, while for $q\geq\frac{1}{2}$ we let $\chi=(2q-1)/(1/\omega+1/2)$. In this study we set $\omega=\omega^+$ in case of the TRT scheme and $\omega=s_\nu$ in case of the MRT scheme.

The main difference between IEBB scheme, and LIBB and QIBB schemes is that the IEBB formulates an auxiliary equilibrium at the solid cell and then execute the collision at that point, while the latter schemes interpolate the unknown value without collision scheme.

Multi-reflection (MR)

Ginzburg and d'Humières (2003) extended the results of (*Bouzidi et al.*, 2001b) such that the boundary leads to third-order accuracy. The boundary condition is introduced as a closure relation between an unknown PDF and some of the known PDFs of the fluid cell. Taylor expansion of the result at the boundary shows a second order deviation from the ideal solution, such that if the deviation is zero, it performs as a third-order boundary condition. However, there is a solution for some specific flows and geometry, e.g., Poiseuille flow in a cell aligned channel.

The multi-reflection (MR) is an approach to obtain highly accurate bounce-back conditions (*Ginzburg and d'Humières*, 2003; *Ginzburg et al.*, 2008b), which reads as

$$\begin{aligned} f_{\bar{k}}(x_{f_1},t_{n+1}) = {} & \tfrac{1-2q-2q^2}{(1+q)^2}\tilde{f}_k(x_{f_2},t_n)+\tfrac{q^2}{(1+q)^2}\tilde{f}_k(x_{f_3},t_n)\\ & -\tfrac{1-2q-2q^2}{(1+q)^2}\tilde{f}_{\bar{k}}(x_{f_1},t_n)-\tfrac{q^2}{(1+q)^2}\tilde{f}_{\bar{k}}(x_{f_2},t_n)+\tilde{f}_k(x_{f_1},t_n)+F_k^{pc}, \end{aligned} \tag{3.57}$$

where F_k^{pc} is the post-collision correction term. The post-correction term is related to the third-order moments and for the MRT we use the one presented in *Ginzburg and d'Humières* (2003) for the MR1 model. This reads as $F_k^{pc}=-\frac{4\Lambda_k}{3\nu(1+q)^2}f_k^{(2)}$ with $\Lambda_k=(1/s_\nu-0.5)/(1/s_k-0.5)$, and f_k^2 is obtained from the third-order non-equilibrium

and can be calculated as

$$\boldsymbol{f}^{(2)} = \boldsymbol{M}^{-1}\boldsymbol{S}[\boldsymbol{t} - \boldsymbol{t}^{eq}] \tag{3.58}$$

where $\boldsymbol{t}$ are the third-order moments.

The correction term for the TRT collision is employed as it is introduced in (*Ginzburg et al.*, 2008b) as

$$F_k^{pc} = \frac{4}{(1+q)^2}\omega^-(\frac{1}{\omega^-} - \frac{1}{2})(f^- - f^{eq-}). \tag{3.59}$$

It is worth to mention that the non-equilibrium term should be calculated before the collision.

Note that this scheme must access five distribution values at three fluid nodes to effect the update.

Central linear interpolation bounce-back (CLI)

A computationally cheaper variant is given by (*Ginzburg et al.*, 2008b) as the central linear interpolation scheme (CLI), which only requires three values at two fluid nodes, i.e.,

$$f_{\bar{k}}(x_{f_1}, t_{n+1}) = \tfrac{1-2q}{1+2q}\tilde{f}_k(x_{f_2}, t_n) - \tfrac{1-2q}{1+2q}\tilde{f}_{\bar{k}}(x_{f_1}, t_n) + \tilde{f}_k(x_{f_1}, t_n). \tag{3.60}$$

It should be noted that neither of the two latter schemes involves a distinction of cases for different values of q, which allows for an efficient implementation. We note that the CLI scheme can also be modified with a post-collision correction f_k^{pc} in order to eliminate the second-order error for steady flows. This additional correction is not considered in the present study, but we refer to (*Ginzburg et al.*, 2008b; *Khirevich et al.*, 2015) for a further discussion and results.

3.9.3 Periodic pressure boundary condition

In many applications, fluid flow is driven by a pressure difference. For incompressible flow, the corresponding periodicity boundary conditions can be written as

$$\boldsymbol{u}(\boldsymbol{x} + L\,\boldsymbol{i}, t) = \boldsymbol{u}(\boldsymbol{x}, t), \qquad p(\boldsymbol{x} + L\,\boldsymbol{i}, t) = p(\boldsymbol{x}, t) + \Delta p, \tag{3.61}$$

where L is the length of the domain in the periodic direction $\boldsymbol{i}$, and $\Delta p/L$ is the pressure gradient applied between the inlet and outlet boundaries of the domain.

In LBM-based approaches, applying this type of boundary condition is not straightforward. Simply adjusting the corresponding pressures at the inlet and outlet boundaries produces non-physical mass defects at the periodic boundary, as was reported e.g. for Poiseuille flow in *Dupuis* (2002). The most commonly employed approaches replace the pressure gradient by incorporating an equivalent body force; see e.g. *Martys et al.* (1998); *Buick and Greated* (2000); *Guo et al.* (2002); *Mohamad and Kuzmin* (2010); *Huang et al.* (2011). However, these approaches suffer from the inability to predict the pressure gradient accurately for flow situations in general geometries (*Chen and Doolen*, 1998; *Zhang and Kwok*, 2006; *Kim and Pitsch*, 2007; *Gräser and Grimm*, 2010). For porous media applications, where we face complex pore geometries, it is desirable to have a boundary condition that is not lumped into a volume forcing and hence does not rely on rough predictions of the pressure field. In this work, we employ a pressure boundary condition which can be applied for incompressible periodic flows. Here we specify the equilibrium distribution function f_i^{eq} and the non-equilibrium distribution $f_i^{neq} = f_i - f_i^{eq}$ separately, as we shall describe below. As the extension to multiple periodic boundaries is straightforward, we consider in our description an essentially one-dimensional setting in which flow propagates from the left (L) to the right (R) boundary:

Since the pressure is related to the density via the equation of state $p = \rho c_s^2$, we consider a density difference instead of pressure difference in the following. The density at the left boundary is obtained by

$$\rho_L = \rho_R + \Delta\rho. \tag{3.62}$$

Regarding the relaxation dynamics of the non-equilibrium distribution, in the presence of the periodic boundaries, it can be approximated as

$$f_{i,L}^{neq} = f_{i,R}^{neq}. \tag{3.63}$$

Now by using the above formulations, the unknown distribution functions can be computed as

$$f_{i,L} = f_{i,R}^{neq} + f_{i,R}^{eq}(\rho_L, \boldsymbol{u}_R), \tag{3.64}$$

$$f_{i,R} = f_{i,L}^{neq} + f_{i,L}^{eq}(\rho_R, \boldsymbol{u}_L). \tag{3.65}$$

Since the momentum in a periodic channel does not change, the implementation of

this approach is simple. For instance, by considering Eq. (3.24), the update Eq. (3.64) and Eq. (3.65) can be performed as:

$$f_{i,L} = f_{i,R} + w_k \Delta\rho, \tag{3.66}$$

$$f_{i,R} = f_{i,L} - w_k \Delta\rho. \tag{3.67}$$

3.10 Software framework WALBERLA

With the rise of extremely capable supercomputers, the direct numerical simulation (DNS) has been established as a third possibility for the analysis of homogenized models that can complement the classical experimental and the rigorous mathematical averaging approaches. In the past two decades, the class of lattice Boltzmann methods (LBM) has attracted the interest of researchers in CFD-related areas. In contrast to traditional CFD approaches based on the conservation of macroscopic quantities like mass, momentum, and energy, the LBM models the fluid by the kinetics of discrete particles that propagate (streaming step) and collide (relaxation step) on a discrete lattice mesh. Due to this kinetic nature, microscopic interactions in the fluid flow can be handled even in complex geometries, such as in microfluidic devices or in porous media (*Singh and Mohanty*, 2000; *Bernsdorf et al.*, 2000; *Kim et al.*, 2001). Moreover, due to the inherently local dynamics, an efficient implementation and parallelization of both fundamental algorithmic stages of the LBM is possible which allows to harness the computational power of currently available and emerging super-computing architectures (*Peters et al.*, 2010; *Schönherr et al.*, 2011; *Feichtinger et al.*, 2011).

The inherently local dynamics used in LBM afford efficient implementation and parallelization of both of the fundamental algorithmic stages. This allows to harness the computational power of currently available and emerging supercomputing architectures (*Peters et al.*, 2010; *Schönherr et al.*, 2011; *Feichtinger et al.*, 2011; *Fattahi et al.*, 2016a).

In this study, we use WALBERLA framework (widely applicable Lattice-Boltzmann from Erlangen) (*Feichtinger et al.*, 2011), which is specifically designed to be used for massively parallel fluid flow simulations. Basically, it is a general-purpose software framework to support various numerical methods for the simulations on the high-performance computers. It is prepared to be generic, extensible for parallelization, domain partitioning, input and output, and the simulations models.

3.10.1 Software concepts

WALBERLA is written in C++ to support modular and portable software design, and it can be compiled with all major compilers(GCC, Visual Studio, Clang, Intel C++ Compiler) on different operating systems (Linux, Windows). It supports the parallelization with OpenMP, MPI, and hybrid parallel execution that OpenMP threads are executed per MPI process. Specifically, for the fluid flow simulations, this enables us to compute problems with resolutions of more than one trillion (10^{12}) cells and up to 1.93 trillion cell updates per second using 1.8 million threads (*Godenschwager et al.*, 2013).

The modular structure of this framework allows for the implementation of new LBM schemes and models.

3.10.2 Stream-Collide class

In the lattice Boltzmann scheme, the computation is typically split into a collision and streaming step, which are given as

$$\tilde{f}_k(\boldsymbol{x}, t_n) - f_k(\boldsymbol{x}, t_n) = \Delta t \, g_k(\boldsymbol{x}, t_n), \qquad \text{(collision)}$$
$$f_k(\boldsymbol{x} + \boldsymbol{e}_k \Delta t, t_{n+1}) = \tilde{f}_k(\boldsymbol{x}, t_n), \qquad \text{(streaming)}$$

respectively, for $k = 0, \ldots, q$. The execution order of these two steps is arbitrary and may vary from code to code for implementation reasons. For instance, in WALBERLA, the order is first streaming and then the collision. This has the benefit that the stream and collision steps can be fused and that the macroscopic values need not be stored and later retrieved from memory.

3.11 Summary

In this chapter, the lattice Boltzmann method is explained, and different aspect of the method is described to evaluate the method for porous media flow. Next chapter will present results of the evaluation of flow through simple sphere pack in a wide range of Reynolds number.

4 Evaluation of LBM for porous media [1]

Having immense computational power at hand is not enough to solve relevant problems: due to the explicitness of classical LBM methods the spatial and temporal discretization characteristics are strongly coupled. Hence, we should take special care for pore-scale simulations to properly incorporate the physics at the boundaries and inside the domain without over-resolving the problem. Moreover, it is essential to accurately evaluate the boundary conditions and collision models that are effective from the Stokes regime to the inertial and turbulent flow regimes.

4.1 Introduction

An accurate and computationally efficient implementation of the no-slip boundary condition requires a suitable combination of collision and boundary operators. The most common boundary condition in LBM simulations is the simple bounce-back scheme, which also can be easily modified for the moving solid boundaries (*Ladd*, 1993). As we mentioned in Sec. 3.9.1, the SBB approximate the wall position at half-way between the solid and fluid nodes, but the exact position depends on the geometry, i.e., the orientation of the solid wall. To do the simulation with coarser resolution and higher accuracy, many improved boundary conditions have been proposed (see Sec. 3.9.2). However, theses methods are computationally more expensive than the SBB, and their accuracy and efficiency have to be evaluated. Another important issue is that these boundaries may lead to different results with different collision scheme (*Pan et al.*, 2006; *Chun and Ladd*, 2007).

A common way to simulate pressure driven flow is to replace the pressure gradient with an equivalent body force and applying stream-wise periodic boundary conditions. However, previous studies (*Chen and Doolen*, 1998; *Zhang and Kwok*, 2006; *Kim*

[1] Most parts of this chapter are published in "E. Fattahi, C. Waluga, B. Wohlmuth, U. Rüde, M. Manhart, and R. Helmig, Lattice Boltzmann methods in porous media simulations: From laminar to turbulent flow, Computers and Fluids, 140 (2016), 247 – 259."

and Pitsch, 2007; *Gräser and Grimm*, 2010) show that using this approach does not lead to correct flow fields for the flow through complex geometries, e.g., in porous media. In this study, we drive the flow by imposing the pressure gradient while applying the periodic boundary condition in stream-wise direction and allow it to develop based on the geometry.

The accuracy and convergence rates of different boundary conditions for flow in the Stokes regime, are investigated in Sec. 4.2. Also, the computational costs of different boundary schemes are assessed to choose the best combination for highly resolved simulations in high Reynolds numbers flow. After finding a suitable configuration, we then examine the spatial convergence of the boundary schemes in the laminar steady and fluctuating flow regime in Sec. 4.3.

We compare five different interpolating boundary condition schemes to deal with curved boundaries, namely, the linear interpolation bounce-back (LIBB, (*Bouzidi et al.*, 2001b)), the quadratic extension (QIBB, (*Lallemand and Luo*, 2003)), the interpolation/extrapolation bounce back (IEBB, (*Mei et al.*, 2000)), the multi-reflection (MR, (*Ginzburg et al.*, 2008b)) scheme and the central linear interpolation (CLI, (*Ginzburg et al.*, 2008b)) scheme.

Using the results of this evaluation, in Sec. 4.3 we simulate the flow through a simple sphere pack for two different solid volume fractions and investigate the effect of lattice velocity sets on the drag force and permeability in high Reynolds number flow by comparing the full and the reduced stencil lattice models.

4.2 Pore-scale simulation at $Re \ll 1$

To verify the implementation and assess the quality of different schemes we will evaluate different combinations of the LBM strategies discussed in chapter 3 in the Darcy regime. Since the flow in the Darcy (Stokes) regime is linear and irrotational, we conduct our simulations using the D_3Q_{19} lattice model. We consider flow through a periodic array of spheres arranged on a regular lattice as depicted in Fig. 4.1. To quantify the errors, we compute the dimensionless drag coefficient

$$C_D = \frac{F_D}{6\pi\mu U r} \quad , \tag{4.1}$$

where r is the sphere radius, F_D is the drag force acting on the sphere and U is the volume averaged velocity (Darcy velocity).

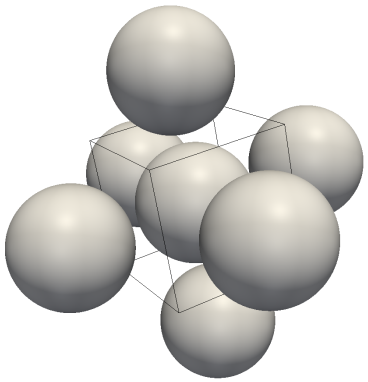

Figure 4.1: 3D view of simple sphere array with equal radii.

To reduce computational cost, we compute the wall distances required for the higher-order boundary conditions only once before the time-stepping loop begins and reuse it in each boundary handling step. This pre-calculation is possible because we are assuming non-deformable spheres. Moreover, we exploit the periodicity in the domain and consider only one cubic representative elementary volume (REV) containing a single sphere. For details on boundary handling, we refer to the previous Sec. 3.9.

In the following sections, we shall summarize our results related to the spatial discretization effect, as well as the undesired effect of viscosity dependence of the schemes.

4.2.1 Convergence analysis

In this test, we change the size of the sphere and increase the computational domain accordingly, such that the relative solid volume fraction is fixed to $\chi = D/L = 0.6$. Although *Sangani and Acrivos* (1982) prepared a semi-analytical solution for a simple cubic sphere pack based on the solid volume fraction, the correlated limits are not sufficient to evaluate the convergence rate of the boundary conditions. Therefore, first, we find the limit value of each boundary condition by least-squares curve fitting. Subsequently, we calculate the convergence rate of the corresponding boundary scheme. We compute the dimensionless drag force C_D and consider the relative error $|C_D/C_{D,\infty} - 1|$. In this section, the magic number is set to $3/16$ in which the interpolation boundary schemes result in better accuracy (*Khirevich et al.*, 2015). Our results are plotted in Fig. 4.2 and Fig. 4.3.

We can confirm that the higher-order boundary conditions converge with a higher order than the SBB boundary scheme which is expected to be asymptotical of the first order. As Fig. 4.3(a) indicates, all of the interpolation boundary schemes almost have second-order accuracy when combined with the SRT model. Moreover, for this example, we observe that the MR scheme converges with third order.

In Fig. 4.3(b) and Fig. 4.3(c), we list the results for the TRT and MRT models, respectively. Here we observe a difference between the CLI and the MR schemes, i.e., the CLI scheme converges with second-order while the MR scheme converges with third-order. The results also exhibit that the QIBB and IEBB schemes converge with second-order. The results of the convergence rate are summarized in Tab. 4.1. Here, it is worth mentioning that the simulation results using the TRT and MRT collision can be altered by changing the magic number.

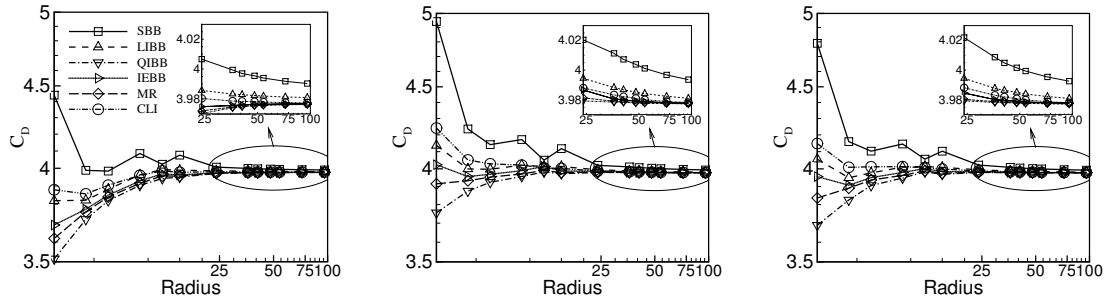

(a) SRT (b) TRT (c) MRT

Figure 4.2: Dependence of the dimensionless drag C_D on the resolution of the sphere for simple sphere pack with relative volume fraction of $\chi = 0.6$. Three collision models are presented: (a) SRT, (b) TRT, and (c) MRT. Each figure depicts 6 boundary conditions scheme results.

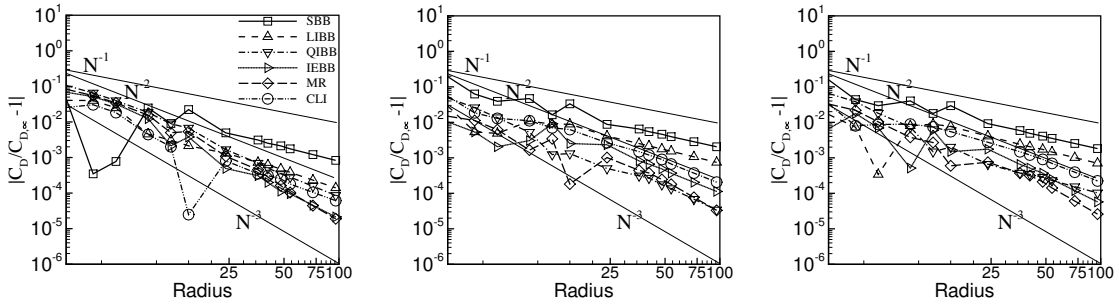

(a) SRT (b) TRT (c) MRT

Figure 4.3: Logarithmic relative error of the dimensionless drag $|C_D/C_{D,\infty} - 1|$ as a function of the sphere radius (in lattice units). Three collision models are presented, (a) SRT, (b) TRT, and (c) MRT. Each figure depicts 6 boundary conditions scheme results. The solid lines are eye showing convergence rate.

Table 4.1: Limit value of the dimensionless drag force and the convergence rate α calculated from the last three results of each boundary condition in Fig. 4.2.

		SBB	LIBB	QIBB	IEBB	MR	CLI
SRT	α	1.29	1.74	2.05	2.60	2.95	1.87
	$C_{D,\infty}$	3.98340812	3.976854186	3.97337407	3.97329727	3.97282669	3.97363293
TRT	α	1.14	1.26	2.41	2.06	2.94	2.05
	$C_{D,\infty}$	3.98180682	3.97455861	3.97369797	3.97372456	3.97373716	3.97383257
MRT	α	1.15	1.26	2.40	2.54	2.95	1.98
	$C_{D,\infty}$	3.98167626	3.97460279	3.97319284	3.97402321	3.97378283	3.97362

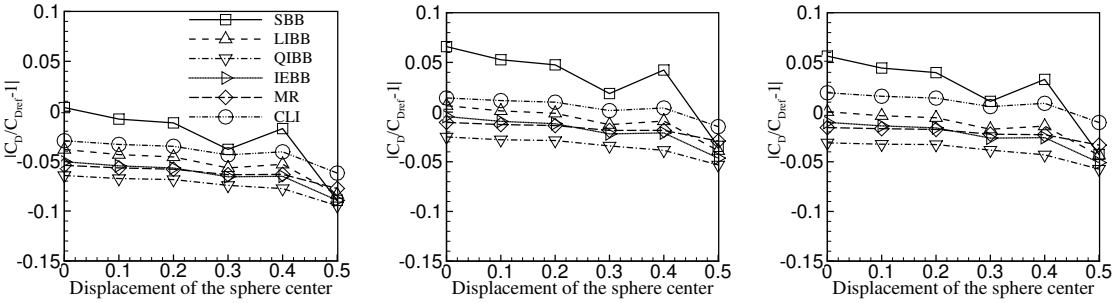

(a) SRT (b) TRT (c) MRT

Figure 4.4: Relative error of the drag force $(C_D/C_{D,\mathrm{ref}} - 1)$ as a function of the sphere center displacement (in the lattice cell). Three collision models are presented, (a) SRT, (b) TRT, (c) MRT. Each figure depicts the results of 6 boundary conditions. All simulations were conducted by $\Lambda = 3/16$, $r = 4.5$, with a solid volume fraction of $\chi = 0.6$.

4.2.2 Effect of the sphere displacement

In these experiments, we also observe pre-asymptotic discretization error modes where the errors for most models do not smoothly decrease with the resolution ($r < 15$). Comparing, for instance, the LIBB model with the QIBB model reveals that the higher order scheme is less affected by this discrepancy. To investigate the source of these fluctuations, we conduct a second series of tests where the center of the sphere is shifted stream-wise inside the cell. In all cases, the radius of the sphere is kept fixed at 4.5 lattice units and the relative volume fraction was set to $\chi = 0.6$. In Fig. 4.4, we show the results for a displacement of $0.0 - 0.5$ times a cell width. Although the results obtained by the SRT-SBB are relatively good for this setup, we observe that the SBB scheme for all considered collision schemes is more sensitive to the positioning of the center. As this behavior stems only from the geometry representation, the use of interpolation models significantly increases the reliability of the results. Since the displacement along the span-wise showed a similar behavior, we do not list these results.

4.2.3 Viscosity independence of the computed permeability

As many researchers have previously reported, the choice of boundary conditions and collision models may have a strong impact on the simulation accuracy (*Pan et al.*, 2006; *Ginzburg*, 2008; *Bogner et al.*, 2015; *Bartuschat and Rüde*, 2015). To have a complete understanding of the effects of the boundary conditions and collision schemes on the results, we conduct a viscosity dependency study for a setting where a periodic-pressure-drop boundary condition drives the flow. The viscosity dependence study is of particular importance when the simulation across a broad range of Reynolds numbers is of interest since the viscosity is one of the key parameters to achieve different Reynolds numbers in the LBM simulation. To exclude pre-asymptotic discretization error modes from our observations and only concentrate on the real inconsistencies introduced by a particular combination of collision and boundary treatment, we use a sufficient resolution of 16.5 (in lattice units) for the sphere radius. The permeability in the Darcy regime is only a geometrical characteristic; therefore, it is used to show the effect of viscosity. As proposed by *Adler* (1992), the average pressure gradient in the flow direction can be computed as $\nabla P \cdot \boldsymbol{i} = -F_D\, L^{-3}$, where L is the length of the domain in flow direction. By combining this equation with Eq. (4.1) and Eq. (2.6), we find the reference permeability K_{ref}. Here, we use the drag force provided by *Sangani and Acrivos* (1982) to calculate the reference permeability.

The plots in Fig. 4.5 display the ratio of the computed permeability to the reference permeability, K/K_{ref}, for a simple sphere pack with a relative solid volume fraction of $\chi = 0.6$. We consider viscosity in the range $[0.029, 0.45]$ (LB unit) and compare different collision models and boundary conditions. In Fig. 4.5(a) we show that for all boundary schemes, the SRT collision results in a permeability that is strongly dependent on the viscosity. While the IEBB scheme is less sensitive than the other schemes, the errors we can expect from an SRT collision model are still unacceptable for our purposes.

The results plotted in Fig. 4.5(b) and Fig. 4.5(c) depict the same set of experiments conducted with the TRT and MRT models, respectively. The result achieved by the TRT collision operator shows that the SBB, CLI, and MR schemes produce viscosity-independent permeability. The LIBB scheme results in an unacceptable viscosity-dependency of the permeability and the QIBB and IEBB also show viscosity-dependent permeability but lower than the LIBB. The results for the MRT model show the same behavior as the TRT. However, we see a little violation in the MR scheme, in which the relative difference is below 0.02%. The CLI and SBB also

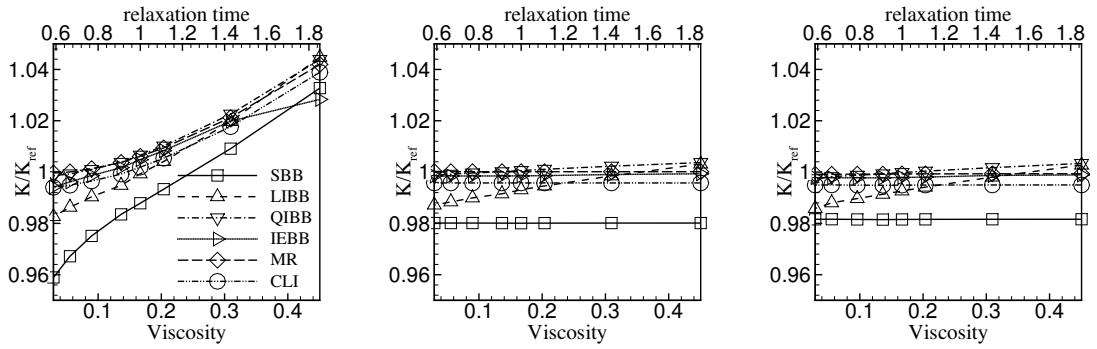

(a) SRT (b) TRT (c) MRT

Figure 4.5: Viscosity dependence of the permeability for the solid volume fraction of $\chi = 0.6$. The results represent the normalized permeability as K/K_{ref} for different boundary conditions in the viscosity range $[0.029, 0.45]$ in the LB unit corresponding to the relaxation time of the range $[0.58, 1.85]$, which covers both the over- and under-relaxed modes.

reproduce viscosity independence results. Although the SBB results in viscosity-independent results, however, it severely under-predicts the permeability due to its staircase representation of the geometry. These results are in agreement with those found in the simulation of the TRT collision in the work of *Pan et al.* (2006).

We note that, by comparing the two linear boundary schemes, namely, the CLI and LIBB, we observe that the LIBB does not yield viscosity-independent results in any of the collision models under consideration. The CLI has much better properties in this respect and gives viscosity independence results with the TRT and MRT collision models.

It is worth mentioning that the SRT collision scheme should not be used when the flow behavior is being studied across a wide range of Reynolds numbers. For instance, the correlation of the drag force or the permeability can be wrong, because the viscosity in the LBM is one of the key parameters that can be adjusted to simulate a certain Reynolds number of the flow. There are also some relaxation combinations proposed for the MRT model for high Reynolds number flow, which fixes the ghost relaxation rates to achieve stability. Those also leads to viscosity dependent results. For further details, we refer interested readers to (*Khirevich et al.*, 2015).

Table 4.2: Dimensionless drag force of steady laminar flow at $Re_p = 46$ and $\chi = 0.9$ for the SBB, CLI, and MR boundary schemes. All of the simulations are conducted with the TRT collision operator and the D_3Q_{27} lattice model.

$D/\Delta x$	SBB	CLI	MR
36	26.546	22.7539	22.3431
72	24.6073	22.6939	22.5754
144	23.6916	22.6731	22.6392
288	23.2805	22.6681	22.6535
α	1.17	1.79	1.86

Table 4.3: Dimensionless drag force of weakly turbulent flow at $Re_p \approx 315$ and $\chi = 0.9$ for the SBB, CLI, and the MR boundary schemes without correction term. All of the simulations are conducted with the TRT collision operator and the D_3Q_{27} lattice model.

$D/\Delta x$	SBB	CLI	MR
102.6	64.8742	64.8312	64.8332
144	61.6376	63.9441	63.8481
202.5	62.6216	63.3753	63.2392
288	64.0017	63.0316	63.7219
α	-	1.58	-

4.3 Pore-scale simulation at $Re > 1$

In this section, we investigate the consistency of the boundary condition schemes under steady laminar and weakly turbulent flows.

4.3.1 Convergence rate

To examine the convergence rate, we use the low Reynolds results from the previous sections to choose a first-, second- and third-order boundary scheme, namely the SBB, CLI, and MR, respectively. For all of the evaluation in this section, we use the TRT collision operator with the D_3Q_{27} velocity set and fix the magic number to $3/16$.

For the steady laminar flow, we simulate the fluid flow through the simple sphere pack at $Re_p = 46$. In this regime, the inertia of the fluid flow plays an important role, and the flow is non-linear. The results of the dimensionless drag are presented in Tab. 4.2 for different boundary conditions. The SBB and CLI boundary schemes converge with first- and second-order, respectively, as in the Stokes regime, while the convergence rate of the MR drops to second-order. This reduction is because of the second-order accuracy of the LBM in bulk fluids in the non-linear regime. The results also show that the SBB boundary scheme with the highest resolution conducted here differs from the CLI and MR schemes by 2.7%.

Here we investigate the capability of the LBM in the unsteady weakly turbulent flow at $Re_p \approx 315$. We conduct the simulation for a sufficiently long time such that the relative difference of the time-averaged drag force is below 0.1%. The results of the dimensionless drag force for various boundary schemes are shown in Tab. 4.3. Since the flow in this Reynolds number is fluctuating, we averaged the dimensionless drag force for 50 L/U_D for each case. We use the diffusive scaling to keep the compressibility error on the same scale as the discretization error. Increasing the resolution beyond the necessary one for a stable simulation, the drag force computed in different boundary conditions does not change significantly. The MR boundary scheme in this test makes instability, and we found out that the correction term causes this problem. Since the MR model without correction term is a second order boundary, we will present the result of the MR model without the correction term in this section. The computed convergence rate of the CLI based on the three point values is 1.58, while the asymptotic convergence rate for other boundary schemes cannot be calculated.

The results suggest that for the simulation of turbulent flow in porous media, where high enough resolution is needed to capture the small vortices effects and stable simulation, increasing the resolution does not significantly change the computed drag force. However, boundary layer effects at high Reynolds numbers should be investigated carefully for different boundary schemes to have a general conclusion. In the above tests, the SBB results differ by at most 2% from the CLI and MR results.

4.4 Computational cost

Our results obtained in Sec. 4.2.1 and Sec. 4.2.3 indicate that the TRT and MRT collision operators in combination with the MR boundary scheme results in the most accurate solutions. Given that the highly optimized split kernel of the TRT implementation in waLBerla is about as fast as the SRT model (*Godenschwager et al.*, 2013), there is no justification to use the MRT scheme, as in the optimized version the computation is about a factor of two more expensive. Although control of the higher order moments in high Reynolds numbers is only possible with the MRT collision scheme, the TRT collision model can also be used as it can control anti-symmetric moments.

While the identification of a favorable collision operator is clearly apparent, the choice of the right boundary treatment is less obvious. Note that, especially for a

direct numerical simulation of turbulent flow, where one has to provide enough resolution to resolve the smallest dissipative scales, massive parallelism cannot be avoided. Unfortunately, the more accurate boundary handling methods must access LBM nodes from up to three cells away from the particle boundary cell, see Sec. 3.9. In a massively parallel setting, such physical boundary points may be near a logical processor boundary that has been created by the domain partitioning for a distributed memory machine (*Feichtinger et al.*, 2011). In WALBERLA this situation is handled by extra ghost-layer exchanges, i.e., by communicating an extended set of distribution functions to neighboring processors along the sub-domain boundaries. The data dependencies also cause additional synchronization overhead in the parallel execution. Although by saving both the pre- and post-collision PDF, the necessary nodes for the interpolating boundaries can be reduced by one, however, this results in an additional communication for the saved field, which in general does not help the efficiency of the code.

For our computational objectives, more complex geometric configurations must be considered. In these cases, the communication of data quickly becomes the critical bottleneck. For our application, it is of particular importance to save on communication, as for production runs many time steps are necessary to find the desired solution. Thus, to keep the computing times acceptable, only moderately large blocks of LBM nodes can be assigned to each processor. Consequently, the ratio between computation and communication is already a bottleneck despite the highly optimized WALBERLA program and even when just one layer of ghost nodes is exchanged in every time step. This means that our typical simulation runs are already close to the strong scaling limit of the parallel execution, as analyzed in *Godenschwager et al.* (2013).

To demonstrate the parallel scalability and efficiency of the WALBERLA framework in the context of a porous media simulation, we perform a weak-scaling study. Here we use a lattice of 151^3 cells per core and embed into this grid a sphere with a diameter of 90 lattice length. The results have been obtained on the LIMA cluster at RRZE [2] which has 500 compute nodes. Each node consists of two Intel Xeon 5650 "Westmere" chips so that each node has 12 cores running at 2.66 GHz. We conduct scalability tests ranging from one node to 64 nodes. This setup results in 2.64×10^9 cells for the largest run including 768 spherical obstacles. Fig. 4.6(a) displays the weak-scaling results using the TRT kernel. Fig. 4.6(a) shows the mega lattice updates per second (MLUPS) for the SBB and CLI boundary schemes. The

[2] https://www.rrze.fau.de/dienste/arbeiten-rechnen/hpc/systeme

results do not only confirm that the code scales very well, but also that the MLUPS count per core compares favorably with other state of the art LBM implementations *Peters et al.* (2010); *Schönherr et al.* (2011); *Robertsen et al.* (2015).

We point out that achieving a good scaling behavior becomes more challenging when the node performance is already high, but a high performance on each node is a fundamental prerequisite for achieving good overall performance. Thanks to both, the meticulously optimized waLBerla kernels on each node, combined with the carefully designed communication routines, the MLUPS value per core is high and stays nearly constant while the number of cores is increased. Note that the CLI boundary conditions cause a slowdown of about 10% in comparison to the SBB boundary condition, which is the fastest scheme. Fig. 4.6(b) displays the percentage of the total time spent for the MPI communication, the portion of the total time which is dedicated to the streaming and the collision step, and the time for the boundary handling. The slowdown of the performance while using the CLI is due to the additional time that is needed for the communication and the higher complexity of the boundary condition compared to SBB. Although, the boundary handling of the CLI scheme also takes a little bit more time than the SBB, the higher accuracy of the CLI compared to the SBB allows in complex application to use a coarser resolution of the simulation domain.

As a good compromise between the cost (including communication on parallel computers) and numerical accuracy, we choose here the TRT-CLI scheme for large pore-scale problems. It leads to a reasonably good accuracy, has no viscosity-dependence, and needs less communication than the MR scheme. Hence, using the slightly less accurate but significantly better parallelizable method results in a considerable reduction in run-time.

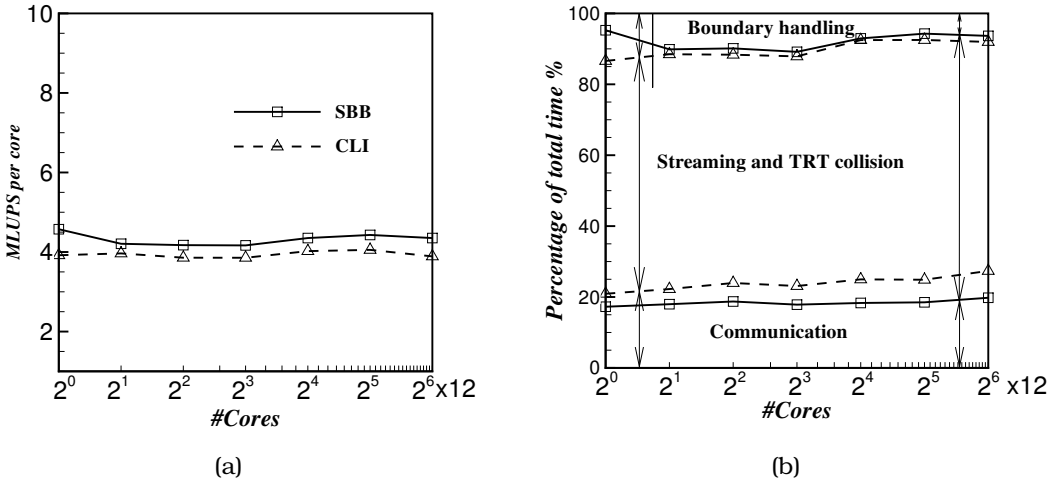

(a) (b)

Figure 4.6: Weak scaling on LIMA-Cluster using 151^3 cells per core, a) Measured MLUPS per core, b) percentage of total time spent for MPI communication, streaming step and the TRT kernel computation, and the boundary handling step.

4.5 Lattice model effect

For a three-dimensional LBM simulation, stencils that differ on the velocity directions can be used. Lattice models require an accurate evaluation of their velocity moments up to second-order to consistently recover Navier-Stokes dynamics in the continuum limit. However, they may behave differently at a discrete level, which in turn can lead to the violation of some necessary physical requirements. Investigating an intermediate Reynolds number flow ($50 < Re < 500$) through a nozzle, *White and Chong* (2011) demonstrated that the D_3Q_{19} lattice model, a three-dimensional model with a 19 directional stencil can cause a lack of isotropy in the flow field. This deficiency, which was found to be independent of the collision model, the grid resolution, and the Mach number, can be removed by using the D_3Q_{27} lattice model which has a 27-directional stencil. They found out that lattice models with a plane having less than six velocity vectors are not entirely isotropic and can produce qualitatively different results. Similar observations have been reported by other researchers (*Mayer and Házi*, 2006; *Geller et al.*, 2013; *Kang and Hassan*, 2013). Recently, *Silva and Semiao* (2014) theoretically analyzed the truncation errors of different lattice models and showed that reduced lattice schemes, i.e., D_3Q_{15} and D_3Q_{19}, produce spurious angular velocities. They revealed that, for convection-dominated flows the rotational invariance will be violated if a reduced lattice scheme is used. *Nash et al.* (2014), on the other hand, investigated the Dean flow at $Re \approx 400$

with a strong secondary flow and demonstrated that none of the respective lattice models produces significant artifacts in the velocity field. Their results suggest that using a greater number of velocity sets for a lattice model provides better results for interpolating boundary schemes but worse results when using the simple bounce-back boundary.

In this section, we evaluate the effect of the lattice models on turbulent flow and compare the results of the simulations conducted with two different lattice models of the D_3Q_{19} and D_3Q_{27}. The flow dynamics are obtained for touching spheres arranged in a simple cubic array. The magic number for the simulation is fixed at $3/16$, and the TRT collision operator in combination with the CLI boundary scheme is used.

To simulate the touching sphere array ($\chi = 1.0$), the flow field is initialized with the result of the simulation using the SBB scheme and is continued with the CLI boundary scheme. This method of initialization helps to avoid the instability arising from the narrow gaps of the pores. For the boundary nodes for which the neighbor fluid cell does not exist, the SBB scheme is used instead of the CLI. By handling the boundary in this way, the convergence rate will decrease but still offer more stability, especially for unsteady flow. To calculate the time average Darcy velocity in the turbulent flow, we average the volume averaged velocity for 100–150 L/U_D flow through times.

As it is pointed out in (*Tenneti et al.*, 2011), to resolve the boundary layer, the grid resolution in the DNS approaches should increase appropriately by increasing the Reynolds number. The boundary layer thickness can be approximated as $\delta_b \sim D/\sqrt{Re_p}$. To check the grid-independence of the results in the turbulent flow, we conducted the simulation at $Re_p = 1045$ with different resolution. The results are presented in Tab. 4.4 which depict that for $\delta_b > 5.5$, the time-averaged dimensionless drag force (C_d) is not changing significantly. For the following simulation, we use 252 lattice cells as sphere diameter.

Figure 4.7 shows the instantaneous velocity field of the highest Reynolds number considered in this study which is 2477. The time evolution of the dimensionless drag force is also presented in this figure which shows chaotic behavior of the flow. Analysis of the time-averaged results indicates that the same pressure drop will lead to different Darcy velocities for various lattice models. For D_3Q_{27}, the average velocity is 2.8% less than the D_3Q_{19} model and leads to the Reynolds number $Re_p = 2477$, while for the D_3Q_{19} model $Re_p = 2547$. On the other hand, the drag force calculated by these two models differs by only 0.2%. The relative difference of the dimensionless drag coefficient, is 2.98%.

Table 4.4: Dimensionless drag force of turbulent flow at $Re_p \approx 1045$ and $\chi = 1.0$, and also the approximate boundary layer thickness δ_b in lattice unit. The simulations are conducted with the TRT collision operator, the CLI boundary scheme and the D_3Q_{19} lattice model.

$D/\Delta x$	Re_p	C_d	δ_b
150	1045	356.1	4.63
180	1043	355.2	5.57
252	1045	350.2	7.79
360	1048	348.9	11.12

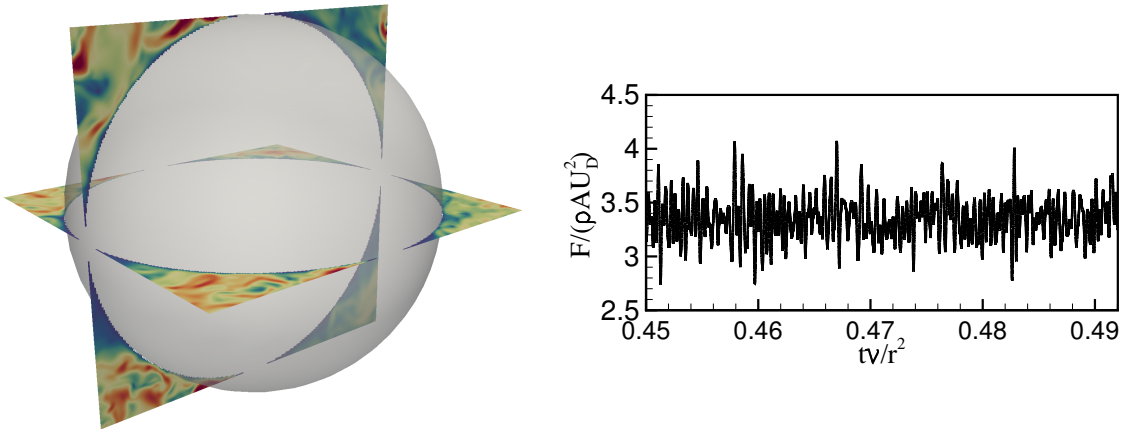

(a) (b)

Figure 4.7: Instantaneous velocity field contour of turbulent flow of touching spheres in simple sphere array at $Re_p = 2477$ simulated with D_3Q_{27} (left), time series of the drag force simulated with different Re_p (right).

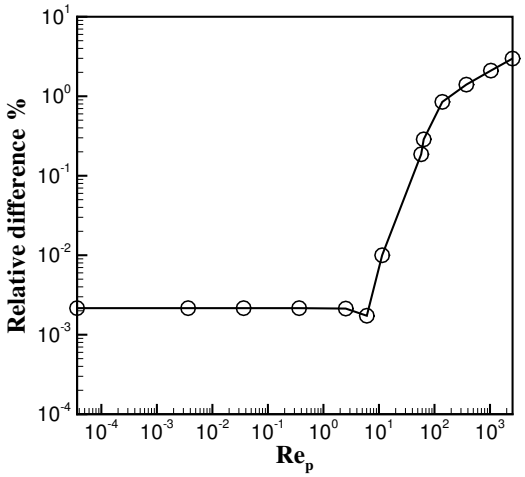

Figure 4.8: Relative difference of the dimensionless drag force $|C_{D,reduced}/C_{D,full} - 1|\%$ of the two lattice models, D_3Q_{19} and D_3Q_{27}, reduced stencil and full stencil, respectively.

Figure 4.8 shows the relative differences between the D_3Q_{19} and D_3Q_{27} models for different Reynolds numbers of the flow. Here we can see that for Reynolds numbers below 100, the violation of the rotational invariance by the D_3Q_{19} model does not significantly affect the dimensionless drag force and for the flow beyond that Reynolds number, rotational invariance starts to exert an effect on the physical behavior of the flow.

4.6 Cumulant collision operator

In this section, we briefly evaluate the cumulant collision operator that is described in Sec. 3.4.1. Utilizing the cumulant collision is proposed to remove the Galilean invariance violation from the LBM. Cumulant can remove this problem, since the higher order cumulants do not depend on the lower order cumulants. This also helps to remove the hyper-viscosity in the fourth order moment in the other collision models. However, there are few articles available and the cumulant collision is not evaluated yet. One of the key question in the collision operator is the way of choosing the relaxation rate. *Geier et al.* (2015) mentioned that in the three dimensional simulation, D_3Q_{27}, ω_1 is related to the shear viscosity. It is mentioned that ω_1 has a leading order influence on the results, and the rest can be chosen in the range of $(0, 2)$. Here we test that by the benchmark we have used in Sec. 4.2.3. We call this type of relaxation set as *type I*, and the results of the permeability for a wide range of viscosity is presented in Fig. 4.9.

As the results show, the permeability strongly depends on the viscosity that is not physical. Here, we propose to choose the relaxation the same as the MRT, i.e., all of the even order cumulants should be adjusted regarding to the ω_1, as it is described in Sec. 3.5. Another possibility is to choose the relaxation rates such that the even order cumulants are set to ω_1, and the odd order cumulants is calculated the same way as for the TRT. We call the latter one as *type II*. The results demonstrate that this set of relaxation rates leads to a viscosity-independent permeability.

In the laminar regime, the difference between the TRT and cumulant is in the order of machine error. The main difference between these two methods is the truncation errors of the equilibrium that exist for the TRT collision, but not for the cumulant collision. At very high Reynolds number, where the hyper-viscosity is important, the results show significant difference, both in accuracy and stability. However, detailed

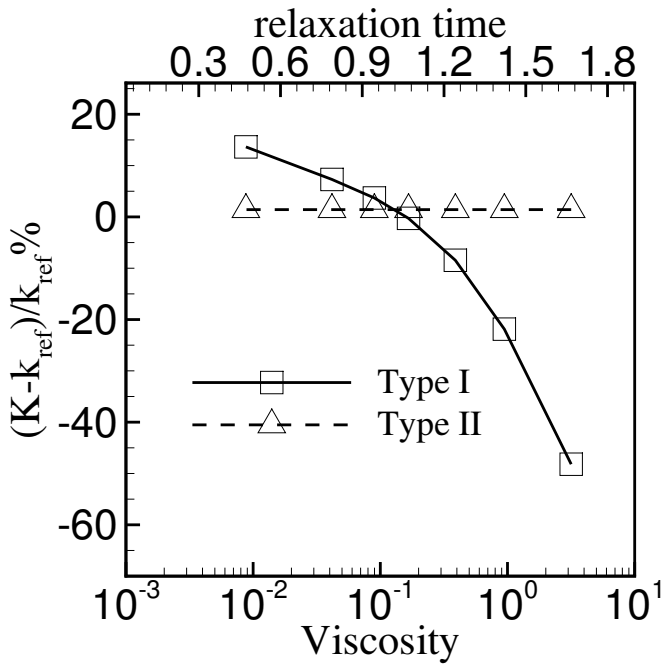

Figure 4.9: Viscosity dependence of the permeability of the simulation performed by the cumulant collision operator.

analysis of this topic is out of scope of this work and we will postpone it for future works.

4.7 Summary

The evaluation presented in this chapter revealed that the simulation with the LBM using the TRT collision operator and the CLI no-slip boundary condition can be considered as a good compromise between accuracy and efficiency. Using the results of this chapter, in the following chapter we analyze the flow characteristics at different flow regimes.

5 Flow through structured array of particles

5.1 Introduction

Defining the flow regimes, as well as the transition between those regimes is essential for the design and optimization of practical devices that include porous media. *Seguin et al.* (1998b) studied the transition from laminar flow to turbulent flow and found that the transition occurred at different Reynolds numbers at different locations in porous media. *Zeng and Grigg* (2006) proposed a revised Forchheimer number as $Fo = \frac{K\beta\rho v_s}{\nu}$, along with the Reynolds number as a criteria to identify the beginning of non-Darcy flow (cf. Sec. 2.3.2). They defined a critical Forchheimer number as $Fo_c = 0.11$. Further studies attempted to define the transition between different flow regimes. However, the characteristic length, that is used to define the Reynolds number and the friction factor is not unique, and this makes direct comparisons difficult (*Zeng and Grigg*, 2006; *Moutsopoulos*, 2007; *Moutsopoulos et al.*, 2009; *Sedghi-Asl and Rahimi*, 2011; *Bagci et al.*, 2014).

Despite the common usage of the Forchheimer euation, a recent experimental study by *Bagci et al.* (2014) revealed that the β factor that is measured in the laminar regime is not valid across the entire range of the fluid flow. The study proposed the usage of two different values for permeability, in conjunction with distinct values β for laminar and turbulent flow through spherical particles. Specifically, the flow becomes turbulent in the range $Re_p > 300$ and significant deviations were observed from the Forchheimer model with the laminar β.

Based on a series of experiments, *Barree and Conway* (2004) proposed another model with the same structure as the Darcy model Eq. (2.6) albeit replacing absolute permeability K_D by an apparent permeability (denotes as K_{app}). The apparent permeability can be measured in the same way as the Darcy permeability, but it depends on the flow in a non-linear fashion and is defined as follows:

$$K_{app} = K_{min} + \frac{(K_D - K_{min})}{(1 + {Re_T}^F)^E}. \tag{5.1}$$

Here, E and F are exponential coefficients that describe the heterogeneity of the porous medium. Specifically, $Re_T = \rho l_T U/\mu$ denotes the Reynolds number based on a transition length scale corresponding to l_T, and K_{min} is a minimum permeability attained at high Reynolds numbers. This model was proposed based on the conjecture of two plateau areas for permeability at low and high Reynolds numbers. The plateau areas at low Reynolds number correspond to the Darcy regime, and the prediction of the Barree–Conway model in the transition region indicates good agreement with those of experiments (*Barree and Conway*, 2004; *Lopez-Hernandez*, 2007; *Lai et al.*, 2012). However, the plateau at higher Reynolds numbers is largely hypothesized. This model will be examined in Sec. 5.4.

The evaluation conducted in chapter 4 confirmed that the LBM can simulate fluid flow in porous media in a wide range of Reynolds numbers. In this section we present the flow pattern of the simulation of simple sphere pack with two different solid volume fractions. The flow field is initialized with the results achieved by using the SBB boundary condition for the sphere and is continued with the CLI boundary scheme. This initialization avoid the instability coming from the narrow gaps in the pore. The Magic number for the simulation is fixed at $3/16$ and the TRT collision operator is used.

5.2 Flow through the sphere pack with $\chi = 0.6$

To show the flow behavior in detail, Fig. 5.1 presents the streamlines that are plotted in two perpendicular planes based on an instantaneous velocity field at a dimensionless time $t^* = t\nu/D^2 = 2.22$. The plots are presented in span-wise views, i.e., XY and XZ, as well as 3D streamlines. Figure 5.1(a) presents a side view of the streamlines of the simulation in $Re_p < 1$. We can observe the development of steady boundary layers near the solid boundaries and symmetric streamlines at the upstream and downstream of the sphere. This behavior can be observed from the other views as well. Figure 5.1(c) shows a 3D view of the streamlines, in which the color is re-scaled based on the corresponding maximum velocity. The flow is in the Stokes regime that is linear and symmetric.

As the Reynolds number increases, we can see the onset of inertial effects caused by the acceleration and deceleration of the fluid passing through the space between the periodic spheres. In Fig. 5.1(d), we see that small vortices start to form in front of the sphere and some larger ones behind the sphere. Therefore, a large momentum

deficit in the wakes of the spheres is happening. Since the distance to the next particle is not large enough, the drag force deviates from the drag force of a sphere in unbounded fluid. In this regime, the form drag is added to the viscous drag and increases the head loss.

A further increase in the flow rate leads to the merging of the two vortices to an even larger vortex that occupies the space between the two spheres as shown in Fig. 5.1(g). Larger recirculation area results in a lower flow capacity. Because of the symmetric flow field, the pressure difference between the upstream and downstream of the sphere decreases, and this in turn decreases the inertial contribution to the drag force when compared to the viscous contribution. Consequently, the drag force increases relatively slowly with the Reynolds number. Although inertial flow is dominant at $Re_p = 79$, the flow regime is still laminar and steady.

From Fig. 5.1, it can be concluded that increasing the Reynolds number generally decreases the flow capacity.

The acceleration/deceleration effects described above are the dominant phenomenon until the flow begins to fluctuate. As shown in Fig. 5.2(a), the flow is still laminar at approximately $Re_p = 180$, but the symmetry breaks and the flow becomes unsteady. The flow separation and the boundary layer interaction downstream of the sphere are observed that cause energy dissipation in the unsteady laminar flow regime.

The onset of fluctuations is reported between $Re_p = 110$ and $Re_p = 250$ for different porous media (*Lopez-Hernandez*, 2007). The critical Reynolds number strongly depends on the porosity, arrangement of the packing and sizes of the spheres. The change of the flow direction in the flow regime along with the asymmetry of the flow about the sphere increases the pressure difference between the upstream and downstream of the sphere. Therefore, the inertial contribution to the drag force increases by increasing the Reynolds number.

At higher Reynolds number, we observe the onset of turbulent chaotic behavior; cf. Fig. 5.2(b) and Fig. 5.2(c). Candidate mechanisms for governing transition to turbulent flow in porous media, are the mixing of flow, and separation of microscopic flow field from the internal local geometry. We can also observe small vortices that can pass through the pores and thereby increase the inertial effects. At even higher Reynolds number, flow becomes turbulent as the chaotic behavior is shown in Fig. 5.2(e) and Fig. 5.2(f).

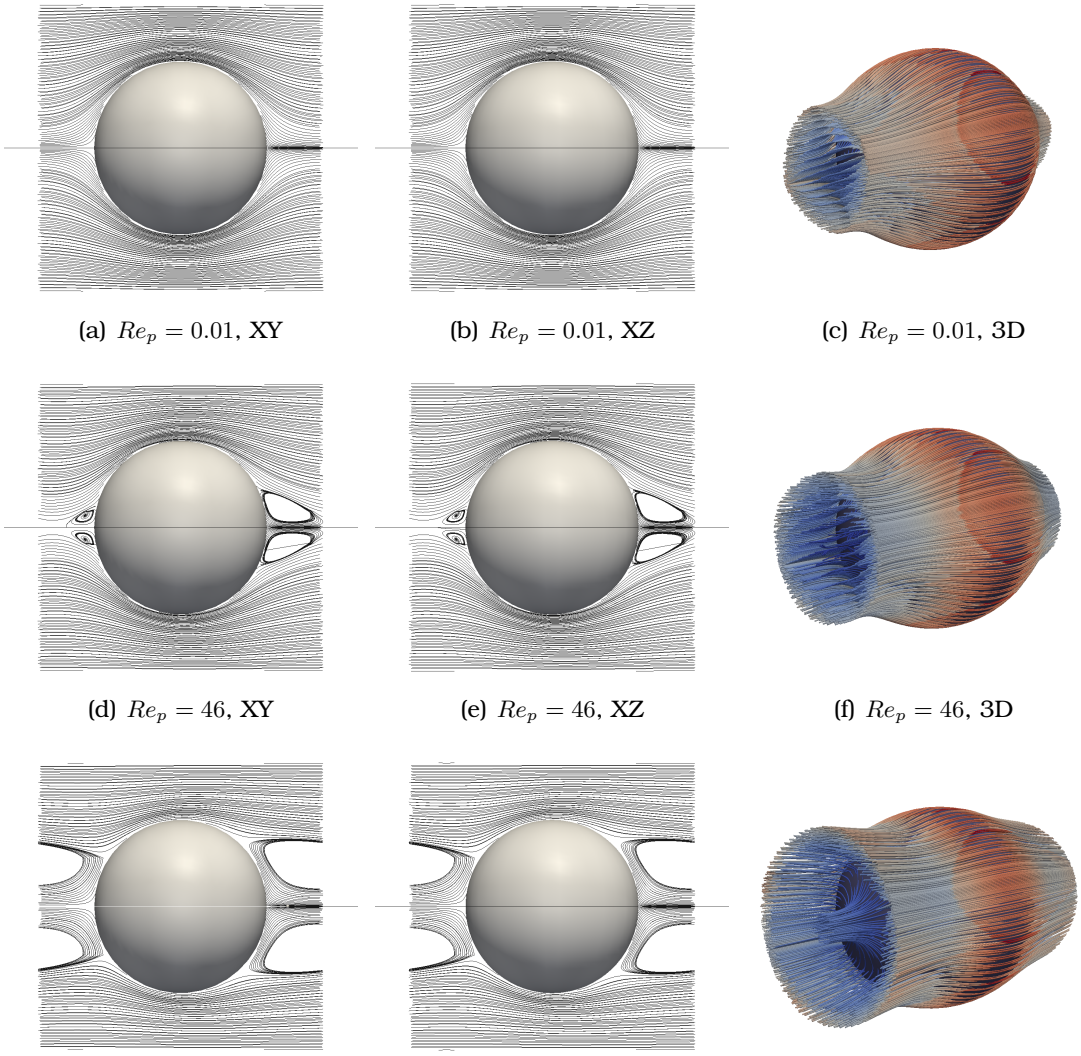

(a) $Re_p = 0.01$, XY (b) $Re_p = 0.01$, XZ (c) $Re_p = 0.01$, 3D

(d) $Re_p = 46$, XY (e) $Re_p = 46$, XZ (f) $Re_p = 46$, 3D

(g) $Re_p = 79$, XY (h) $Re_p = 79$, XZ (i) $Re_p = 79$, 3D

Figure 5.1: Streamlines of flow through the simple sphere pack at linear and non-linear steady regimes with $\chi = 0.6$ at $Re_p = 0.01,\ 46,\ 79$.

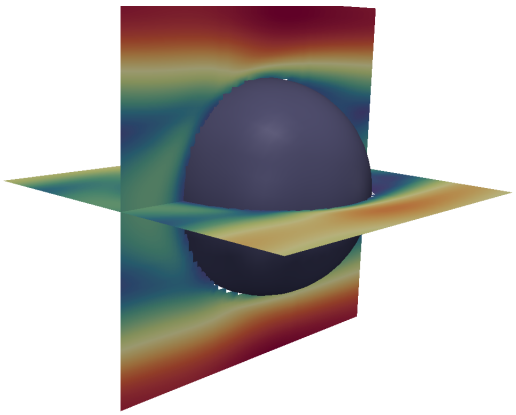

(a) $Re_p = 183$

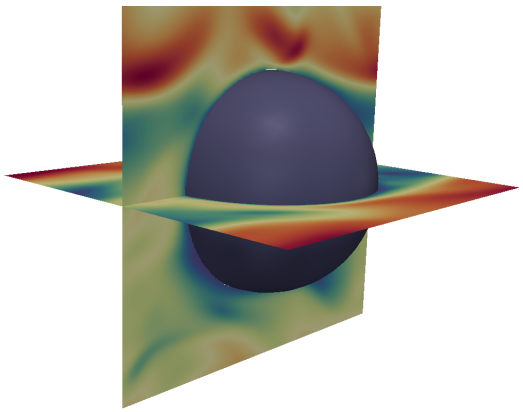

(b) $Re_p = 509$

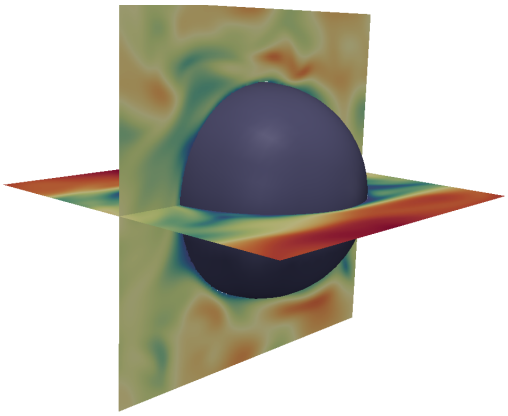

(c) $Re_p = 762$

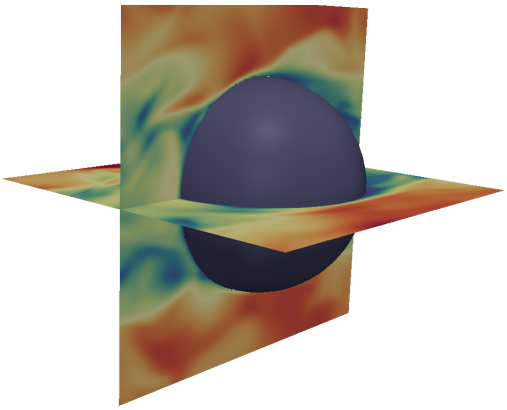

(d) $Re_p = 1008$

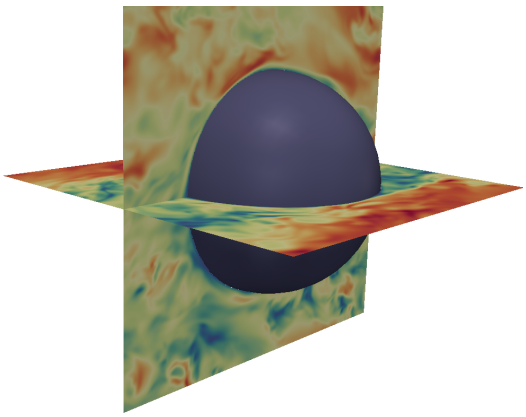

(e) $Re_p = 3880$

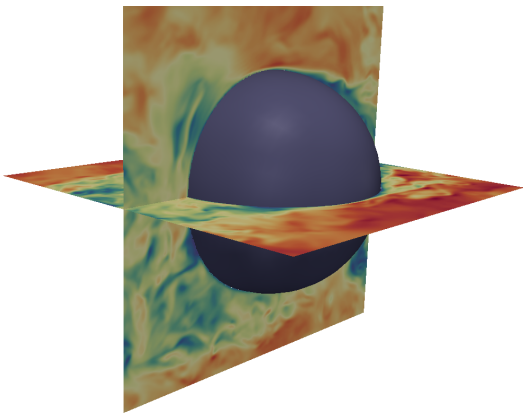

(f) $Re_p = 5812$

Figure 5.2: Velocity field of flow through the simple sphere pack for non-linear flow at $\chi = 0.6$ with $Re_p = 183,\ 509,\ 762,\ 1008,\ 3880,\ 5812,$.

5.3 Flow through the sphere pack with $\chi = 1$

In this section we investigate the flow dynamics of the touching spheres $\chi = 1$, that are arranged in a simple cubic array. The size of the domain is the same as that in the case of $\chi = 0.6$, in such a way that the resolution of the sphere in the touching sphere will be higher than in case studied with $\chi = 0.6$.

Distinguishing of flow behavior at laminar regime of the touching sphere is difficult to be shown by velocity contours. Therefore, the streamlines are presented in Fig. 5.3 to show the different flow field in creeping flow regimes and laminar regime. In the creeping flow, Figs. 5.3(a) and 5.3(b), streamlines follow the particle geometry, while in laminar regime streamlines are curvy and recirculation zone are observed as it is shown in Figs. 5.3(c) and 5.3(d). Figure 5.4 shows the instantaneous velocity field for $Re_p > 139$. The flow with $Re_p = 139$ is laminar while the symmetry of the velocity field in the stream-wise component just has been broken. At the larger solid volume fraction, the velocity field depicts that the inertial contribution to the drag force decreases. This is because of the smaller void space of the more complex flow that exists at the larger solid volume fraction. Increasing the contribution of the viscous force to the drag force results in a slow change in the total drag force as the Reynolds number increases.

By further increasing the Reynolds number, the stream-wise and span-wise velocity components start to fluctuate (Fig. 5.4(b)) and the flow regime changes to periodic-unsteady flow at $Re_p = 225$. A difference in the velocity field can be observed between the upstream and downstream areas, and this causes a strong inertial effect. Compared to the results of the sphere packing with $\chi = 0.6$, the velocity field in the dense sphere pack gives fewer information since the pore is relatively small. Therefore, the time series of the drag force coefficient is also presented to depict the flow details in a better manner. The behavior in the periodic regime can be determined from Fig. 5.5(b).

With the onset of the unsteady flow, the velocity field exhibits more fluctuations as it is observed in Fig. 5.5(c). The span-wise components of the velocity share the chaotic momentum transport, that leads to a pseudo-periodic regime as it is shown in Fig. 5.5(b).

The primary instability is followed by a secondary instability at $Re_p = 582$ (Fig. 5.5(d)) and the chaotic behavior can be observed from the velocity field. More perturbations can be observed when the Reynolds number increases and the flow becomes

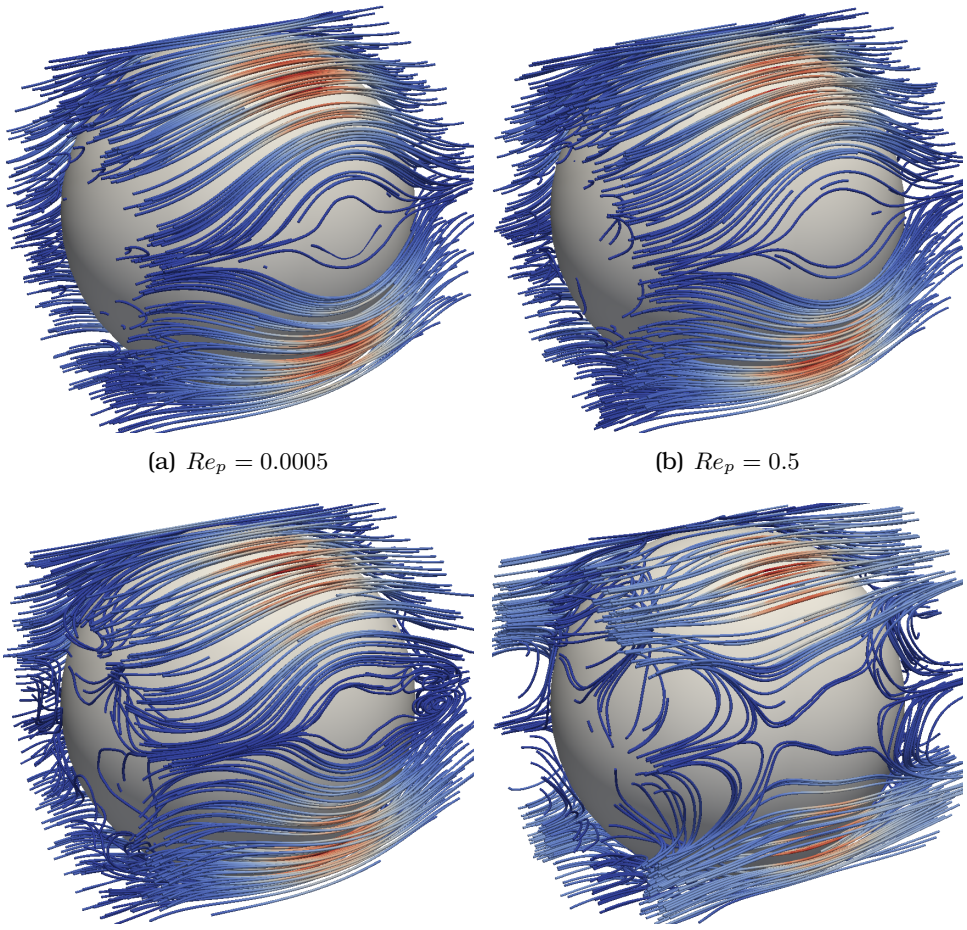

(a) $Re_p = 0.0005$ (b) $Re_p = 0.5$

(c) $Re_p = 5$ (d) $Re_p = 50$

Figure 5.3: Streamlines of flow through the touching simple sphere pack at linear and non-linear steady regimes with $\chi = 1$ at $Re_p = 0.00005$, 0.5, 5, and 50.

turbulent at approximately $Re_p = 1006$. At $Re_p = 2477$, the flow behaves randomly and small vortices can be seen in stream-wise and span-wise planes. The drag force exhibits a highly fluctuating behavior as it is displayed in Fig. 5.5(f).

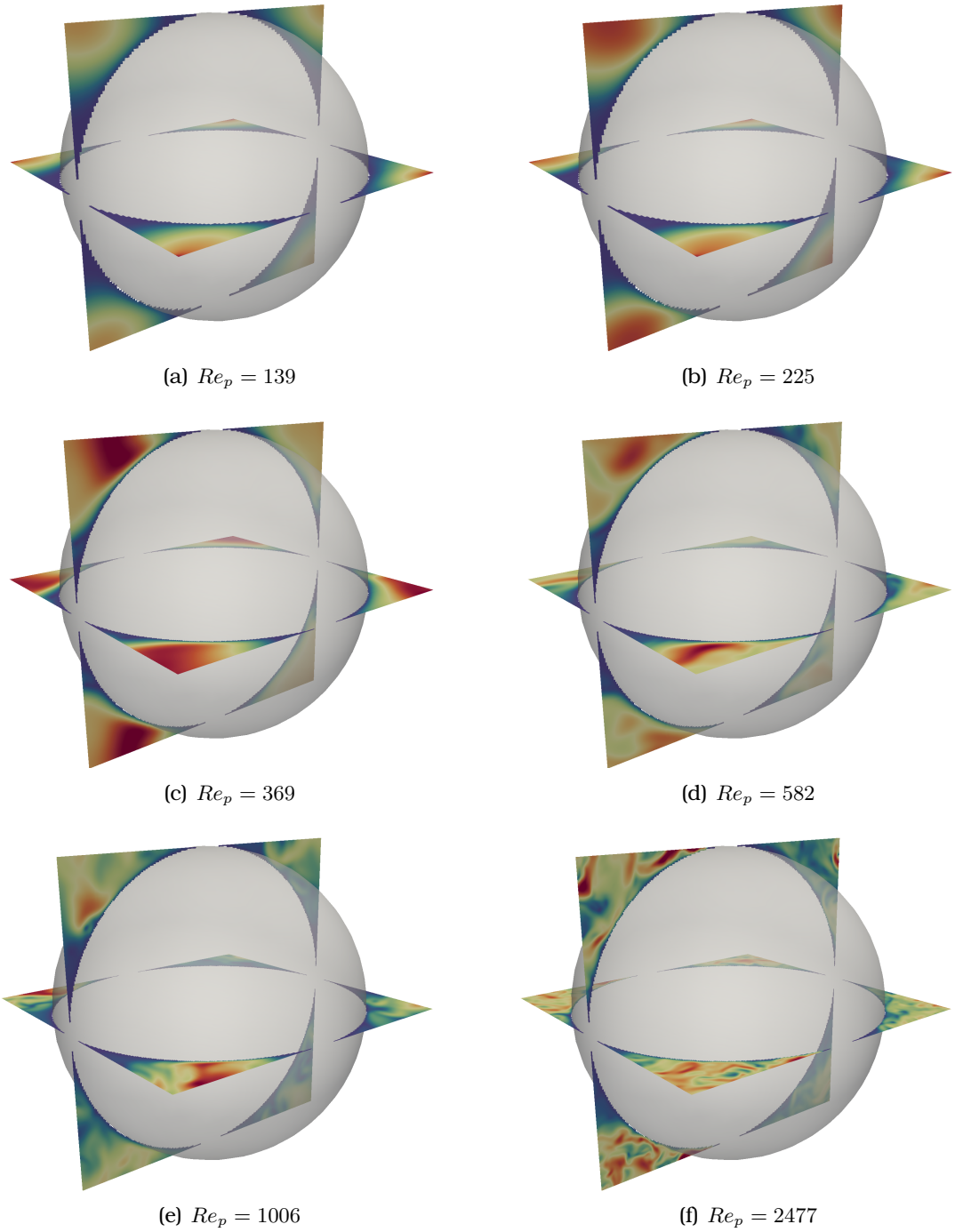

(a) $Re_p = 139$ (b) $Re_p = 225$

(c) $Re_p = 369$ (d) $Re_p = 582$

(e) $Re_p = 1006$ (f) $Re_p = 2477$

Figure 5.4: Velocity contour of the simulation with D_3Q_{27} lattice model of the touching spheres at different Re_p.

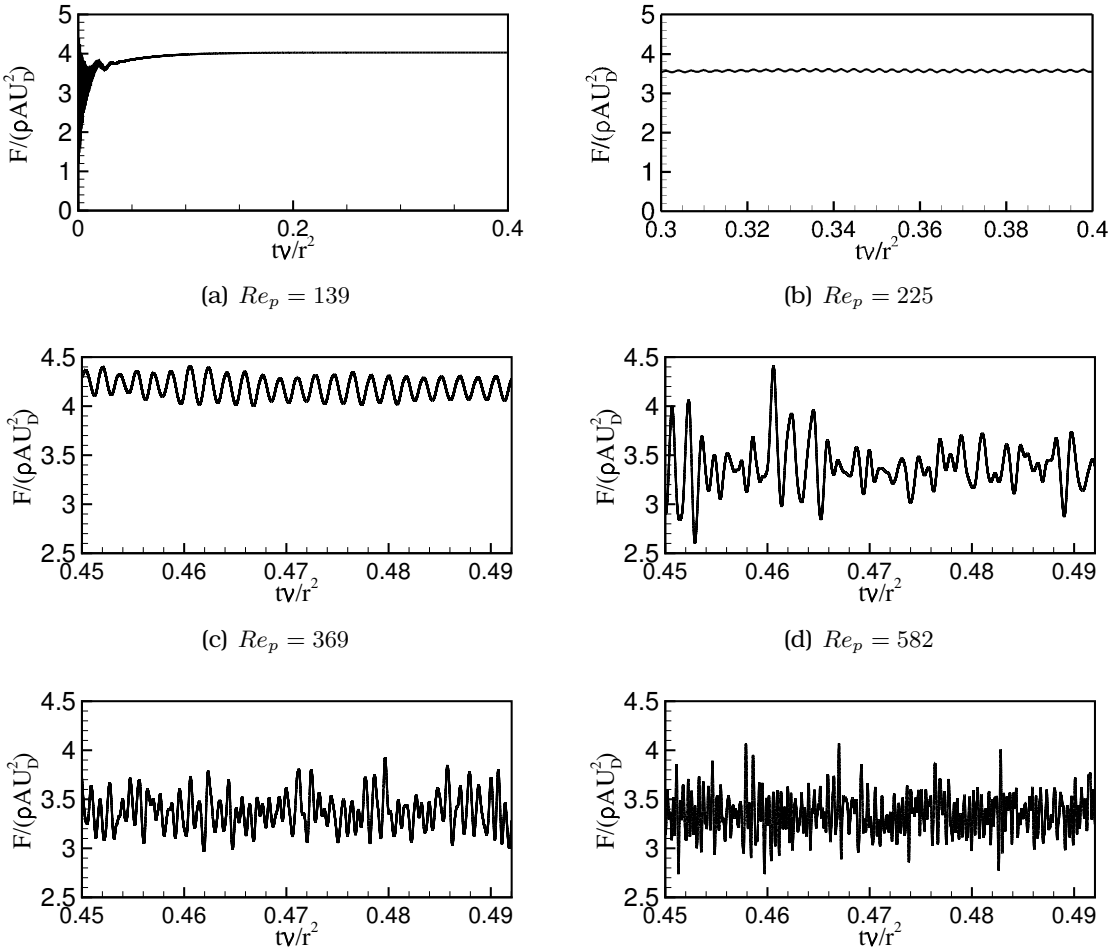

(a) $Re_p = 139$ (b) $Re_p = 225$

(c) $Re_p = 369$ (d) $Re_p = 582$

(e) $Re_p = 1006$ (f) $Re_p = 2477$

Figure 5.5: Time series of the drag force simulated at different Re_p.

5.4 Result analysis and discussion

Based on the fore-mentioned results of the pore scale simulation, we compute the Forchheimer constant C_F, the apparent permeability, and the friction factor and discuss them in this section.

5.4.1 Forchheimer constant

Forchheimer equation, Eq. (2.7), can be also written as

$$\nabla P = -\mu K_{Da}^{-1}\mathbf{U} - C_F K_{Da}^{-1/2}\rho|\mathbf{U}|\mathbf{U}, \tag{5.2}$$

where C_F is the constant inertial factor, and subscript Da denotes the Darcy regime. The Forchheimer constant is calculated based on the simulation data for two different solid volume fractions, and the results are presented in Fig. 5.6. The Forchheimer constant is believed to be fixed for a given type of porous media (*Dukhan and Patel*, 2011; *Hwang et al.*, 2002). However, Fig. 5.6 depicts that the value of C_F strongly depends on the Reynolds number, which is in line with the experimental results obtained by *Bagci et al.* (2014). They showed that the β factors have to be chosen differently for different flow regimes.

The results of the sphere pack with $\chi = 0.6$ in Fig. 5.6(a) show that two approximately constant values can be considered for laminar and turbulent flow. In our setup, these are 0.0078 for $8 < Re < 79$ and 0.023 for $762 < Re < 5812$, respectively; the former corresponds to the non-linear laminar regime, and the latter corresponds to the turbulent regime. The results of the dense sphere pack, i.e. $\chi = 1$, in Fig. 5.6(b) depict that with a good approximation, a constant value can also be considered for high Reynolds number flow. In our setup this is 0.145 for $369 < Re_p < 2477$. The results show that C_F is decreasing when Re_p increases in the steady laminar regime, and in the transition of the steady to unsteady flow, it increases when Re_p increases.

Given that the Forchheimer equation, Eq. (5.2), does not consider the porosity of the porous media, two main points can be noted with respect to the results of the Forchheimer constant of the two considered sphere packs. Although both sphere packs show the plateau at high Reynolds number, the Forchheimer constant in the laminar regime shows a distinct behavior. First, the results of the dilute sphere pack at laminar regime exhibits a lower value relative to the turbulent regime. This plateau area does not exist for the dense sphere pack at laminar regime. The second

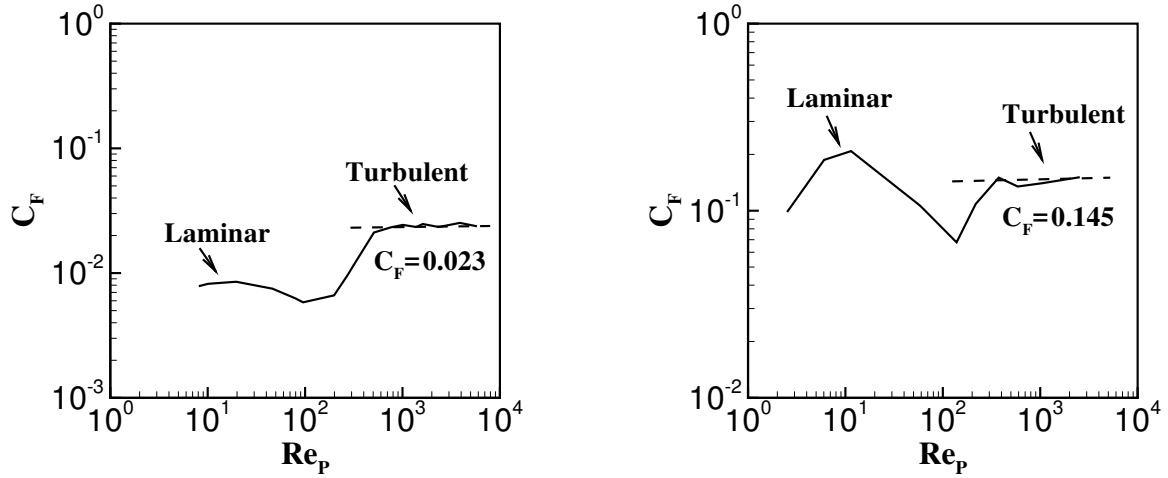

Figure 5.6: Forchheimer constant (C_F) for pressure-driven flow at different Reynolds numbers through the simple sphere pack, a) sphere pack with $\chi=0.6$, b) sphere pack with $\chi=1$.

point that is noted here is that the Forchheimer constant shows an increase when the transition from the laminar regime to the turbulent regime occurs.

5.4.2 Barree-Conway model

Apparent permeability as defined by the Barree–Conway model (5.1), can be normalized by the Darcy permeability, i.e.,

$$K^* := \frac{K_{\text{app}}}{K_{Da}}, \tag{5.3}$$

where K_{app} is determined using the one-dimensional equivalent of Darcy's law, cf. Eq. (2.6), by means of a spatially and temporally averaged velocity. To calculate the time average Darcy velocity, we average the volume averaged velocity for a period of 100–150 flow through times L/U_{Da}.

The results of the normalized permeability of the considered sphere packs are presented in Fig. 5.7 for the entire range of Reynolds numbers considered in this study. In this figure, we compare our results to a best fit with respect to the Barree–Conway model, obtained for Reynolds numbers up to $Re_p = 1\,000$ which is

$$K^* = 0.044 + \frac{1 - 0.044}{\left(1 + (Re_P/512)^{1.521}\right)^{2.157}}. \tag{5.4}$$

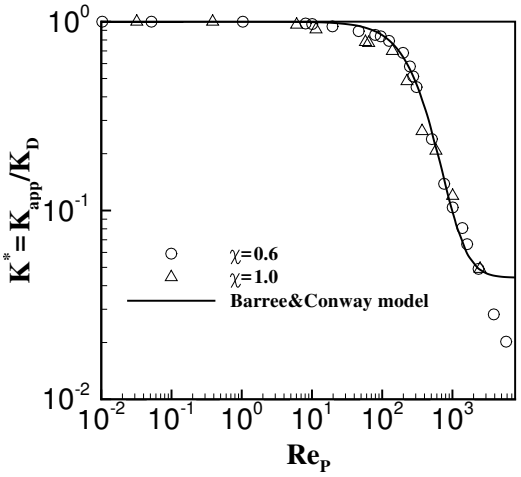

Figure 5.7: Normalized permeability (K^*) versus Reynolds numbers of flow through the simple sphere pack.

We see that the results can be fitted well to the model equations that is in agreement with the experimental validations reported in (*Barree and Conway*, 2004; *Lopez-Hernandez*, 2007; *Lai et al.*, 2012). However, for higher Reynolds numbers, we observe a significant deviation from the plateau region that is postulated by the model. This indicates that, although the Barree–Conway model can be adjusted well for flow simulations in the range up to $Re_p = 1\,000$, it lacks enough degrees of freedom to model flow beyond that range. Including the additional data for high Reynolds numbers increases the fitting error in the low Reynolds regime, where the model has been validated by previous studies of various authors. Furthermore, based on our observations, we moreover conclude that $K_{\min}$ in the model does not have the physical meaning of a minimal permeability that is attained at the high Reynolds limit. It should rather be considered as a free model parameter that can be chosen to fit the curves for a porous medium at hand in the regime $Re_p < 1\,000$. To the best of our knowledge, no experimental setup or numerical simulation is available that exhibits the plateau behavior at high Reynolds numbers.

5.4.3 Friction factor

A non-dimensional form of equation (5.2) can be provided in the form of a friction factor, i.e.,

$$F_K = \frac{1}{Re_K} + F, \tag{5.5}$$

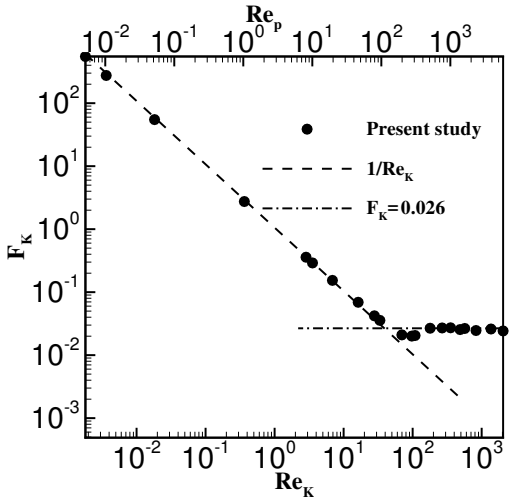

Figure 5.8: Permeability-based friction factor of the simple sphere pack with $\chi = 0.6$ versus the permeability-based Reynolds numbers and the particle diameter-based Reynolds numbers.

where $F_K = (\Delta p/L)\sqrt{K}/\rho U^2$, and $Re_K = \rho U\sqrt{K}/\mu$. As we showed in Sec. 5.4.2, the permeability changes in different flow regimes. Therefore, the permeability used in Eq. (5.5) should be carefully selected. The flow is linear and irrotational in the Darcy regime, thus the permeability of the porous media in this regime represents the actual internal structure of the porous medium most accurately. Hence, the permeability determined in the Darcy regime should be used in Eq. (5.5).

Figure 5.8 presents the results of the friction factor for the sphere pack with χ=0.6. Flow regimes can be identified using this results. As it can be seen, for $Re_K < 1$ the results are inversely proportional to Re_K which is the typical behavior of the friction factor in the Darcy regime (*Nield and Bejan*, 2006). The deviation commences at $Re_K = 5$ ($Re_p = 20$) where the inertial flow start to dominate the flow behavior. The transition regime from unsteady flow to chaotic flow happens at $70 < Re_K < 110$ ($180 < Re_p < 300$). By further increasing the Reynolds number, we can see the turbulent flow regime in which the friction factor converges to nearly a constant value that depends on the porous geometry, and is 0.026 for this solid volume fraction. The results of the friction factor of flow through touching spheres is depicted in Fig. 5.8. Similar to the sphere pack with χ=0.6, when $Re_K < 1$ the friction factors of the touching sphere pack are inversely proportional to Re_K in the Darcy regime. In this geometry, the deviation starts earlier at $Re_K = 0.5$ ($Re_p = 11$). This is due to the smaller passages in the touching sphere packing relative to the dilute one, therefore the inertial contribution to the drag force starts at earlier Reynolds number.

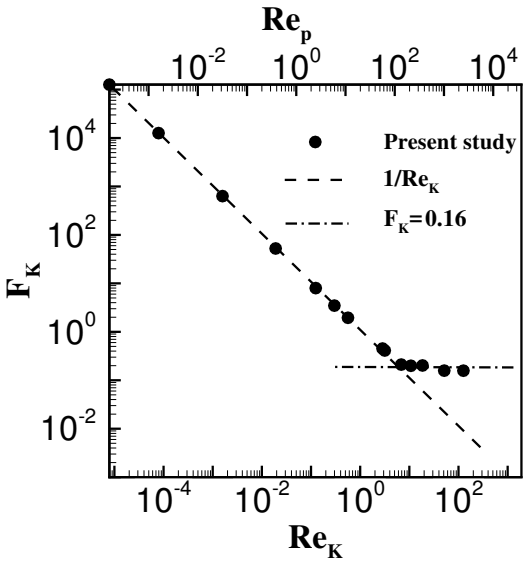

Figure 5.9: Permeability-based friction factor of the sphere pack with $\chi = 1$ versus the permeability-based Reynolds numbers and the particle diameter-based Reynolds numbers.

The unsteady laminar flow begins when $Re_K > 6.9$ ($Re_p > 139$) and the transition regime from unsteady to chaotic flow can be identified in the range $18 < Re_K < 28$ ($369 < Re_p < 582$). By further increasing the Reynolds number, we can see the turbulent flow regime in which the friction factor converges to a nearly constant value of 0.16 for this porous geometry. The obtained friction factor is in line with the recent experimental results presented by *Huang et al.* (2013) for $Re_p < 1000$.

5.5 Summary

In this chapter, we performed simulations to investigate the flow characteristics in a simple sphere pack. Considering two volume fractions, we demonstrated that the Forchheimer constant should be chosen differently at different flow regimes. Evaluation of the Barree-Conway model revealed that there is no plateau area for the permeability at high Reynolds number. Using the friction factor model, we could distinguish between flow regimes and define the transition Reynolds number.

Following the findings in this chapter for the structured array, we will present the investigation flow through a random and unstructured array in the next chapter.

6 Flow through unstructured packed beds

In this chapter, we extend our LBM simulation for the unstructured packing of different particles. We describe how the packing is constructed as well as the simulation strategy used to simulate flow through the packing. This is followed by investigating the packing characteristics, namely, we compare results of the permeability with available literature data for packed beds.

6.1 Creating the packed bed

A few numerical techniques were proposed by previous studies to generate the random packing of spheres. These techniques can be divided into two categories, namely sequential addition and collective rearrangement. The construction is based on some assumption for packing growth and they have different criteria for the stability. Since these methods do not consider the interaction of the particles and the force, the packing constructed by theses methods are not comparable to the real packing structure (*Liu et al.*, 1999).

In this study, to construct a semi-real porous structure, we use the in-house multi-body dynamics framework physics engine (pe) (*Preclik and Ruede*, 2015). The pe can simulate the motion of rigid bodies and their interaction by frictional collisions. Here we use this functionality to generate a sphere packing. Several spherical particles with the same diameter are initialized such that they fall under their own weight and collect at the bottom of the bed. After the spheres came to rest, their position is fixed and their geometry defines the solid matrix of a porous structure. The pore space is then resolved by a lattice Boltzmann grid in the waLBerla framework.

6.2 Packed beds of spherical particles

Analytic formulas for the acting drag force on particles in unbounded flow are often restricted to single, isolated particles, and low Reynolds numbers. For example, *Hinch* (1977) calculated the drag force for dilute spherical packing. This study was extended by *Kim and Russel* (1985) to cover volume fractions up to 0.5. *Carman* (1937) proposed an estimate for larger volume fractions, albeit only for low Reynolds numbers.

To-date, no analytical solution was found for high Reynolds numbers and larger solid volume fractions. With respect to this regime, correlations were obtained from experimental and numerical tests. The most important correlations that are commonly used in practical applications were proposed by *Ergun* (1952) and *Wen and Yu* (1966). These correlations were obtained empirically by measuring the pressure drop and flow rates. The Ergun correlation defines the pressure drop based on the superficial velocity (denoted as v_s), the porosity (denoted as ϵ), and the particle diameter (denoted as D) as follows:

$$\frac{\Delta p}{L} = 150\frac{(1-\varepsilon)^2\,\mu}{\varepsilon^3 D^2}v_s + 1.75\frac{(1-\varepsilon)\,\rho}{\varepsilon^3 D}v_s^2 \tag{6.1}$$

where ρ denotes the density, L denotes the length of the channel, and μ is the viscosity. The two constants, 150 and 1.75, were obtained from fits to experimental data. These two constants are not general and different values were proposed by other experimental studies (*Fand et al.*, 1987; *Seguin et al.*, 1998a,b).

The first correlations for the drag force based on the DNS were provided by *Koch and Sangani* (1999); *Hill et al.* (2001) and *Hill and Koch* (2002) using LBM simulations. *Hoef et al.* (2005) and *Beetstra et al.* (2007) investigated mono- and bi-disperse spherical packing and proposed a correlation for the same. *Bokkers et al.* (2004) used a coupled simulation of CFD and DEM to illustrate that performing the simulation by using the correlation proposed by *Hill et al.* (2001) results in better agreement with experimental measurements than that of the simulations using Ergun and Wen-Yu correlations.

Tran-Cong et al. (2004) experimentally investigated the drag force for isolated non-spherical particles that were constructed from several spherical particles. *Beetstra et al.* (2006) compared LBM simulation results to the experimental data obtained by *Tran-Cong et al.* (2004), and showed that the numerical results were in a good agreement with the experimental data. *Chen et al.* (2015) investigated a packed bed

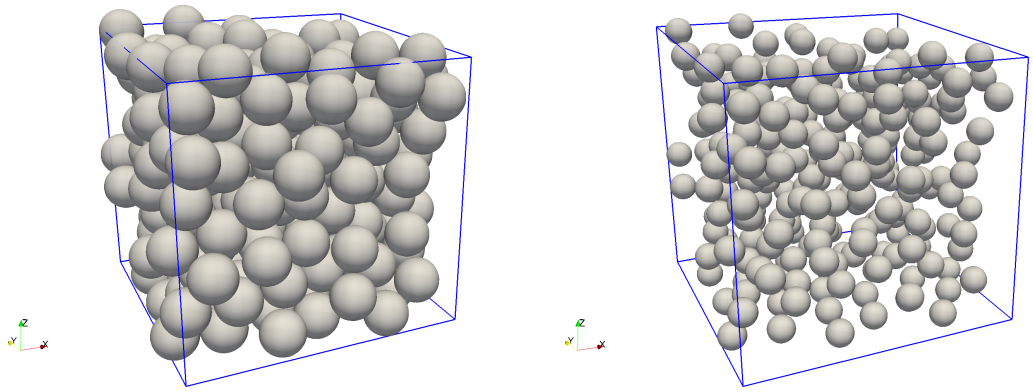

(a) dense packing (b) dilute packing

Figure 6.1: Packing structures simulated by pe including 360 spheres, a) dense sphere pack $\epsilon = 0.42$, a) dilute sphere pack $\epsilon = 0.87$.

including approximately cubic particles constructed by spherical particles. They examined the correlation proposed by *Beetstra et al.* (2006), for spherical particles, and provided a correlation that also accounted for the solid volume fraction of the packing.

6.2.1 Simulation setup

Following the findings in chapter 5, we now investigate flow through spherical packed bed. In this section, we use the TRT collision scheme with the CLI boundary condition at the sphere surfaces. The unstructured spherical packed bed is shown in Fig. 6.1. Periodicity is assumed in the span-wise direction, and fluid flows from the bottom to the top. By performing the simulation with this setup, we avoid the wall friction effect which is of importance when $L/D < 40$, where L is the column diameter, and D is the particle diameter (*Cheng*, 2011). The macroscopic variables are measured in a box of with a length of $10D$ to represent the elementary volume (REV) correctly. The Darcy law, Eq. (2.6), is used to calculate the permeability.

The porosity of the spherical packed bed that is constructed with the pe simulation is $0.37 < \epsilon < 1$. To change the porosity of the packed bed, first the touching pack, Fig. 6.1(a), will be created by the pe and then, before starting the fluid flow simulation, the spheres are shrunk to achieve the desired porosity as shown in Fig. 6.1(b). For fluid flow simulation, we use 36 cells per diameter of the sphere, and this will be the same for all packing variants.

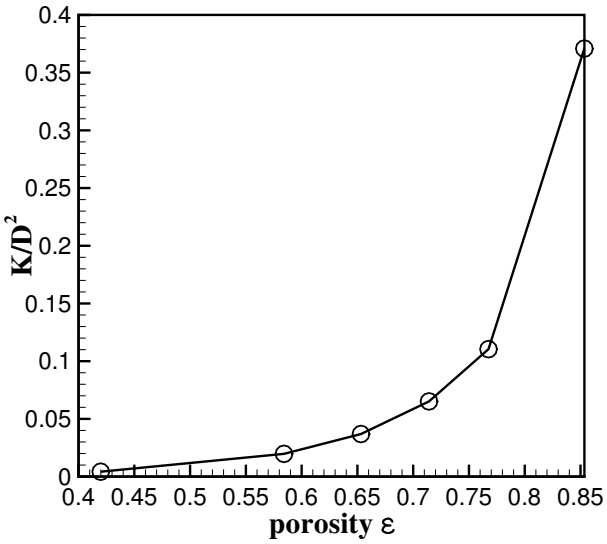

Figure 6.2: Dimensionless permeability of sphere packs with different porosities, $0.42 < \epsilon < 0.85$.

6.2.2 Results and discussion

Several correlations exist to estimate the permeability for spherical packing. One of the widely used model in the laminar flow regime is called Carman–Kozeny (CK),

$$K = \frac{D^2}{36\kappa + 2.871 \left(\frac{Re}{1-\epsilon}\right)^{0.9}} \frac{\epsilon^3}{(1-\epsilon)^2}, \tag{6.2}$$

where κ is a constant that takes the value between 4.17 and 5 (*Prieur Du Plessis*, 1994). Equation (6.2) can be seen as low Reynolds number limit of the Ergun correlation, Eq. (6.1), when $\kappa = 4.17$.

By performing the simulation of fluid flow through sphere packs with different porosities in the range of $0.42 < \epsilon < 0.85$, we measured the permeability, and the results are presented in Fig. 6.2. Our results indicate a different trend in comparison to the CK correlation, Eq. (6.2). Correlating the permeability results in the equation as

$$K = \frac{D^2}{85} \frac{\epsilon^{2.4}}{(1-\epsilon)^2}. \tag{6.3}$$

This difference results from the fact that our simulation is performed for creeping flow with the packing of smooth spherical particles, while the CK correlation is general and provided for the whole range of laminar flows.

To investigate the Reynolds number effect on the permeability, we perform a series

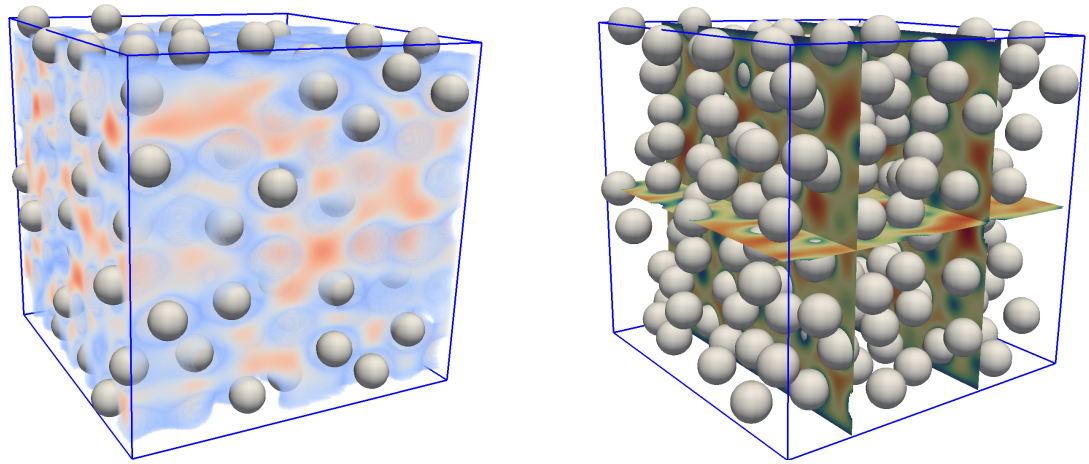

(a) (b)

Figure 6.3: Dilute packing structure containing mono-sized spherical particles with porosity $\epsilon = 0.87$, (a) Volume velocity contour (b) instantaneous velocity contour at Stokes regime.

of simulations for $Re < 100$. Figure 6.4 illustrates the packing structure containing 592 mono-sized spherical particles in a domain with periodic stream- and span-wise flow. At the top and bottom of the domain no-slip conditions are applied so that part of the spheres are cut out of the domain. The diameter of the spheres is set as 40 lattice units, and this domain has the porosity $\epsilon = 0.37$.

The instantaneous flow field at $Re = 65$ is shown in Fig. 6.4(b) with two slices. As it can be seen, the flow field exhibits a complicated structure, in particular, different flow velocities and channelization are noted. In this regime, three main phenomena are noticed: the low velocity close to the spheres, the high velocity in main channels, and the recirculation behind the spheres. This leads to lower flow capacity. The flow field shown in Fig. 6.4 can only provide a qualitative understanding. To be quantitative, the permeability is calculated at different Reynolds number and it is presented in Fig. 6.5. The permeability is normalized with the Darcy permeability, as Eq. (5.3). The result indicates distinct permeability in compare to the isolated particle that we have presented in Fig. 5.6(b). The reason is because of the random position of particles that creates different pore size at different locations. Therefore, the volume average quantities, like the Darcy velocity, will be smaller that leads to a lower value of permeability. The results are also compared to the Carman-Kozney correlation that shows a good agreement.

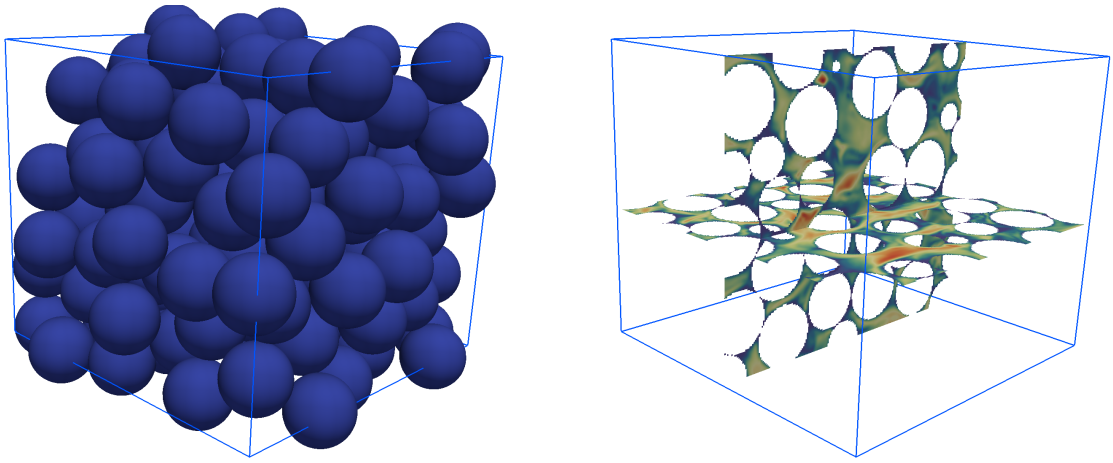

(a) (b)

Figure 6.4: (a) Packing structure containing mono-sized spherical particles with porosity $\epsilon = 0.37$, (b) Instantaneous velocity field contour at $Re_p = 65$.

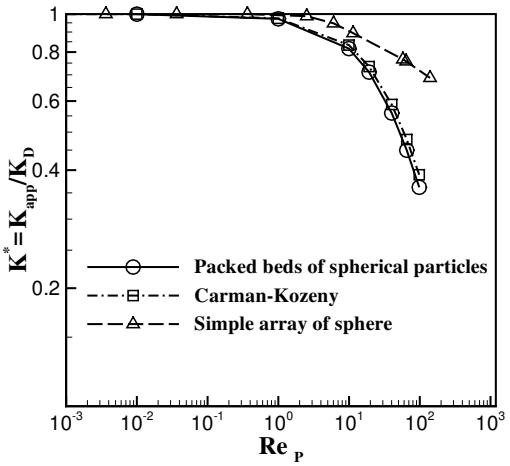

Figure 6.5: Dimensionless permeability versus Reynolds number of dense sphere packing.

6.3 Packed beds of non-spherical particles

Real particles, both artificial and natural, have different shapes ranging from a roughly spherical glass to highly irregular shapes of fibrous or biomass materials. In many important applications, such as absorption, processes such as gasification, pyrolysis and carbonization (*Allen et al.*, 2013), and several syntheses reactors (*Kunii and Levenspiel*, 1991), the particles are not spherical. The pressure drop through porous media, e.g., packed beds, must be known for successful and effective design, operation, and optimization of the system. The shape, solid volume fraction, and

the orientation of the particles strongly affect the flow behavior (*Nikku et al.*, 2014; *Hölzer and Sommerfeld*, 2008; *Zastawny et al.*, 2012). Therefore, it is necessary to study the effect of the particle shape on the resulting pressure drop through the packed beds in detail.

Although particles are not spherical in most practical applications of packed beds, the investigation of packed beds including spherical particles has attracted considerable research interests. This oversimplification is presented in a vast number of numerical simulations that completely ignore the effect of particle shape (*Zhu et al.*, 2008). The main reasons for the restriction of spherical particles include the difficulty in creating the packing by using non-spherical particles, and difficulties involved in finding a general drag force correlation for non-spherical particles.

Although the fore-mentioned correlations are generally accepted to provide reasonable results for spherical particles, the extension to non-spherical particles is not straightforward. It has been shown that the microscopic behavior of the flow as well as the macroscopic properties are strongly affected by the structure of the packed beds (*Guardo et al.*, 2006; *Freund et al.*, 2003). One of the most common approaches to deal with non-spherical particles is to use an effective diameter of the particles and use the Ergun correlation. However, *Nemec and Levec* (2005) showed that using only an effective diameter is not sufficient to cover all effects of non-spherical particles in the flow field. They proposed changing the constants in the Ergun correlation to a function of particle size.

It has also been reported that the Ergun correlation under-predicts the pressure drop of rocks by a factor of almost 5 (*Beasley and Clark*, 1984; *Tobiś*, 2000). *Allen et al.* (2013) showed that the pressure drop through the packing of non-spherical particles, such as rough spheres, smooth cylinders, and cubes, are significantly higher than the one predicted by the Ergun correlation.

The effects of particle orientation and Reynolds number on the drag force has been investigated by *Hölzer and Sommerfeld* (2008). They used experimental data and numerical simulation to provide a correlation for the drag force exerted on non-spherical particles. However, since they did not consider the solid volume fraction, it can not be used for the packed beds. *Hua et al.* (2015) proposed a model for the drag force for dilute and dense solid volume fractions that considers the particle shape. They compared their results to the experimental results and showed that the proposed model predicts the pressure drop with a relatively better agreement both in the micro-scale and the macro-scale. However, they introduced a particle sphericity that has to be calibrated by an experimental measurement a priori.

In contrast to the spherical particles, the irregular or non-spherical particles feature a complicated flow field that results in a large discrepancy of the drag force and permeability when compared to spherical particles (*Zastawny et al.*, 2012; *Guo et al.*, 2011).

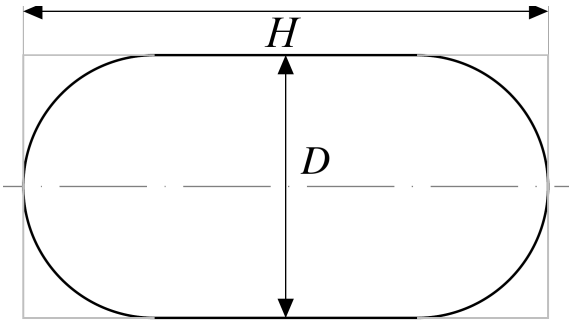

Figure 6.6: Schematic of spherocylinder in two dimension with the length of H and diameter of D.

6.3.1 Results and discussion

In the following, we will first investigate the main parameters specific to non-spherical particles.

Shape factor

It is extremely challenging to determine a shape factor to find the effect of the shape of the particles on flow properties. Several shape factors have been introduced and widely used (*Chhabra et al.*, 1999; *Tran-Cong et al.*, 2004; *Bouwman et al.*, 2004) in the literature. The sphericity of particles may be the most appropriate single parameter to describe the deviation from a spherical shape. The sphericity is defined as the ratio between the surface area of the volume equivalent sphere and the surface area of the considered particle. This factor provides a general description of the particle shape and can enter the correlations of the drag forces of the non-spherical or irregularly shaped particles.

The sphericity of the spherocylindrical particle decreases by increasing the aspect ratio. We define the aspect ratio as $Ar = H/D$, where H represents the length of the spherocylinder and D is its diameter (cf. Fig. 6.6). Four different aspect ratios of $Ar = 2.5, 3.5, 4.5$, and 6.5 are considered to investigate the effect of the aspect ratio on the flow field. Figure 6.7 shows packing structured with different aspect ratios.

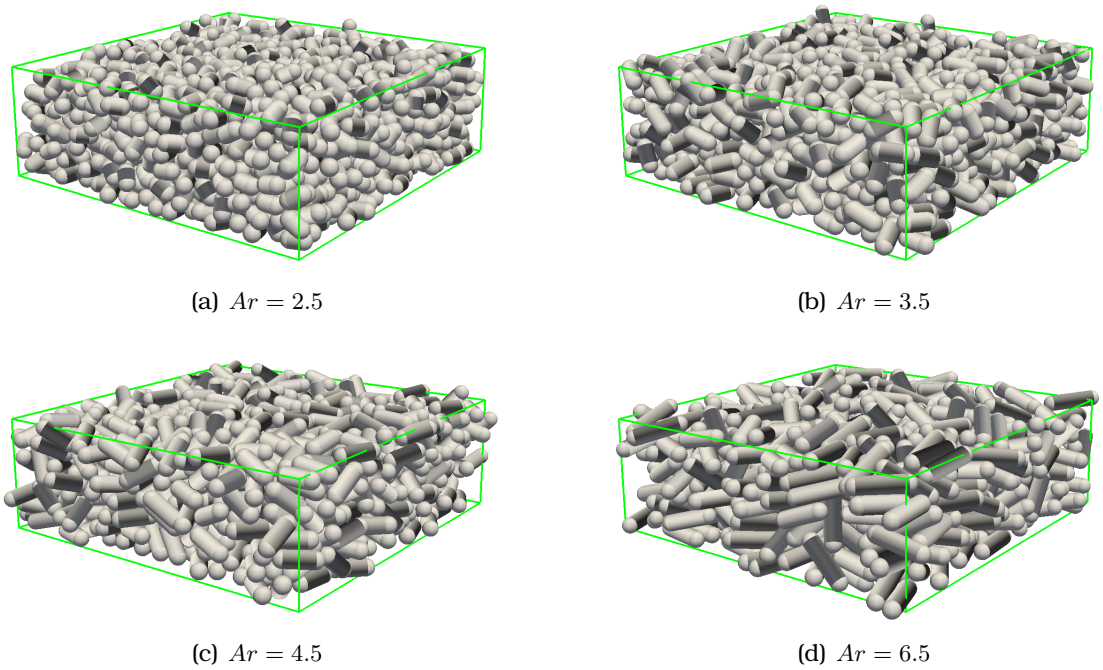

(a) $Ar = 2.5$ (b) $Ar = 3.5$

(c) $Ar = 4.5$ (d) $Ar = 6.5$

Figure 6.7: Packing structure of spherocylindrical particles with different aspect ratios, a) $Ar = 2.5$, b) $Ar = 3.5$ c) $Ar = 4.5$, d) $Ar = 6.5$.

It should be noted that the packing constructed by the spherocylinder with higher aspect ratio includes fewer particles in the domain with the same volume. The number of particles in the simulation ranges from 495 to 953.

The results of the simulation with different aspect ratios are presented in Fig. 6.8 and show the measured permeability and porosity. The results show that aspect ratio has a weak effect on the porosity of the packing, and it has a narrow range of $0.29 - 0.39$. It should be noted that the packing constructed by the spherocylinder can have lower porosity than the dense sphere pack.

However, the permeability is strongly affected by the aspect ratio. First, it decreases with increasing aspect ratio until the critical porosity of $Ar = 4$, and then increases. We note that at $Ar = 4$, the packing has also the minimum porosity. This effect is mainly related to the channelization and tortuous pathway. At small aspect ratios, the particle shape is similar to the shape of a sphere, but by increasing the aspect ratio, the cylindrical part of the spherocylinder affects the pore geometry and results in a lower void for the fluid to flow. By increasing the aspect ratio, the number of the direct channels increases compared to the tortuous pathway. Therefore, the permeability, which is the flow capacity, increases.

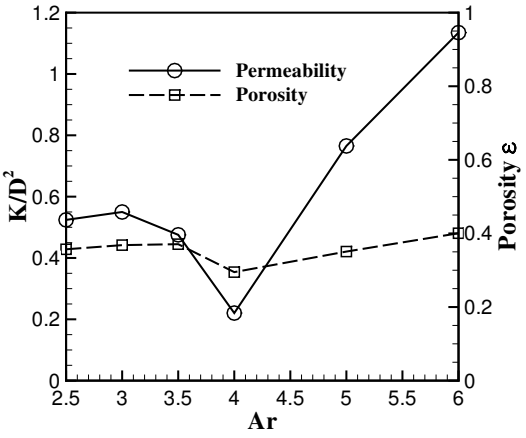

Figure 6.8: Effect of the aspect ratio on permeability and porosity of the spherocylinder packing.

Another parameter that can affect the flow is the orientation of the particles. In contrast to the spherical packing, flow through the packing constructed by non-spherical particles is sensitive to the orientation of the particles. The same spherocylindrical particles can form several different pore geometries due to the orientation. This adds to the complexity of pore geometry. We measured the orientation of the particles with respect to the stream-wise direction. The probability of the orientations are shown in Fig. 6.9 for different aspect ratios of $Ar = 3, 4$, and 5. The maximum frequency is in zero degrees, and this implies that the particles are oriented in the stream-wise direction. Also, different aspect ratios do not show significant differences among each other. Therefore, this parameter has relatively smaller effect when compared with those of the porosity and the aspect ratio.

Velocity field

It is necessary to define the length scale, i.e., the effective diameter, to calculate the Reynolds number. With respect to the non-spherical particle, the definition of the effective diameter is ambiguous. Various definition have been used in the literature, namely, equivalent surface volume diameter $D_{sv} = 6\frac{\sum V_p}{\sum A_p}$, diameter of a volume equivalent spherical particle $D_{eq} = \left(\frac{6}{\pi}V_p\right)$, and the hydraulic diameter $D_H = \frac{4A}{P}$, where V, A, and P denote volume, surface, and the wetted perimeter of the cross-section, respectively. In this study, we use the hydraulic diameter to calculate the Reynolds number, as well as to normalize the permeability.

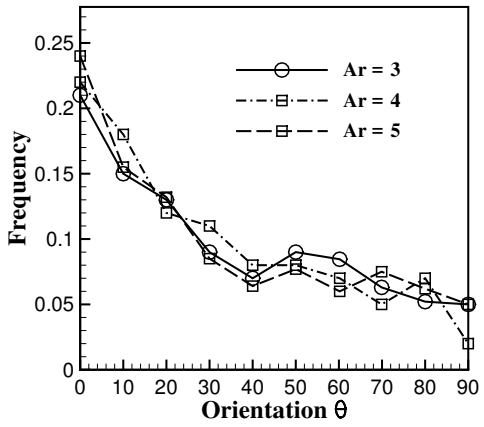

Figure 6.9: Orientation probability in the packing of the spherocylindrical particles of different aspect ratios $Ar = 3, 4$, and 5.

Figure 6.10 shows the simulation domain of the spherocylinder packing with $Ar = 3.5$. The flow field at $Re_{D_H} = 16$ is shown in Fig. 6.11. Although the Reynolds number is low, closer inspection of the velocity field, Fig. 6.11(a), reveals chaotic flow behavior at some positions. The streamlines presented in Fig. 6.11(b) shows the flow complexity and tortuous path. It is worth to note that the Reynolds number is measured based on the time-averaged Darcy velocity, and the maximum velocity in the simulation domain is about 50 times larger than the Darcy velocity.

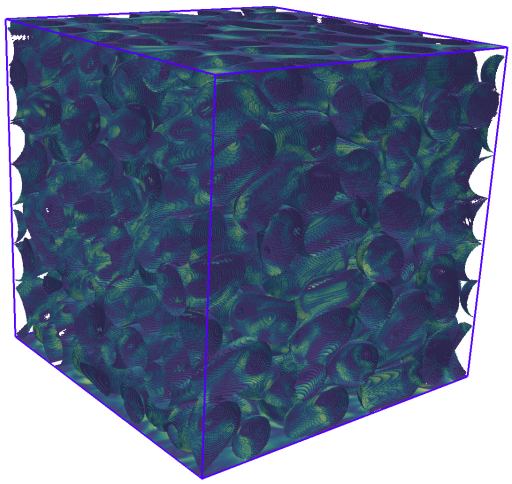

Figure 6.10: The simulation domain of the mono-sized spherocylinder packing

Figure 6.12 depicts the permeability that is normalized by the hydraulic diameter versus the Reynolds number. Results of different aspect ratios, namely $Ar = 3, 4$ and

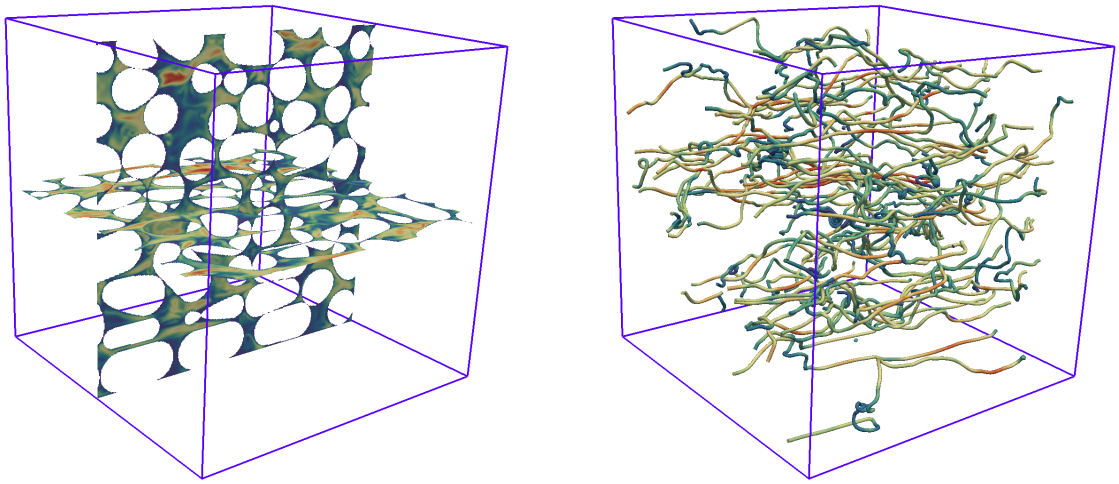

(a) (b)

Figure 6.11: (a) Slices of the instantaneous velocity field contour of spherocylinder packing with $Ar = 3.5$, (b) streamlines at $Re_{D_H} = 16$.

5, are presented. For all cases, by increasing the Reynolds number the permeability decreases.

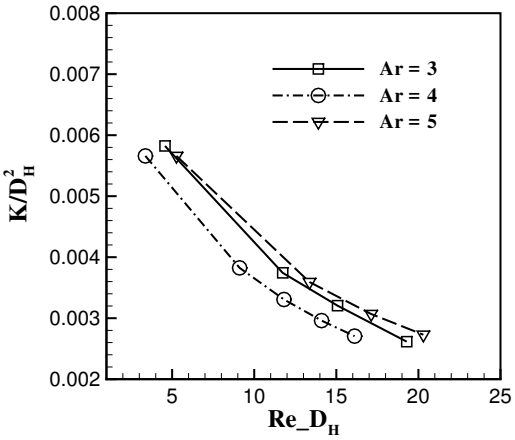

Figure 6.12: Normalized permeability as a function of Reynolds number based on the hydraulic diameter of the mono-sized spherocylinder packing.

6.4 Flow through pack of non-uniform particles

To highlight the ability of the developed code to deal with complex geometries, in the section we also present an illustration of flow through packing of non-uniform particles that is constructed by sphere and spherocylinder particles. The packing can be constructed with cubic, spherical, and spherocylinderical particles. Figure 6.13 illustrates the construction of non-uniform packing.

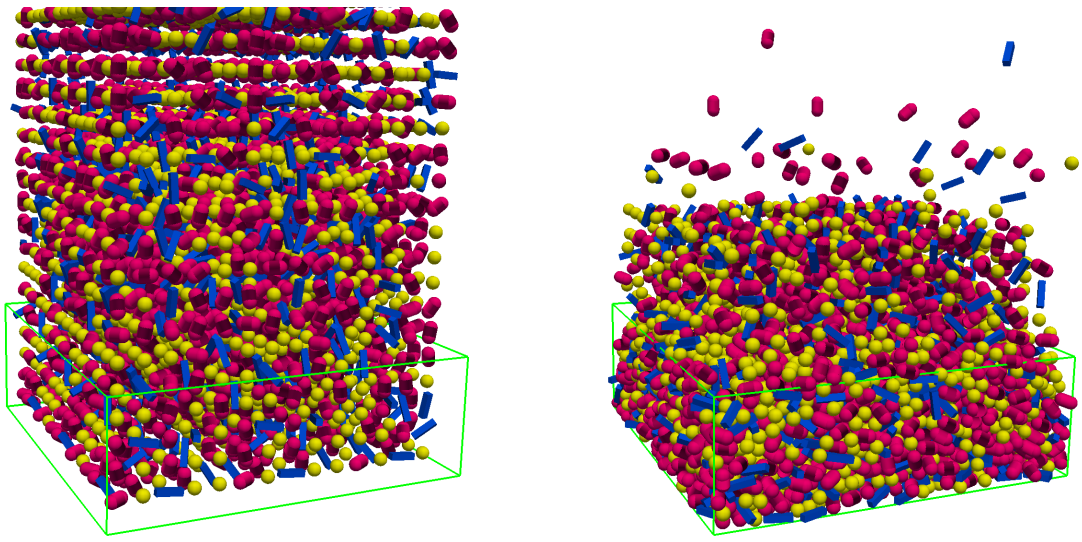

(a) (b)

Figure 6.13: Packing structure of mixed particles with the same hydraulic diameter, sphere, cuboid, and spherocylinder.

Simulation of fluid flow through the packing containing spheres and spherocylinders has been performed and the results are presented in Fig. 6.14. Detailed investigation of the effect of particle shape, orientation, and isotropy of the packing on the pressure drop can be performed by the available framework. However, this is out of the scope of this work.

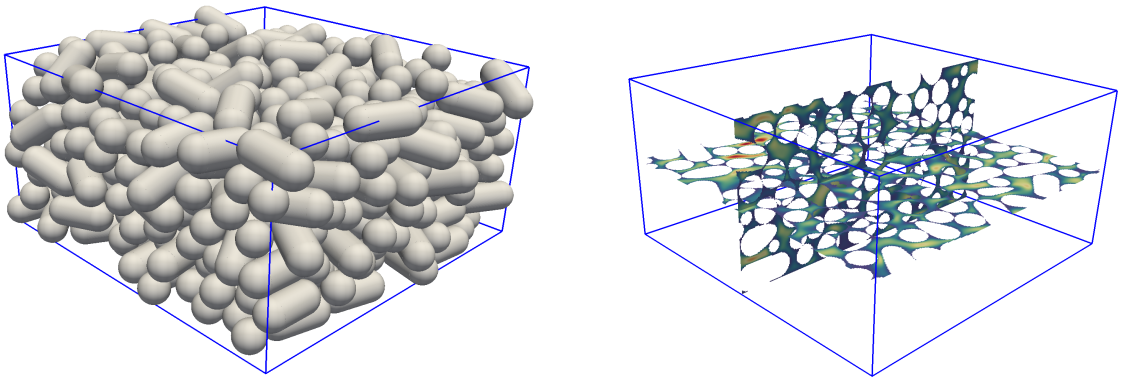

(a) (b)

Figure 6.14: Non-uniform packing containing spheres and spherocylinders, (a) packing structure, (b) instantaneous velocity contour .

6.5 Summary

In this chapter, the result of flow simulation in unstructured packed beds was presented. Dense and dilute spherical pack is considered in the simulation of flow in Stokes regime and a correlation proposed for the permeability. Packed beds containing non-spherical particles were investigated. Effect of the shape of the particle, orientation, and Reynolds number on the permeability were investigated and results are described in detail. An illustration of packed beds containing non-uniform particles were provided to exhibits the ability of the framework.

In the next chapter, we examine a free flow over porous media.

7 Free flow over permeable beds [1]

7.1 Introduction

The representative elementary volume (REV) is defined as the minimal element for which macroscopic characteristics of a porous flow can be observed. To describe the flow in the bulk of the porous medium, Darcy's law, Eq. (2.6), is commonly used. However, when a porous medium and a free flow domain co-exist, different approaches based on two-domain or on single-domain models are available. Using a single-domain in combination with the Brinkman equation that modifies Darcy's law by a viscous term

$$-\mu_{\text{eff}}\nabla^2\boldsymbol{u} + \mu\boldsymbol{K}^{-1}\boldsymbol{u} = \boldsymbol{F} - \nabla p, \tag{Br}$$

where $\boldsymbol{F}$ is the body force, allows to model a smooth transition (see e.g. *Alazmi and Vafai* (2001); *Nield and Kuznetsov* (2009); *Le Bars and Worster* (2006)). Here μ_{eff} is an effective dynamic viscosity in the porous region. However, determining appropriate viscosity parameters for the Brinkman model in the transient region is challenging (*Le Bars and Worster*, 2006; *Goyeau et al.*, 2003; *Chandesris and Jamet*, 2009). Furthermore, the penetration of flow into the porous medium is found to depend on the roughness coefficient of the surface; see e.g. *Goharzadeh et al.* (2005); *Ghisalberti* (2010); *Morad and Khalili* (2009); *Pokrajac and Manes* (2009).

Alternatively, one can use a two-domain approach in combination with a sharp interface transmission condition. Considering the (Navier-)Stokes equation in the free flow region and the Brinkman (or Darcy) equation in the porous region, the interface plays an important role. Proceeding from the experimental investigation of Poiseuille flow over a porous medium, *Beavers and Joseph* (1967) introduced an empirical approach that agreed well with their experiment; see also *Nield and Kuznetsov* (2009): They suggested to use a slip-flow condition at the interface, i.e.,

[1] Most parts of this chapter are published in "E. Fattahi, C. Waluga, B. Wohlmuth, and U. Rüde (2016), Large scale lattice Boltzmann simulation for the coupling of free and porous media flow, High Performance Computing in Science and Engineering, HPCSE 2015, Czech Republic, May 25-28, 2015, Revised Selected Papers, pages 1–18. Springer International Publishing."

the velocity gradient on the fluid side of the interface is proportional to the slip velocity. For simplicity, we consider a domain for which the interface is aligned with the flow direction. The Beavers¬Joseph relation is formulated as

$$\left.\frac{dU}{dz}\right|_{z=0^+} = \frac{\alpha}{\sqrt{k}}\left(U_s - U_m\right), \tag{BJ}$$

where z denotes the coordinate perpendicular to the interface, $U = U(z)$ is the mean velocity in flow direction, U_s is the slip velocity at the interface $z = 0^+$, U_m is the seepage velocity that is evaluated far from the plane $z = 0$ in the porous region, k is the permeability, and α is a phenomenological dimensionless parameter, only depending on the porous media properties that characterize the structure of the permeable material within the boundary region which typically varies between 0.01 and 5 (*Nield and Bejan*, 2006; *Duman and Shavit*, 2009). We refer to (*Baber et al.*, 2012; *Mosthaf et al.*, 2011) and the references therein for the interface coupling of two-phase compositional porous-media flow and one-phase compositional free flow.

In 1971, Saffman (*Saffman*, 1971) found that the tangential interface velocity is proportional to the shear stress. He proposed a modification of the BJ condition as

$$\frac{\sqrt{k}}{\alpha}\left.\frac{dU}{dz}\right|_{z=0^+} = U_s + O(k). \tag{BJS}$$

More than two decades later, *Ochoa-Tapia and Whitaker* (1995) proposed an alternative modification of the BJ condition which includes the velocity gradient on both sides of the interface as

$$\mu_{\text{eff}}\left.\frac{dU}{dz}\right|_{z=0^-} - \mu\left.\frac{dU}{dz}\right|_{z=0^+} = \frac{\mu}{\sqrt{k}}\beta U_s. \tag{OTW}$$

Here the jump-coefficient β is a free fitting parameter that needs to be determined experimentally (*Martys et al.*, 1994). Different expressions for the effective viscosity μ_{eff} can be found in the literature. For instance, *Lundgren* (1972) suggested a relation of the form $\mu_{\text{eff}} = \mu/\epsilon$, where ϵ is the porosity.

All of the interface conditions mentioned above require the a priori knowledge of the exact position of the interface (*Zhang and Prospretti*, 2009; *Nabovati et al.*, 2009; *Liu and Prospretti*, 2011), which is for realistic porous geometries often not the case. Additionally both, single-domain and two-domain, homogenized models rely on assumptions whose validity is not automatically guaranteed and depend on additional parameters. Traditional experiments to validate and calibrate such models are often costly, time consuming and difficult to set up.

As a next step in this direction, we here carry out a direct numerical simulation of free flow over a porous medium. The model porous media geometry is constructed by generating a random sphere-packing using the same simulation as described in Sec. 6.1. For the fluid flow simulation, we use the CLI boundary condition with TRT collision operator using D_3Q_{19} lattice model.

We use the results of the direct numerical simulation of flow over and through the porous media as reference solution and evaluate several sharp-interface conditions. As a further example, we also use a homogenized lattice Boltzmann model as a REV scale simulation and show the capability of this model to reproduce the pore-scale results with high accuracy.

7.2 Laminar flow over a permeable bed

The particles have different sizes and their radius is uniformly distributed in a range $[0.5D_m, 1.5D_m]$ where the parameter D_m denotes a mean diameter. For the fluid flow simulation using the LBM, the TRT collision operator and the CLI solid boundary condition are used. We recall that from chapter 4, this combination is fast, has second order accuracy, and shows no viscosity-dependency.

First, we test the influence of the resolution on the averaged stream-wise velocity. To do so, we increase the diameter D of the spheres from 4 to 48 and keep $Re_D = \frac{U_{\max} D}{\nu}$ constant. The domain has two walls at the top and bottom, and periodic boundary conditions are applied at stream-wise and span-wise directions. A constant pressure drop drives the flow, and the data are set such that $Re_D \approx 2$. The simulation result is presented as a planar average of the stream-wise velocity in Fig. 7.1 while it is normalized using the maximum velocity and the height of the channel as a reference value. The results show that beyond $D = 32$ (lattice cells) a further increase of the resolution does not significantly change the results. It is worth to note that in the porous region a coarse lattice can be used and that only the transient region requires a higher resolution.

Figure 7.2 shows the planar average stream-wise velocity, that is normalized by the maximum velocity, at different Reynolds numbers. To change the Reynolds number, the viscosity and particles diameter are kept constant while the pressure gradient is changed to adjust the flow velocity. The results show that the normalized velocity in the porous region at low Reynolds number is considerably higher than those for fast flow. When the Reynolds number of the flow increases, the result indicates that

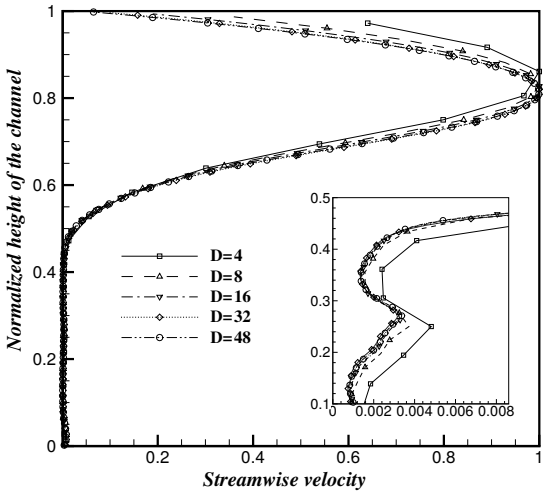

Figure 7.1: Planar average stream-wise velocity for different grid sizes, $Re_D \simeq 2$.

the position of the maximum velocity shifts toward to the top wall. This phenomena is due to the boundary layer effect, however, the exact reason needs more detailed investigation which is out of the scope of this work.

In Fig. 7.2, we observe a small deviation in the velocity profile close to the bottom wall in the porous region. This is because of high porosity close to the wall, where spherical particles are in contact with a flat plane. Consequently a higher permeability region is created, and flow will accelerate because the resistance against the pressure difference is lower than that of the interior of the porous medium. Therefore, to evaluate the existing models without this effect and having a more uniform porosity in the porous region, a different set-up structure is chosen. The bottom plate of the particle simulation is placed about one particle size below the bottom wall of the fluid flow simulation. With this structure the porosity does not have the effect of placing a sphere on the wall, and therefore we create an approximately uniform permeability distribution in the porous medium.

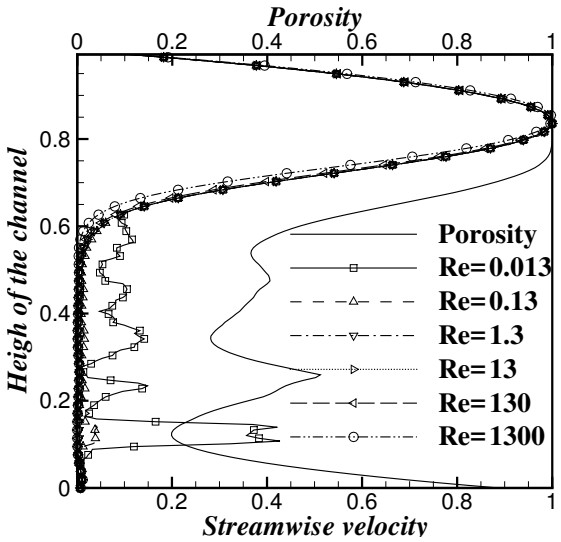

Figure 7.2: Flow over mono-sized particles at different Reynolds numbers.

7.3 Evaluation of different interface conditions

In this section, we evaluate different two-domain approaches. All interface conditions under consideration have parameters for which no explicit relation is known. In the BJ and BJS models, the slip coefficient, α, is unknown, while in the OTW model, the jump coefficient β and the effective viscosity μ_{eff} are unknown and in the Br model, the effective viscosity μ_{eff} is unknown.

7.3.1 Reference DNS result

Using the DNS solution, we can calculate the optimal values for the unknown parameters. The domain that is used is a channel which is periodic in stream-wise and span-wise directions, Fig. 7.3. A free fluid flows on the top of a porous media. To make the comparison independent of the setup, all of the flow properties are non-dimensionalized.

The result of the following pore-scale simulation is taken as a reference solution. Here, we use 1274 particles with radius in the range of $[16, 48]$ cells. A laminar flow is driven by pressure difference of 10^{-6} (in lattice units), and the simulation is run until the flow reaches the steady state. The planar average of the stream-wise velocity is depicted in Fig. 7.4.

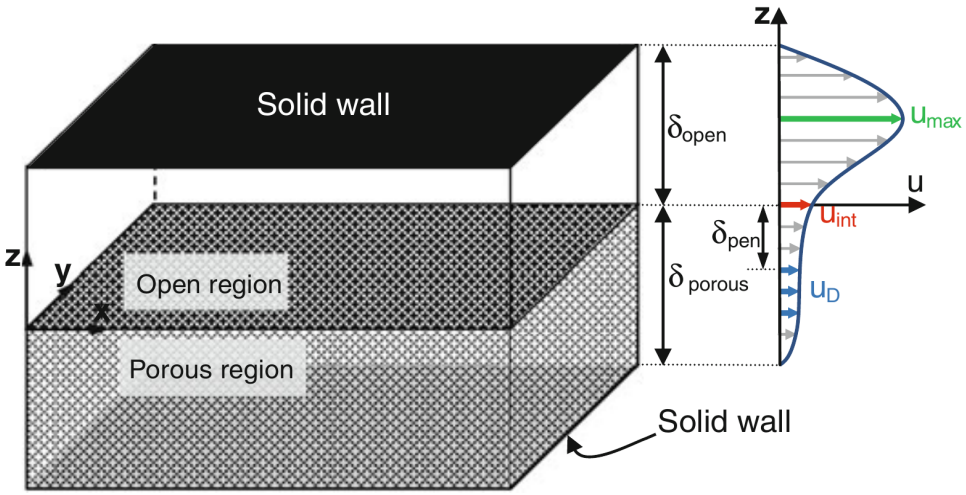

Figure 7.3: Schematic of the simulation domain and averaged velocity profile in the open and porous regions.

7.3.2 Effect of the transition control parameters

The value of the interface velocity U_{int}, can be directly obtained from the averaged velocity profile of the DNS. In order to obtain the velocity gradient on the free flow and porous sides, curve fitting techniques are used to approximate the velocity profile close to the interface. The velocity profile on the free flow side can be well approximated by a polynomial curve and on the porous side, the velocity profile can be approximated by an exponential curve. Permeability and seepage velocity (Darcy velocity) can be calculated from the velocity profile far from the interface in the porous medium. Given this, the unknown variables can be calculated from the Eqs. (BJ), (BJS) and (OTW). However, to do so, the exact position of the interface should be defined which in real applications is nearly impossible.

To find out how the additional parameters of the interface conditions affect the results, a two-domain approach is chosen and the equations are solved analytically. For the free flow region, the Stokes equation is used and for the porous region, the Brinkman equation is chosen. The permeability is calculated from the DNS result far enough from the interface inside the porous region. In Fig. 7.5, we depict the planar average stream-wise velocity which is normalized based on the maximum velocity in the DNS solution.

As it can be seen in Fig. 7.5(a), in the Brinkman model by increasing the viscosity ratio, $J = \frac{\mu_{\mathrm{eff}}}{\mu}$, the maximum velocity decreases and produces a discontinuity in the shear stress over the interface. In the OTW model, Fig. 7.5(b), negative values of β

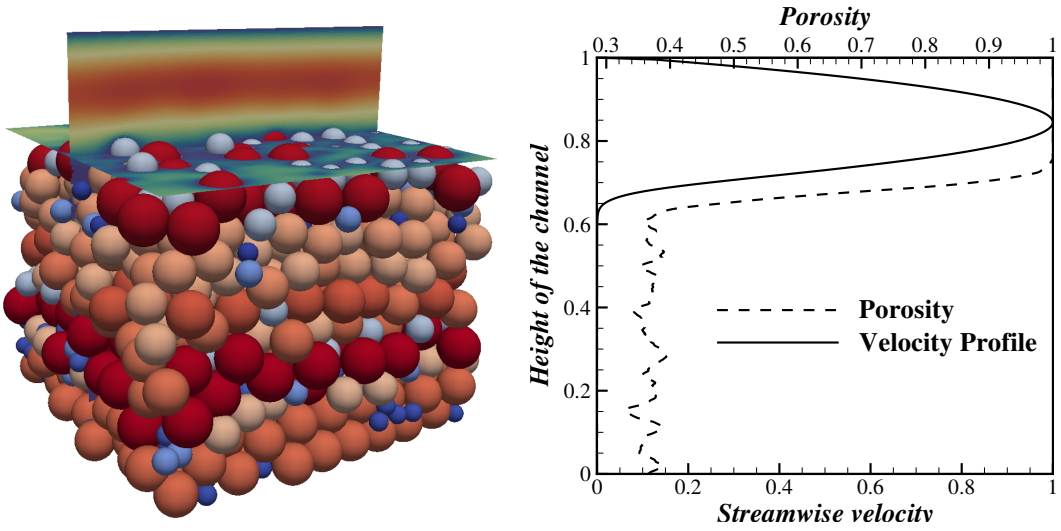

(a) pore geometry and velocity field (b) planar average of stream-wise velocity

Figure 7.4: pore-scale simulation of free flow over porous media.

do not influence the result significantly, however, positive values of β have a strong impact on the maximum velocity as well as on the slip velocity on the interface. Figure 7.5(c) and Fig. 7.5(d) show the results for the BJ and the BJS interface conditions. It can be observed that there is almost no difference between these two models for low Reynolds number flows. In both these cases, the maximum velocity decreases if α increases. A small value of α results in a considerably larger maximal velocity than in the two other cases.

7.3.3 Effect of the interface position

Quite often two-domain models result in discontinuities in the stress at the interface. Thus the a priori knowledge of the position of the interface is crucial. One possibility to fix the position of the interface is to take the location where the porosity reaches the limit value one, i.e., $y = 0.756$. However fitting of the DNS velocity profile shows that only up to $y = 0.722$, the curve is fitted well by an exponential function. More precisely, $u(h) = 0.48423 \cdot \exp(0.31195\, h) - 0.48236 \cdot \exp(0.3131\, h)$ yields a root mean squared error of $5.736 \cdot 10^{-6}$. The pure fluid flow velocity profile is fitted to a 2nd order polynomial resulting in $u(h) = (1.9593e-3) + (2.78421e-4)h - (4.48066e-6)h^2$ with a root mean squared error of $9.5815 \cdot 10^{-6}$. This observation motivates an alternative choice of the interface position where the corresponding governing equations will be fulfilled. Calculating the slip coefficient and the jump coefficient for these two

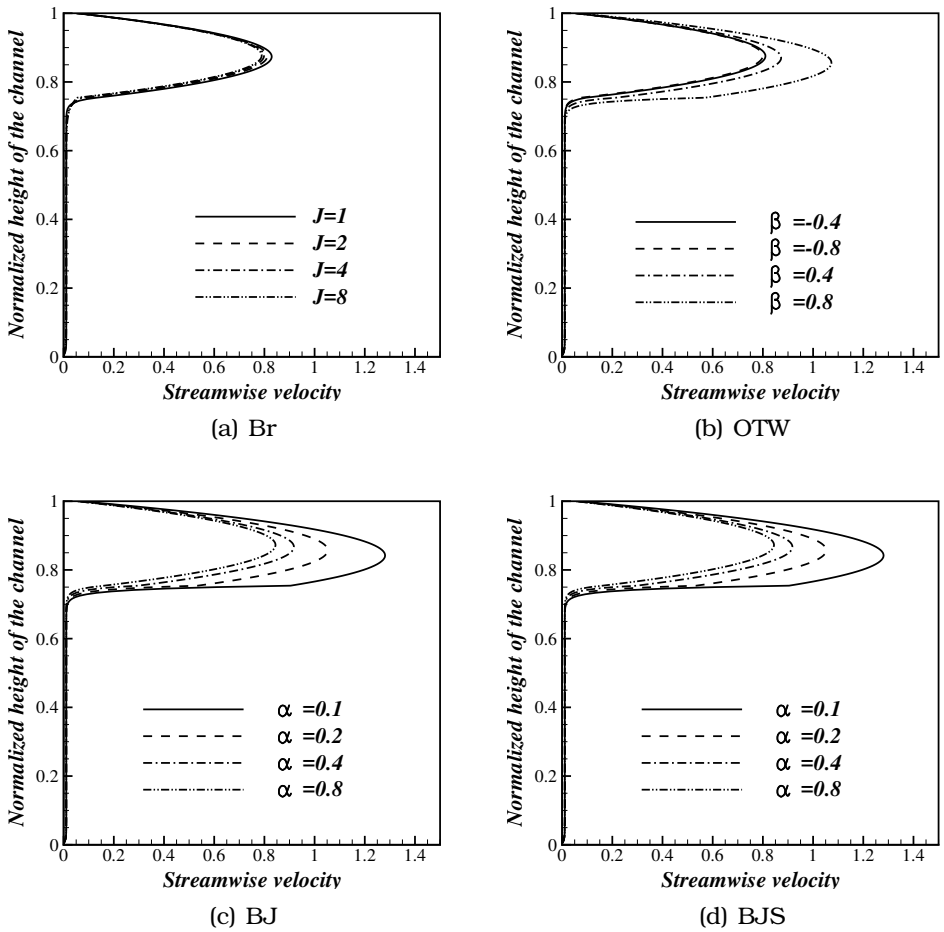

(a) Br (b) OTW

(c) BJ (d) BJS

Figure 7.5: Analytical solution for the velocity profile, which is normalized by the maximum velocity of the DNS solution, by different interface models.

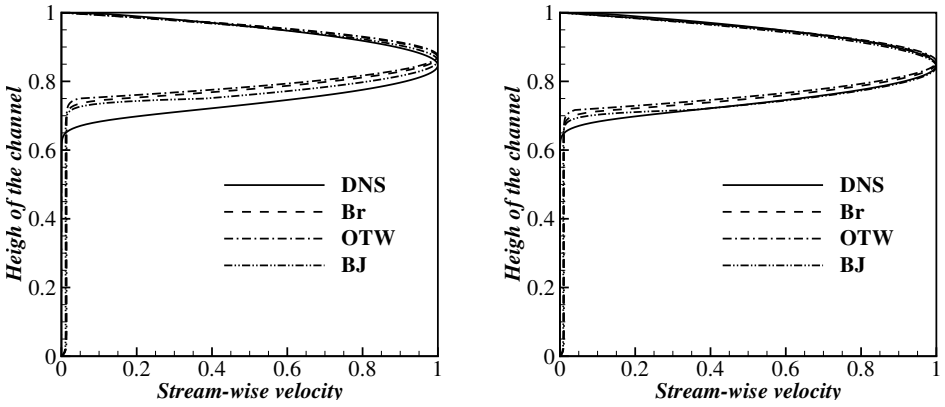

(a) Interface at y=0.756 (b) Interface at y=0.722

Figure 7.6: Normalized velocity profile of the one-domain approaches in compare to the DNS solution; a) interface at y=0.756, b) interface at y=0.722.

positions, we find for $y = 0.756$, $\alpha = 0.3163$, $\beta = -2.8397$ and for $y = 0.722$, $\alpha = 0.31645$ and $\beta = -2.8397$. However, as it can be seen in Fig. 7.6, even with the parameters which are extracted from the DNS results, the considered two-domain approaches cannot represent accurately the DNS solution. Comparing Figs. 7.6(a) and 7.6(b) shows that the two-domain approaches depend strongly on the interface position and more sophisticated criteria for defining the interface location are required to obtain better matching results.

7.4 Numerical simulation with homogenized LBM

The LBM can also be applied to model the fluid flow in porous media at the REV scale. The most commonly used models are the Darcy, the Brinkman-extended Darcy and the Forchheimer-extended Darcy models. This last approach accounts for the flow resistance in the standard LBM by modifying the body-force or equilibrium terms, leading to the recovery of either Darcy-Brinkman's equations or generalized Navier-Stokes equations (*Spaid and Phelan*, 1997; *Freed*, 1998; *Martys*, 2001).

The general model of porous media flow should consider the fluid forces and the solid drag force in the momentum equation (*Nithiarasu et al.*, 1997). *Guo and Zhao* (2002) proposed a model to include the porosity into the equilibrium distribution and added a force term to the evolution equation to account for drag forces of the medium. The non-linear inertial term is not included in the Brinkman model either, and thus, this model is only suitable for low-speed flow. In this approach, the detailed structure of

the medium is ignored, and the statistical properties of the medium are included to represent the porous effects.

In this work, we use the Generalized Lattice Boltzmann Model (GLBM) for porous media introduced in (*Guo and Zhao*, 2002), which is applicable for a medium with both a constant and a variable porosity. The model can be expressed by the following generalized Navier-Stokes equation:

$$\nabla \cdot \mathbf{u} = 0 \tag{7.1}$$

$$\frac{\partial \mathbf{u}}{\partial t} + (\mathbf{u} \cdot \nabla)\left(\frac{\mathbf{u}}{\epsilon}\right) = -\frac{1}{\rho}\nabla(\epsilon p) + \nu_{\text{eff}}\nabla^2\mathbf{u} + \mathbf{F}, \tag{7.2}$$

where ρ is the fluid density, $\mathbf{u}$ and p are the volume-averaged velocity and pressure, respectively, ν_{eff} is the effective viscosity, and ϵ is the porosity. The total body force $\mathbf{F}$ caused by the presence of a porous medium and other external force fields is given by

$$\mathbf{F} = -\frac{\epsilon\nu}{K}\mathbf{u} - \frac{\epsilon c_F}{\sqrt{K}}|\mathbf{u}|\mathbf{u} + \epsilon\mathbf{G}, \tag{7.3}$$

where ν is the shear viscosity of the fluid that is not necessarily the same as ν_{eff}, $\mathbf{G}$ is the body force induced by an external force, c_F is the Forchheimer coefficient that depends on the porous structure, and K is the permeability of the porous media. The first and the second terms on the right hand side of Eq. (7.3) are the linear Darcy and non-linear Forchheimer drags due to the porous medium, respectively. The quadratic nature of the non-linear resistance makes it negligible for low-speed flows, but is more noteworthy in hindering the fluid motion for high-speed flows, i.e., high Reynolds number and high Da number flows.

The GLBM considers Eq. (7.3) as a source term in Eq. (3.20) and also modifies the equilibrium distribution function (Eq. (3.24)) based on the porosity. The detailed formulation can be found in (*Guo and Zhao*, 2002).

7.5 Comparison of a homogenized LBM with the pore-scale LB simulation

Firstly to validate the generalized model for flow over a porous medium, we choose a simple Couette flow. The lower-half of the channel of width H is filled with a porous medium with a porosity of ϵ, the stream-wise and span-wise boundaries are periodic,

and the top wall of the channel is moving with a constant velocity of u_0. Then, the steady state velocity in this channel satisfies

$$\nu_{\text{eff}}\nabla^2\mathbf{u} - \frac{\epsilon\nu}{K}\mathbf{u} - \frac{\epsilon c_F}{\sqrt{K}}|\mathbf{u}|\mathbf{u} + \epsilon\mathbf{G} = 0, \tag{7.4}$$

while the walls of the channel are modeled by a no-slip condition.

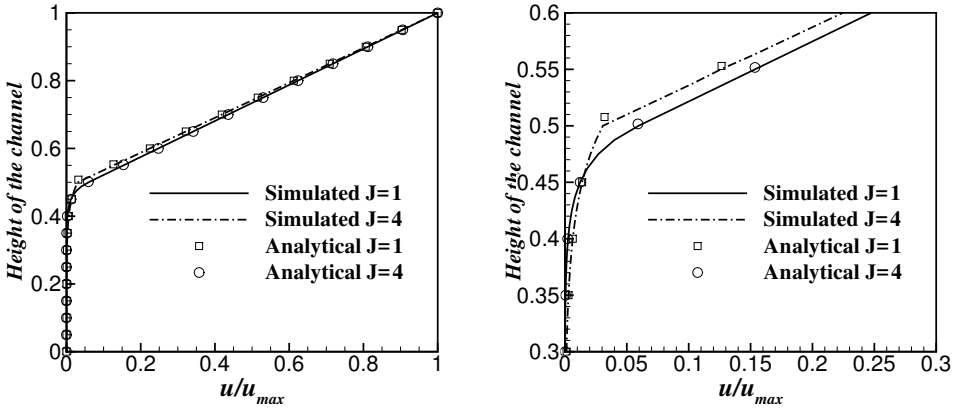

Figure 7.7: Velocity profile of the Couette flow for different viscosity ratios $J = \mu_e/\mu$, in comparison with the approximate analytical solution of Eq. (7.5), a) global system, b) zoom into the region near the interface

Figure 7.7 shows the velocity profile for the Couette flow with different viscosity ratios J ($= \mu_e/\mu$) and compared to a semi-analytical solution for $Re = 0.1$ and $Da = 0.00012$. In the Stokes regime for a low Da number, (*Martys et al.*, 1994) reported that the velocity profile in the free flow is linear and exponentially decaying in the porous region. More precisely the semi-analytic solution can be written as:

$$u_x(y) = \begin{cases} rKa + \epsilon a\,(y - H/2) & H/2 \le y \le H \\ rKae^{r(y-H/2)} & 0 \le y \le H/2 \end{cases} \tag{7.5}$$

where

$$a = \frac{2u_0}{2rK + \epsilon H}, \quad r = \frac{\sqrt{\nu\epsilon}}{\sqrt{\nu_{\text{eff}}k}}, \tag{7.6}$$

and u_0 is the lid's velocity. The simulation result shows excellent agreement with the analytical solution for both viscosity ratios.

Secondly, we apply the generalized model to a problem with no sharp interface and a significant porosity change close to the interface. We use the planar average of the porosity as it is obtained in the DNS, therefore, there is no need to explicitly set the

interface position. Since the flow is within the Stokes regime, the Forchheimer term in Eq. (7.3) is neglected.

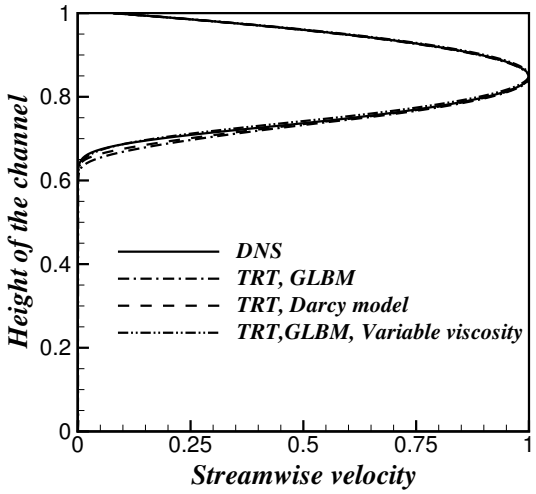

Figure 7.8: A comparison between the planar average of the stream-wise velocity obtained by DNS and the homogenized model, $Re_D \simeq 2$.

Figure 7.8 shows the results of the planar average stream-wise velocity for the DNS solution and the GLBM. Although the porosity, permeability, fluid properties and driving forces are the same, the standard GLBM homogenized model over-predicts the velocity in the transition zone. The dashed line shows the homogenized model that only takes the Darcy force into account. These two mentioned homogenized models use a viscosity in the porous region which is equal to the free flow region. We propose to use the GLBM homogenized model but with a viscosity in the porous region depending on the porosity by $\mu_{\text{eff}} = \mu/\epsilon$. As we can observe in the porous region, the latter model can perfectly predict the DNS result.

7.6 Turbulent Flow over a permeable wall

In this section, we show an illustration of a DNS solution of turbulent flow over permeable bed with semi-realistic porous structure consisting several spherical particles.

To resolve all scales, the porous media part of the domain is refined using three different levels of refinement. Periodic boundary conditions have been used in the stream-wise and span-wise direction while the top boundary is free slip. We apply

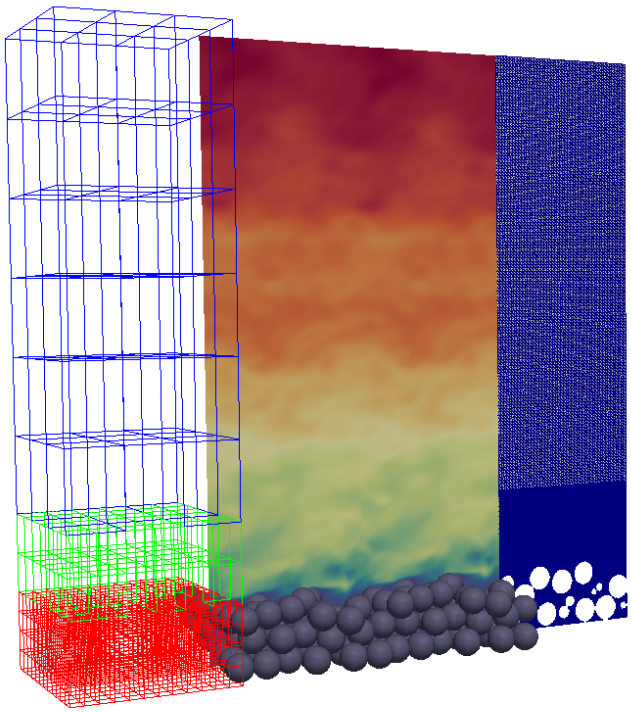

Figure 7.9: Turbulent flow over a permeable bed, left to right, the block structure, velocity contour and the grids, respectively.

the TRT model of collision and the CLI scheme for wall boundary condition. The simulation is executed on the LIMA supercomputer, with 64 nodes and 24 cores on each node. With this configuration it roughly takes 24 hours of computation for the whole simulation for a spatial resolution of 9×10^7 cells. Figure 7.9 shows the contours of the flow velocity of the simulation after 5×10^6 timesteps. The block structure used in WALBERLA is shown on the left hand side of the figure to indicate the static refinement of the meshes. The grids are also displayed on the right hand side of the contour to show the grid resolution. We point out that the results are stored after coarsening the grids throughout the domain by a factor of 8 to keep the size of the resulting outputs reasonable for post-processing and visualization.

7.7 Summary

In this chapter, we presented multi-scale lattice Boltzmann simulation of free flow over porous media. Evaluation of different two domain approaches showed that the interface position affects the entire velocity profile. Although it is not possible to define the best value for the interface position by having only the permeable bed information, by knowing the flow behavior it is possible to find an optimum value for it.

Homogenized LBM simulation with variable viscosity showed promising results in compare to the DNS results. A large-scale simulation of turbulent flow over the permeable bed was illustrated to highlight the ability of the high-performance framework.

The following chapter concludes this thesis with a summary and outlooks will be given for future works.

8 Conclusion

The objective of this work is to demonstrate the ability of the lattice Boltzmann method approach to simulate flow through porous media in different scales. The main focus is on the simulation strategy, accuracy, and stability of the method. Careful evaluation is performed to find the best combinations of the approaches involved in the LBM. Then, the applicability of the method is examined in structured and random packing of particles, as well as free flow over a permeable bed.

This chapter reviews the obtained results and gives an outlook on how this research can be continued.

8.1 Summary

In order to evaluate the LBM, three-dimensional flow through periodic simple sphere packs for two different solid volume fractions and a large range of Reynolds numbers is simulated and analyzed in chapter 4. Two different lattice schemes, namely, the D_3Q_{19} and D_3Q_{27} have been examined. A periodic pressure boundary condition has been adapted to drive the flow. Different collision operators and various types of boundary conditions (see chapter 3) at low and high Reynolds numbers are studied.

The evaluation at low Reynolds numbers shows that the periodic pressure boundary can accurately simulate porous media flows. The convergence study in the Stokes regime is investigated by computing the drag force with various sizes of spheres while the solid volume fraction is fixed. The results show that the simple bounce-back (SBB) boundary scheme converges with first order, the linear interpolation bounce-back (LIBB) converges between first and second-order, the quadratic interpolation bounce-back (QIBB) and the interpolation-extrapolation bounce-back (IEBB) converge with second-order and the multi-reflection method (MR) converges with third-order. The SRT collision operator produces a viscosity-dependent permeability

for all boundary schemes, while the MRT and the TRT models can produce a viscosity independent permeability for the SBB, CLI, and MR boundary conditions. This is explained in Sec. 4.2.

Since the TRT in its optimized version results in a similar run-time to the SRT collision model, and MRT, which is computationally more expensive, does not significantly improve the accuracy, the TRT collision scheme has been used for the simulation of high Re number flows.

Investigating the convergence of various boundary conditions with the TRT collision scheme in inertial flow show that the convergence rate of the MR boundary scheme decreases to second order accuracy while the CLI and SBB maintain the same second-order convergence rate as in the Stokes regime. The degradation in the convergence rate of the MR results from the second-order inheritance of the LBM for the bulk flow in the inertial regime.

Evaluating the boundary schemes in weakly turbulent flow at $Re_p \approx 315$ shows that the CLI converges with lower than second order, while other boundary schemes do not show any clear convergence behavior. The drag coefficient calculated with the SBB boundary condition differs by at most 2% compared to the results calculated with the CLI and MR boundary schemes (see Sec. 4.2).

Based on the result presented in chapter 4, the application of the CLI combined with the TRT can be considered as a good balance between accuracy and efficiency. Comparing the two lattice models with full and reduced stencils in turbulent flow at $Re_p = 2477$, reveals the clear differences in the flow field caused by the lack of isotropy in the reduced scheme. However, porous media properties such as permeability and the drag force show less than 3% difference between these two lattice models. For flow at $Re_p < 100$, the difference is negligible, and that beyond this Reynolds number, the difference increases with increasing Reynolds number.

We also examined the ability of the model and the framework with three large-scale simulations, such as flow through the structured array of spheres, random packing of various particles in the laminar regime, and the flow over a permeable bed.

In chapter 5, flow through the structured array of spheres is simulated to investigate the flow behavior in a wide range of Reynolds numbers. Existing models for the permeability is evaluated and compared to the high-resolution pore-scale simulation results.

Considering the Forchheimer model for high Reynolds number flow, it is shown in Sec. 5.4.1 that the Forchheimer coefficient is strongly dependent on Re number, Our results, however, indicate that constant values can be considered for turbulent regimes of the flow. The results for the permeability in Sec. 5.4.2 show that, contrary to the Barree–Conway model, no plateau area for the permeability can be observed at high Reynolds number. Although the results show that the model can predict the permeability at $Re_p < 1000$, however, the permeability decreases by increasing the Reynolds number which is in line with the theory derived from the Navier-Stokes equation. Also, the results show good agreement with the friction factor models (see Sec. 5.4.3). Various flow regimes can be defined for different Reynolds numbers when the square root of the permeability is considered as the characteristic length scale.

Dense and dilute unstructured packing is also examined in chapter 6. Fully resolved simulation results are provided for packing of spherical, and non-spherical particles and compared to the existing correlations. Effect of porosity, flow rate, and particle shape were presented. A modification for the Carman-Kozney correlation is provided for creeping flow.

The result of the dense sphere packing is compared to the Carman-Kozney correlation, as well as the result of the simple sphere array (see Sec. 6.2). It was shown that the randomness of the pack influences the permeability such that the permeability of the random packing, generally, is lower than the structured packing.

To investigate the particle shape on the permeability, various packing of spherocylinderical particles are examined. The effect of orientation, aspect ratio, and Reynolds number is presented in Sec. 6.3. The results depict that the aspect ratio strongly affects the flow capacity. Additionally, the permeability decreases by increasing the Reynolds number in the same manner for different aspect ratio. Furthermore, an illustration of flow through packed beds containing different particles is presented to show the ability of the method.

As a last large-scale simulation, in chapter 7 we presented three different approaches to simulate the interaction of free flow with porous media flow, namely, direct pore-scale simulations, as well as homogenized single-domain and two-domains approaches. The lattice Boltzmann method is employed both, for obtaining the pore-scale reference solution, and for solving the computationally more appealing homogenized problems.

For the two-domain approaches, four different interface conditions for dealing with the physical transport through a sharp interface have been evaluated. Our evaluation depicts that the two-domain techniques are quite sensitive to the interface position (see Sec. 7.3). To further investigate this effect, we examined two definitions for the interface position, i.e., the exact and the apparent position assumptions. However, as our results indicate, both approaches fall short with respect to accuracy in the vicinity of the interface if the exact interface geometry is unknown. As an alternative approach, we consider a homogenized one-domain model in Sec. 7.4 that is based on the idea of a smooth transition zone between the free flow and porous media models. A simple porosity-dependent re-scaling of the viscosity allows us to accurately reproduce the results obtained by averaging the pore-scale solution. In Sec. 7.6 we also present an illustration of turbulent flow over a permeable wall which is constructed by spherical particles.

8.2 Outlook

In this thesis, we evaluated the LBM for different scenarios, but the physical understanding of the porous media flow are not fully considered. In a future study, more advanced collision models, like cumulant and entropic collision models, could be considered which offer more stability.

We investigated the fluid flow behavior in a simple array of spheres, however, more realistic porous media geometries could be of interest to investigate, while experimental tests are often cumbersome to study the shape effects. Finding good correlations along with the coupling of the pe software framework and the waLBerla gives the possibility to simulate the DEM-CFD in macro-scale.

Additionally, turbulent flow characteristics, energy dissipation, and flow capacity are of importance in the practical applications that can be simulated by proposed strategies in this thesis. Simulation of turbulent flow over the permeable bed with the ability of adaptive refinement is performed by DNS in this work. However, using turbulence models such as large eddy can be utilized to investigate the boundary layer effects and penetration depth into the permeable bed.

In future work, we aim to investigate the combination of homogenized and pore-scale approaches to allow for the treatment of more general situations in a two-scale fashion. Since the discussed lattice Boltzmann schemes are suitable for REV-scale computations and are also highly scalable for pore-scale simulations,

they lend themselves well for leveraging the power of massively parallel computing architectures.

Bibliography

P. M. Adler (1992). *Porous media : geometry and transports*. Butterworth-Heinemann Limited.

B. Alazmi and K. Vafai, *Analysis of fluid flow and heat transfer interfacial conditions between a porous medium and a fluid layer*. *International Journal of Heat and Mass Transfer*, 44 (2001)(9), 1735 – 1749.

K. Allen, T. von Backström, and D. Kröger, *Packed bed pressure drop dependence on particle shape, size distribution, packing arrangement and roughness*. *Powder Technology*, 246 (2013), 590–600.

K. Baber, K. Mosthaf, B. Flemisch, R. Helmig, S. Müthing, and B. Wohlmuth, *Numerical scheme for coupling two-phase compositional porous-media flow and one-phase compositional free flow*. *IMA J. Appl. Math.*, 6 (2012)(77), 887–909.

O. Bagci, N. Dukhan, and M. Özdemir, *Flow regimes in packed beds of spheres from pre-Darcy to turbulent*. *Transport in Porous Media*, 104 (2014)(3), 501–520.

R. Barree and M. Conway (2004). *Beyond beta factors: a complete model for Darcy, Forchheimer and Trans-Forchheimer flow in porous media*. In *SPE Annual Technical Conference and Exhibition held in Houston Texas, September 2004*, pages 1–8. Society of Petroleum Engineers. SPE paper no. 89325.

D. Bartuschat and U. Rüde, *Parallel multiphysics simulations of charged particles in microfluidic flows*. *Journal of Computational Science*, 8 (2015)(0), 1 – 19.

D. E. Beasley and J. A. Clark, *Transient response of a packed bed for thermal energy storage*. *International Journal of Heat and Mass Transfer*, 27 (1984)(9), 1659–1669.

G. S. Beavers and D. D. Joseph, *Boundary conditions at a naturally permeable wall*. *Journal of Fluid Mechanics*, 30 (1967), 197–207.

R. Beetstra, M. van der Hoef, and J. Kuipers, *A lattice-Boltzmann simulation study of the drag coefficient of clusters of spheres*. *Computers and Fluids*, 35 (2006)(8–9), 966 – 970. Proceedings of the First International Conference for Mesoscopic Methods in Engineering and Science.

R. Beetstra, M. A. van der Hoef, and J. A. M. Kuipers, *Drag force of intermediate reynolds number flow past mono- and bidisperse arrays of spheres*. *AIChE Journal*, 53 (2007)(2), 489–501.

O. Behrend, *Solid-fluid boundaries in particle suspension simulations via the lattice Boltzmann method*. *Phys. Rev. E*, 52 (1995), 1164–1175.

R. Benzi, S. Succi, and M. Vergassola, *The lattice Boltzmann equation: theory and applications*. *Physics Reports*, 222 (1992)(3), 145–197.

J. Bernsdorf, G. Brenner, and F. Durst, *Numerical analysis of the pressure drop in porous media flow with lattice Boltzmann (BGK) automata*. *Computer Physics Communications*, 129 (2000)(1–3), 247 – 255.

P. L. Bhatnagar, E. P. Gross, and M. Krook, *A model for collision processes in gases. i. small amplitude processes in charged and neutral one-component systems*. *Phys. Rev.*, 94 (1954), 511–525.

S. Bogner, S. Mohanty, and U. Rüde, *Drag correlation for dilute and moderately dense fluid-particle systems using the lattice Boltzmann method*. *International Journal of Multiphase Flow*, 68 (2015)(0), 71 – 79.

G. Bokkers, M. van Sint Annaland, and J. Kuipers, *Mixing and segregation in a bidisperse gas–solid fluidised bed: a numerical and experimental study*. *Powder Technology*, 140 (2004)(3), 176–186.

A. M. Bouwman, J. C. Bosma, P. Vonk, J. A. Wesselingh, and H. W. Frijlink, *Which shape factor(s) best describe granules?* *Powder Technology*, 146 (2004)(1-2), 66–72.

M. Bouzidi, D. d'Humières, P. Lallemand, and L.-S. Luo, *Lattice Boltzmann equation on a two-dimensional rectangular grid*. *Journal of Computational Physics*, 172 (2001a)(2), 704 – 717.

M. Bouzidi, M. Firdaouss, and P. Lallemand, *Momentum transfer of a Boltzmann-lattice fluid with boundaries*. *Physics of Fluids (1994-present)*, 13 (2001b)(11), 3452–3459.

J. M. Buick and C. A. Greated, *Gravity in a lattice Boltzmann model. Phys. Rev. E*, 61 (2000), 5307–5320.

P. C. Carman, *Fluid flow through granular beds. Transactions of the Institution of Chemical Engineers*, 15 (1937), 150–166.

M. Chandesris and D. Jamet, *Jump conditions and surface-excess quantities at a fluid/porous interface: A multi-scale approach. Transport in Porous Media*, 78 (2009)(3), 419–438.

S. Chapman and T. G. Cowling (1991). *The Mathematical Theory of Non-uniform Gases: An Account of the Kinetic Theory of Viscosity, Thermal Conduction and Diffusion in Gases (Cambridge Mathematical Library)*. Cambridge University Press, 3 edition.

H. Chen, *Volumetric formulation of the lattice Boltzmann method for fluid dynamics: Basic concept. Physical Review E*, 58 (1998)(3), 3955.

H. Chen, O. Filippova, J. Hoch, K. Molvig, R. Shock, C. Teixeira, and R. Zhang, *Grid refinement in lattice Boltzmann methods based on volumetric formulation. Physica A: Statistical Mechanics and its Applications*, 362 (2006)(1), 158–167.

S. Chen and G. D. Doolen, *Lattice Boltzmann method for fluid flows. Annual Review of Fluid Mechanics*, 30 (1998)(1), 329–364.

Y. Chen, J. Third, and C. Müller, *A drag force correlation for approximately cubic particles constructed from identical spheres. Chemical Engineering Science*, 123 (2015), 146–154.

N.-S. Cheng, *Wall effect on pressure drop in packed beds. Powder Technology*, 210 (2011)(3), 261 – 266.

R. P. Chhabra, L. Agarwal, and N. K. Sinha, *Drag on non-spherical particles: an evaluation of available methods. Powder Technology*, 101 (1999)(3), 288–295.

B. Chun and A. J. C. Ladd, *Interpolated boundary condition for lattice Boltzmann simulations of flows in narrow gaps. Phys. Rev. E*, 75 (2007), 066705.

H. Darcy, *Recherches expérimentales relatives au mouvement de l'eau dans les tuyaux. Mallet-Bachelier, Paris*, (1857).

D. d'Humières, *Generalized lattice Boltzmann equations. Progress in Aeronautics and Astronautics*, 159 (1992), 450+.

D. d'Humières, I. Ginzburg, M. Krafczyk, P. Lallemand, and L. Luo, *Multiple–relaxation–time lattice Boltzmann models in three dimensions*. *Philosophical Transactions of the Royal Society of London. Series A: Mathematical, Physical and Engineering Sciences*, 360 (2002)(1792), 437–451.

N. Dukhan and K. Patel, *Effect of sample's length on flow properties of open-cell metal foam and pressure-drop correlations*. *Journal of Porous Materials*, 18 (2011)(6), 655–665.

T. Duman and U. Shavit, *An apparent interface location as a tool to solve the porous interface flow problem*. *Transport in Porous Media*, 78 (2009)(3), 509–524.

A. Dupuis (2002). *From a Lattice Boltzmann model to a parallel and reusable implementation of a virtual river*. Ph.D. thesis, University of Geneva.

A. Dupuis and B. Chopard, *Theory and applications of an alternative lattice Boltzmann grid refinement algorithm*. *Physical Review E*, 67 (2003)(6).

G. Eitel-Amor, M. Meinke, and W. Schröder, *A lattice-Boltzmann method with hierarchically refined meshes*. *Computers & Fluids*, 75 (2013), 127 – 139.

S. Ergun, *Fluid flow through packed columns*. *Chemical Engineering Progress*, 48 (1952)(2), 89–94.

A. Fakhari and T. Lee, *Numerics of the lattice Boltzmann method on nonuniform grids: Standard LBM and finite-difference LBM*. *Computers & Fluids*, 107 (2015), 205 – 213.

R. Fand, B. Kim, A. Lam, and R. Phan, *Resistance to the flow of fluids through simple and complex porous media whose matrices are composed of randomly packed spheres*. *Journal of fluids engineering*, 109 (1987)(3), 268–273.

E. Fattahi, C. Waluga, B. Wohlmuth, and U. Rüde (2016a). *Large scale lattice Boltzmann simulation for the coupling of free and porous media flow*. In *High Performance Computing in Science and Engineering: Second International Conference, HPCSE 2015, Soláň, Czech Republic, May 25-28, 2015, Revised Selected Papers*, pages 1–18. Springer International Publishing, Cham.

E. Fattahi, C. Waluga, B. Wohlmuth, U. Rüde, M. Manhart, and R. Helmig, *Lattice Boltzmann methods in porous media simulations: From laminar to turbulent flow*. *Computers & Fluids*, 140 (2016b), 247 – 259.

C. Feichtinger, S. Donath, H. Köstler, J. Götz, and U. Rüde, *WaLBerla: HPC software design for computational engineering simulations. Journal of Computational Science*, 2 (2011)(2), 105 – 112. Simulation Software for Supercomputers.

Z.-G. Feng and E. E. Michaelides, *The immersed boundary-lattice Boltzmann method for solving fluid–particles interaction problems. Journal of Computational Physics*, 195 (2004)(2), 602 – 628.

O. Filippova and D. Hänel, *Grid refinement for lattice-BGK models. J. Comput. Phys.*, 147 (1998)(1), 219–228.

P. Forchheimer, *Wasserbewegung durch Boden. Z. Ver. Deutsch. Ing*, 45 (1901), 1782–1788.

D. M. Freed, *Lattice-Boltzmann method for macroscopic porous media modeling. International Journal of Modern Physics C*, 09 (1998)(08), 1491–1503.

S. Freudiger, J. Hegewald, and M. Krafczyk, *A parallelisation concept for a multi-physics lattice Boltzmann prototype based on hierarchical grids. Progress in Computational Fluid Dynamics*, 8 (2008)(1-4), 168–178.

H. Freund, T. Zeiser, F. Huber, E. Klemm, G. Brenner, F. Durst, and G. Emig, *Numerical simulations of single phase reacting flows in randomly packed fixed-bed reactors and experimental validation. Chemical Engineering Science*, 58 (2003)(3-6), 903–910.

U. Frisch, B. Hasslacher, and Y. Pomeau, *Lattice-gas automata for the navier-stokes equation. Phys. Rev. Lett.*, 56 (1986), 1505–1508.

M. Geier, M. Schönherr, A. Pasquali, and M. Krafczyk, *The cumulant lattice Boltzmann equation in three dimensions: Theory and validation. Computers & Mathematics with Applications*, 70 (2015)(4), 507 – 547.

S. Geller, S. Uphoff, and M. Krafczyk, *Turbulent jet computations based on {MRT} and cascaded lattice Boltzmann models. Computers and Mathematics with Applications*, 65 (2013)(12), 1956 – 1966.

M. Ghisalberti, *The three-dimensionality of obstructed shear flows. Environmental Fluid Mechanics*, 10 (2010)(3), 329–343.

I. Ginzbourg and D. d'Humières, *Local second-order boundary methods for lattice Boltzmann models. Journal of Statistical Physics*, 84 (1996)(5), 927–971.

I. Ginzburg, *Lattice Boltzmann modeling with discontinuous collision components: Hydrodynamic and advection-diffusion equations*. *Journal of Statistical Physics*, 126 (2007)(1), 157–206.

I. Ginzburg, *Consistent lattice Boltzmann schemes for the Brinkman model of porous flow and infinite Chapman-Enskog expansion*. *Phys. Rev. E*, 77 (2008), 066704.

I. Ginzburg and D. d'Humières, *Multireflection boundary conditions for lattice Boltzmann models*. *Physical Review E*, 12 (2003)(68), 666–614.

I. Ginzburg, F. Verhaeghe, and D. d'Humières, *Study of simple hydrodynamic solutions with the two-relaxation-times lattice-Boltzmann scheme*. *Communications in Computational Physics*, 3 (2008a), 519+.

I. Ginzburg, F. Verhaeghe, and D. d'Humières, *Two-Relaxation-Time lattice Boltzmann Scheme: About Parametrization, Velocity, Pressure and Mixed Boundary Conditions*. *Commun. Comput. Phys.*, 3 (2008b)(2), 427+.

C. Godenschwager, F. Schornbaum, M. Bauer, H. Köstler, and U. Rüde (2013). *A framework for hybrid parallel flow simulations with a trillion cells in complex geometries*. In *Proceedings of SC13: International Conference for High Performance Computing, Networking, Storage and Analysis*, SC '13, pages 35:1–35:12. ACM, New York, NY, USA.

A. Goharzadeh, A. Khalili, and B. B. JÃc rgensen, *Transition layer thickness at a fluid-porous interface*. *Physics of Fluids*, 17 (2005)(5), 057102.

T. I. Gombosi (1994). *Gaskinetic theory*. Cambridge atmospheric and space science series. Cambridge University Press, Cambridge [England] ; New York.

J. Götz, K. Iglberger, M. Stürmer, and U. Rüde (2010). *Direct numerical simulation of particulate flows on 294912 processor cores*. In *Proceedings of the 2010 ACM/IEEE International Conference for High Performance Computing, Networking, Storage and Analysis*, SC '10, pages 1–11. IEEE Computer Society, Washington, DC, USA.

B. Goyeau, D. Lhuillier, D. Gobin, and et al., *Momentum transport at a fluid-porous interface*. *International Journal Of Heat And Mass Transfer*, 46 (2003), 4071–4081.

O. Gräser and A. Grimm, *Adaptive generalized periodic boundary conditions for lattice Boltzmann simulations of pressure-driven flows through confined repetitive geometries*. *Phys. Rev. E*, 82 (2010), 016702.

A. Guardo, M. Coussirat, F. Recasens, M. Larrayoz, and X. Escaler, *CFD study on particle-to-fluid heat transfer in fixed bed reactors: Convective heat transfer at low and high pressure*. *Chemical Engineering Science*, 61 (2006)(13), 4341–4353.

X. Guo, J. Lin, and D. Nie, *New formula for drag coefficient of cylindrical particles*. *Particuology*, 9 (2011)(2), 114 – 120.

Z. Guo and T. Zhao, *Lattice Boltzmann model for incompressible flows through porous media*. *Physical Review E*, 66 (2002)(3), 036304.

Z. Guo, C. Zheng, and B. Shi, *Discrete lattice effects on the forcing term in the lattice Boltzmann method*. *Phys. Rev. E*, 65 (2002), 046308.

J. Hardy, O. De Pazzis, and Y. Pomeau, *Molecular dynamics of a classical lattice gas: Transport properties and time correlation functions*. *Physical review A*, 13 (1976)(5), 1949.

X. He and L.-S. Luo, *Lattice Boltzmann model for the incompressible Navier–Stokes equation*. *Journal of Statistical Physics*, 88 (1997)(3-4), 927–944.

R. Helmig, *Multiphase flow and transport processes in the subsurface: A contribution to the modeling of hydrosystems*. *Springer*, (2011).

R. J. Hill and D. L. Koch, *The transition from steady to weakly turbulent flow in a close-packed ordered array of spheres*. *Journal of Fluid Mechanics*, 465 (2002), 59–97.

R. J. Hill, D. L. Koch, and A. J. C. Ladd, *The first effects of fluid inertia on flows in ordered and random arrays of spheres*. *Journal of Fluid Mechanics*, 448 (2001), 213–241.

E. J. Hinch, *An averaged-equation approach to particle interactions in a fluid suspension*. *Journal of Fluid Mechanics*, 83 (1977)(04), 695.

M. A. V. D. Hoef, R. Beetstra, and J. A. M. Kuipers, *Lattice-Boltzmann simulations of low-Reynolds-number flow past mono- and bidisperse arrays of spheres: results for the permeability and drag force*. *Journal of Fluid Mechanics*, 528 (2005), 233–254.

D. J. Holdych, D. R. Noble, J. G. Georgiadis, and R. O. Buckius, *Truncation error analysis of lattice Boltzmann methods*. *Journal of Computational Physics*, 193 (2004)(2), 595 – 619.

L. Hua, H. Zhao, J. Li, J. Wang, and Q. Zhu, *Eulerian–Eulerian simulation of irregular particles in dense gas–solid fluidized beds*. *Powder Technology*, 284 (2015), 299–311.

H. Huang, M. Krafczyk, and X. Lu, *Forcing term in single-phase and shan-chen-type multiphase lattice Boltzmann models*. *Phys. Rev. E*, 84 (2011), 046710.

K. Huang, J. Wan, C. Chen, L. He, W. Mei, and M. Zhang, *Experimental investigation on water flow in cubic arrays of spheres*. *Journal of Hydrology*, 492 (2013), 61 – 68.

J.-J. Hwang, G.-J. Hwang, R.-H. Yeh, and C.-H. Chao, *Measurement of interstitial convective heat transfer and frictional drag for flow across metal foams*. *Journal of Heat Transfer*, 124 (2002)(1), 120–129.

A. Hölzer and M. Sommerfeld, *New simple correlation formula for the drag coefficient of non-spherical particles*. *Powder Technology*, 184 (2008)(3), 361–365.

S. K. Kang and Y. A. Hassan, *The effect of lattice models within the lattice Boltzmann method in the simulation of wall-bounded turbulent flows*. *Journal of Computational Physics*, 232 (2013)(1), 100 – 117.

S. Khirevich, I. Ginzburg, and U. Tallarek, *Coarse-and fine-grid numerical behavior of MRT/TRT lattice Boltzmann schemes in regular and random sphere packings*. *Journal of Computational Physics*, 281 (2015), 708–742.

J. Kim, J. Lee, and K.-C. Lee, *Nonlinear correction to Darcy's law for a flow through periodic arrays of elliptic cylinders*. *Physica A: Statistical Mechanics and its Applications*, 293 (2001)(1–2), 13 – 20.

S. Kim and W. B. Russel, *Modelling of porous media by renormalization of the Stokes equations*. *Journal of Fluid Mechanics*, 154 (1985)(-1), 269.

S. H. Kim and H. Pitsch, *A generalized periodic boundary condition for lattice Boltzmann method simulation of a pressure driven flow in a periodic geometry*. *Physics of Fluids*, 19 (2007)(10), 108101.

D. L. Koch and A. S. Sangani, *Particle pressure and marginal stability limits for a homogeneous monodisperse gas-fluidized bed: kinetic theory and numerical simulations*. *Journal of Fluid Mechanics*, 400 (1999), 229–263.

P. K. Kundu, I. M. Cohen, and D. R. Dowling (2012). *Fluid mechanics*. Academic Press, Waltham, MA, 5th ed edition. OCLC: ocn713567396.

D. Kunii and O. Levenspiel (1991). *Fluidization Engineering, 2nd Edition*. Butterworth-Heinemann.

A. J. Ladd, *Numerical simulations of particulate suspensions via a discretized Boltzmann equation part ii. numerical results. arXiv preprint comp-gas/9306005*, (1993).

A. J. C. Ladd, *Numerical simulations of particulate suspensions via a discretized Boltzmann equation. part 2. numerical results. Journal of Fluid Mechanics*, 271 (1994), 311–339.

J. Lage, *The fundamental theory of flow through permeable niedia from Darcy to turbulence. Transport phenomena in porous media*, (1998), 1.

B. Lai, J. L. Miskimins, and Y.-S. Wu (2012). *Non-Darcy porous-media flow according to the Barree and Conway model: Laboratory and numerical-modeling studies*. In *Society of Petroleum Engineers*, pages 70 –79.

P. Lallemand and L.-S. Luo, *Theory of the lattice Boltzmann method: Dispersion, dissipation, isotropy, galilean invariance, and stability. Phys. Rev. E*, 61 (2000), 6546–6562.

P. Lallemand and L.-S. Luo, *Lattice Boltzmann method for moving boundaries. Journal of Computational Physics*, 184 (2003)(2), 406 – 421.

M. Le Bars and M. G. Worster, *Interfacial conditions between a pure fluid and a porous medium: implications for binary alloy solidification. Journal of Fluid Mechanics*, 550 (2006), 149–173.

T. Lee and C.-L. Lin, *An eulerian description of the streaming process in the lattice Boltzmann equation. Journal of Computational Physics*, 185 (2003)(2), 445 – 471.

L. Liu, Z. Zhang, and A. Yu, *Dynamic simulation of the centripetal packing of mono-sized spheres. Physica A: Statistical Mechanics and its Applications*, 268 (1999)(3–4), 433 – 453.

Q. Liu and A. Prospretti, *Pressure-driven flow in a channel with porous walls. Journal of Fluid Mechanics*, 679 (2011), 77–100.

H. Lopez-Hernandez (2007). *Experimental Analysis and Macroscopic and Pore-level Flow Simulations to Compare Non-Darcy Flow Models in Porous Media*. Ph.D. thesis, Colorado School of Mines. Department of Petroleum Engineering.

T. S. Lundgren, *Slow flow through stationary random beds and suspensions of spheres*. *Journal of Fluid Mechanics*, 51 (1972), 273–299.

L.-S. Luo, *Analytic solutions of linearized lattice Boltzmann equation for simple flows*. *Journal of Statistical Physics*, 88 (1997)(3), 913–926.

N. Martys, D. P. Bentz, and E. J. Garboczi, *Computer simulation study of the effective viscosity in Brinkman's equation*. *Physics of Fluids*, 6 (1994)(4), 1434–1439.

N. Martys, X. Shan, and H. Chen, *Evaluation of the external force term in the discrete Boltzmann equation*. *Phys. Rev. E*, 58 (1998)(5), 6855–6857.

N. S. Martys, *Improved approximation of the Brinkman equation using a lattice Boltzmann method*. *Physics of Fluids*, 13 (2001)(6), 1807–1810.

G. Mayer and G. Házi, *Direct numerical and large eddy simulation of longitudinal flow along triangular array of rods using the lattice Boltzmann method*. *Mathematics and Computers in Simulation (MATCOM)*, 72 (2006)(2), 173–178.

G. R. McNamara and G. Zanetti, *Use of the Boltzmann equation to simulate lattice-gas automata*. *Phys. Rev. Lett.*, 61 (1988), 2332–2335.

R. Mei, W. Shyy, D. Yu, and L.-S. Luo, *Lattice Boltzmann method for 3-D flows with curved boundary*. *Journal of Computational Physics*, 161 (2000)(2), 680 – 699.

A. Mohamad and A. Kuzmin, *A critical evaluation of force term in lattice Boltzmann method, natural convection problem*. *International Journal of Heat and Mass Transfer*, 53 (2010)(5–6), 990 – 996.

M. Morad and A. Khalili, *Transition layer thickness in a fluid-porous medium of multi-sized spherical beads*. *Experiments in Fluids*, 46 (2009)(2), 323–330.

K. Mosthaf, K. Baber, B. Flemisch, R. Helmig, A. Leijnse, I. Rybak, and B. Wohlmuth, *A new coupling concept for two-phase compositional porous media and single-phase compositional free flow*. *Water Resour. Res.*, 47 (2011), 1–19.

K. N. Moutsopoulos, *One-dimensional unsteady inertial flow in phreatic aquifers induced by a sudden change of the boundary head*. *Transport in Porous Media*, 70 (2007)(1), 97–125.

K. N. Moutsopoulos, I. N. Papaspyros, and V. A. Tsihrintzis, *Experimental investigation of inertial flow processes in porous media*. *Journal of hydrology*, 374 (2009)(3), 242–254.

A. Nabovati, E. W. Llewellin, and A. C. Sousa, *A general model for the permeability of fibrous porous media based on fluid flow simulations using the lattice Boltzmann method. Composites Part A: Applied Science and Manufacturing*, 40 (2009)(6–7), 860 – 869.

R. W. Nash, H. B. Carver, M. O. Bernabeu, J. Hetherington, D. Groen, T. Krüger, and P. V. Coveney, *Choice of boundary condition for lattice-Boltzmann simulation of moderate-reynolds-number flow in complex domains. Physical Review E*, 89 (2014), 023303.

D. Nemec and J. Levec, *Flow through packed bed reactors: 1. single-phase flow. Chemical Engineering Science*, 60 (2005)(24), 6947 – 6957.

D. Nield and A. Bejan, *Convection in porous media. Springer*, (2006).

D. Nield and A. Kuznetsov, *The effect of a transition layer between a fluid and a porous medium: shear flow in a channel. Transport in Porous Media*, 78 (2009)(3), 477–487.

M. Nikku, P. Jalali, J. Ritvanen, and T. Hyppänen, *Characterization method of average gas–solid drag for regular and irregular particle groups. Powder Technology*, 253 (2014), 284 – 294.

P. Nithiarasu, K. Seetharamu, and T. Sundararajan, *Natural convective heat transfer in a fluid saturated variable porosity medium. International Journal of Heat and Mass Transfer*, 40 (1997)(16), 3955 – 3967.

J. Ochoa-Tapia and S. Whitaker, *Momentum transfer at the boundary between a porous medium and a homogeneous fluid–ii. comparison with experiment. International Journal of Heat and Mass Transfer*, 38 (1995)(14), 2647 – 2655.

C. Pan, L.-S. Luo, and C. T. Miller, *An evaluation of lattice Boltzmann schemes for porous medium flow simulation. Computers and Fluids*, 35 (2006)(8–9), 898 – 909.

R. H. Perry and D. W. Green, editors (1984). *Perry's Chemical Engineering Handbook*. McGraw-Hill, 6th edition.

C. S. Peskin, *Numerical analysis of blood flow in the heart. Journal of Computational Physics*, 25 (1977)(3), 220 – 252.

A. Peters, S. Melchionna, E. Kaxiras, J. Lätt, J. Sircar, M. Bernaschi, M. Bison, and S. Succi (2010). *Multiscale simulation of cardiovascular flows on the IBM Bluegene/P: Full heart-circulation system at red-blood cell resolution*. In *Proceedings*

of the 2010 ACM/IEEE International Conference for High Performance Computing, Networking, Storage and Analysis, pages 1–10. IEEE Computer Society, Washington DC, USA.

A. Pinelli, I. Naqavi, U. Piomelli, and J. Favier, *Immersed-boundary methods for general finite-difference and finite-volume navier–stokes solvers*. *Journal of Computational Physics*, 229 (2010)(24), 9073 – 9091.

D. Pokrajac and C. Manes, *Velocity measurements of a free-surface turbulent flow penetrating a porous medium composed of uniform-size spheres*. *Transport in Porous Media*, 78 (2009)(3), 367–383.

T. Preclik and U. Ruede, *Ultrascale simulations of non-smooth granular dynamics*. *Computational Particle Mechanics*, (2015), 1–24.

J. Prieur Du Plessis, *Analytical quantification of coefficients in the ergun equation for fluid friction in a packed bed*. *Transport in Porous Media*, 16 (1994)(2), 189–207.

M. B. Reider and J. D. Sterling, *Accuracy of discrete-velocity bgk models for the simulation of the incompressible navier-stokes equations*. *Computers & Fluids*, 24 (1995)(4), 459 – 467.

F. Robertsen, J. Westerholm, and K. Mattila (2015). *Lattice Boltzmann simulations at petascale on multi-GPU systems with asynchronous data transfer and strictly enforced memory read alignment*. In *Parallel, Distributed and Network-Based Processing (PDP), 2015 23rd Euromicro International Conference on*, pages 604–609.

M. Rohde, D. Kandhai, J. J. Derksen, and H. E. A. van den Akker, *A generic, mass conservative local grid refinement technique for lattice-Boltzmann schemes*. *International Journal for Numerical Methods in Fluids*, 51 (2006)(4), 439–468.

F. Rohm (2016). *A cumulant-based collision for Lattice Boltzmann methods in two dimensions* . Master's thesis, Technische Universitaet Muenchen, Department of Mathematics, Munich, Germany.

P. Saffman, *On the boundary condition at the surface of a porous medium*. *Studies in Applied Mathematics*, 50 (1971)(2).

A. Sangani and A. Acrivos, *Slow flow through a periodic array of spheres*. *International Journal of Multiphase Flow*, 8 (1982)(4), 343 – 360.

M. Schönherr, K. Kucher, M. Geier, M. Stiebler, S. Freudiger, and M. Krafczyk, *Multi-thread implementations of the lattice Boltzmann method on non-uniform grids for CPUs and GPUs. Computers and Mathematics with Applications*, 61 (2011), 3730–3743.

F. Schornbaum and U. Rüde, *Massively Parallel Algorithms for the Lattice Boltzmann Method on NonUniform Grids. SIAM Journal on Scientific Computing*, 38 (2016)(2), C96–C126.

M. Sedghi-Asl and H. Rahimi, *Adoption of manning's equation to 1d non-Darcy flow problems. Journal of Hydraulic Research*, 49 (2011)(6), 814–817.

D. Seguin, A. Montillet, and J. Comiti, *Experimental characterisation of flow regimes in various porous media—i: Limit of laminar flow regime. Chemical Engineering Science*, 53 (1998a)(21), 3751–3761.

D. Seguin, A. Montillet, J. Comiti, and F. Huet, *Experimental characterization of flow regimes in various porous media—ii: Transition to turbulent regime. Chemical engineering science*, 53 (1998b)(22), 3897–3909.

G. Silva and V. Semiao, *Truncation errors and the rotational invariance of three-dimensional lattice models in the lattice Boltzmann method. Journal of Computational Physics*, 269 (2014), 259 – 279.

M. Singh and K. Mohanty, *Permeability of spatially correlated porous media. Chemical Engineering Science*, 55 (2000)(22), 5393 – 5403.

P. A. Skordos, *Initial and boundary conditions for the lattice Boltzmann method. Phys. Rev. E*, 48 (1993), 4823–4842.

M. A. A. Spaid and F. R. Phelan, *Lattice Boltzmann methods for modeling microscale flow in fibrous porous media. Physics of Fluids*, 9 (1997)(9), 2468–2474.

D. Staubach (2013). *Static Block-Structured Grid Refinement for Parallel Lattice Boltzmann Simulations*. Master's thesis, FRIEDRICH-ALEXANDER-UNIVERSITÄTERLANGEN-NÜRNBERG, TECHNISCHE FAKULTÄT, DEPARTMENT INFORMATIK, Erlangen, Germany.

J. D. Sterling and S. Chen, *Stability analysis of lattice Boltzmann methods. J. Comput. Phys.*, 123 (1996)(1), 196–206.

S. Succi (2001). *The Lattice-Boltzmann Equation*. Oxford university press, Oxford.

S. Tenneti, R. Garg, and S. Subramaniam, *Drag law for monodisperse gas–solid systems using particle-resolved direct numerical simulation of flow past fixed assemblies of spheres*. *International Journal of Multiphase Flow*, 37 (2011)(9), 1072 – 1092.

J. Tobiś, *Influence of bed geometry on its frictional resistance under turbulent flow conditions*. *Chemical Engineering Science*, 55 (2000)(22), 5359 – 5366.

S. Tran-Cong, M. Gay, and E. E. Michaelides, *Drag coefficients of irregularly shaped particles*. *Powder Technology*, 139 (2004)(1), 21–32.

C. Wen and Y. Yu, *A generalized method for predicting the minimum fluidization velocity*. *AIChE Journal*, 12 (1966)(3), 610–612.

S. Whitaker, *Flow in porous media I: A theoretical derivation of Darcy's law*. *Transport in porous media*, 1 (1986)(1), 3–25.

S. Whitaker, *The Forchheimer equation: a theoretical development*. *Transport in Porous media*, 25 (1996)(1), 27–61.

A. T. White and C. K. Chong, *Rotational invariance in the three-dimensional lattice Boltzmann method is dependent on the choice of lattice*. *J. Comput. Phys.*, 230 (2011)(16), 6367–6378.

D. Yu, R. Mei, L.-S. Luo, and W. Shyy, *Viscous flow computations with the method of lattice Boltzmann equation*. *Progress in Aerospace Sciences*, 39 (2003)(5), 329 – 367.

Z. Yu and L.-S. Fan, *An interaction potential based lattice Boltzmann method with adaptive mesh refinement (AMR) for two-phase flow simulation*. *Journal of Computational Physics*, 228 (2009)(17), 6456–6478.

M. Zastawny, G. Mallouppas, F. Zhao, and B. van Wachem, *Derivation of drag and lift force and torque coefficients for non-spherical particles in flows*. *International Journal of Multiphase Flow*, 39 (2012), 227 – 239.

Z. Zeng and R. Grigg, *A criterion for non-Darcy flow in porous media*. *Transport in porous media*, 63 (2006)(1), 57–69.

J. Zhang and D. Y. Kwok, *Pressure boundary condition of the lattice Boltzmann method for fully developed periodic flows*. *Phys. Rev. E*, 73 (2006), 047702.

Q. Zhang and A. Prospretti, *Pressure-driven flow in a two-dimensional channel with porous walls*. *Journal of Fluid Mechanics*, 631 (2009), 1–21.

H. Zhu, Z. Zhou, R. Yang, and A. Yu, *Discrete particle simulation of particulate systems: A review of major applications and findings*. *Chemical Engineering Science*, 63 (2008)(23), 5728–5770.